REPORT DOCUMENTATION PAGE

Form Approved OMB NO. 0704-0188

1. REPORT DATE (DD-MM-YYYY)	2. REPORT TYPE	3. DATES COVERED (From - To)
20-10-2014	Final Report	1-Jun-2008 - 31-May-2014

4. TITLE AND SUBTITLE	5a. CONTRACT NUMBER
Final Report: Spray and Combustion of Gelled Hypergolic Propellants	W911NF-08-1-0171
	5b. GRANT NUMBER
	5c. PROGRAM ELEMENT NUMBER
	611103

6. AUTHORS	5d. PROJECT NUMBER
Steve Heister, William Anderson, Carlos Corvalan, Osvaldo Campanella, Robert Lucht, Timothee Pourpoint, Paul Sojka, Steven Son, Terrence Meyer, David Schmidt, Phillip Westmoreland	
	5e. TASK NUMBER
	5f. WORK UNIT NUMBER

7. PERFORMING ORGANIZATION NAMES AND ADDRESSES	8. PERFORMING ORGANIZATION REPORT NUMBER
Purdue University 155 South Grant Street West Lafayette, IN 47907 -2114	

9. SPONSORING/MONITORING AGENCY NAME(S) AND ADDRESS (ES)	10. SPONSOR/MONITOR'S ACRONYM(S) ARO
U.S. Army Research Office P.O. Box 12211 Research Triangle Park, NC 27709-2211	11. SPONSOR/MONITOR'S REPORT NUMBER(S) 54215-EG-MUR.28

12. DISTRIBUTION AVAILIBILITY STATEMENT

Approved for Public Release; Distribution Unlimited

13. SUPPLEMENTARY NOTES

The views, opinions and/or findings contained in this report are those of the author(s) and should not contrued as an official Department of the Army position, policy or decision, unless so designated by other documentation.

14. ABSTRACT

This document provides an executive summary of work performed by a Purdue-led team on DoD MURI Project W911NF-08-1-0171 entitled: Spray and Combustion of Gelled Hypergolic Propellants for Future Rocket and Missile Engines. The team was formed in 2008 for the response to MURI RFP and includes participants from Purdue, University of Massachusetts, NC State University, and Iowa State University. The overall organization of the research tasks performed by this group is highlighted in Fig. 1-1. Tasks 1.1 and 1.2 (highlighted in green in Fig. 1.1) were structured to address Rheological Task Characterization of Gelled Propellants while Tasks 2.1-2.5 were

15. SUBJECT TERMS

16. SECURITY CLASSIFICATION OF:			17. LIMITATION OF ABSTRACT	15. NUMBER OF PAGES	19a. NAME OF RESPONSIBLE PERSON
a. REPORT	b. ABSTRACT	c. THIS PAGE	UU		Stephen Heister
UU	UU	UU			19b. TELEPHONE NUMBER
					765-494-5126

Standard Form 298 (Rev 8/98)
Prescribed by ANSI Std. Z39.18

Report Title

Final Report: Spray and Combustion of Gelled Hypergolic Propellants

ABSTRACT

This document provides an executive summary of work performed by a Purdue-led team on DoD MURI Project W911NF-08-1-0171 entitled: Spray and Combustion of Gelled Hypergolic Propellants for Future Rocket and Missile Engines. The team was formed in 2008 for the response to MURI RFP and includes participants from Purdue, University of Massachusetts, NC State University, and Iowa State University. The overall organization of the research tasks performed by this group is highlighted in Fig. 1-1. Tasks 1.1 and 1.2 (highlighted in green in Fig. 1-1) were structured to address Rheological Task Characterization of Gelled Propellants while Tasks 2.1-2.5 were developed to assess Non-
Newtonian Flow Physics of Gelled Propellants. Finally, Tasks 3.1-3.4 addressed the Combustion Physics of Gelled Propellants. Numerous team members contributed to the various tasks over the 5-year effort.

Enter List of papers submitted or published that acknowledge ARO support from the start of the project to the date of this printing. List the papers, including journal references, in the following categories:

(a) Papers published in peer-reviewed journals (N/A for none)

Received   Paper

05/27/2014 27.00 Jennifer Mallory, Paul E. Sojka. ON THE PRIMARY ATOMIZATION OF NON-NEWTONIAN IMPINGING
                  JETS: VOLUME I EXPERIMENTAL INVESTIGATION,
                  Atomization and Sprays, (10 2014): 0. doi: 10.1615/AtomizSpr.2014008676

08/03/2011 9.00 S. Menon, D. Schmidt. Conservative interpolation on unstructured polyhedral meshes: An extension of the
                  supermesh approach to cell-centered finite-volume variables,
                  Computer Methods in Applied Mechanics and Engineering, (05 2011): . doi:

   TOTAL: **2**

Number of Papers published in peer-reviewed journals:

(b) Papers published in non-peer-reviewed journals (N/A for none)

Received	Paper
03/16/2012 24.00	R. Muddu, J. Lu, P. Sojka, C. Corvalan. Threshold wavelength on filaments of complex fluids, Chemical Engineering Science, ( ): . doi:
08/08/2012 25.00	J. Ku, C. M. Corvalan. Coalescence of viscous drops with surfactants, Chemical Engineering Science, ( ): . doi:
09/28/2011 19.00	C. Yoon, S. Heister, G. Xia, C. Merkle. Numerical Modeling of Injection of Shear-Thinning Gel Propellants Through Plain-Orifice Atomizer, Journal of Propulsion and Power, (09 2011): . doi:
TOTAL:	**3**

Number of Papers published in non peer-reviewed journals:

(c) Presentations

Non Peer-Reviewed Conference Proceeding publications (other than abstracts):

Received   Paper

09/22/2011 17.00 A. Lastufka, Y. Solomon, W. Anderson. Effect of Diluent on Gelled MMH Ignition and Dual Flame
Behavior,
. , . : ,

09/28/2011 18.00 C. Yoon, S. Heister, P. Sojka, C. Watson, G. Xia, C. Merkle. Injector Flow Characteristics for Gel
Propellants,
. , . : ,

09/28/2011 20.00 J. Dennis, C. Yoon, P. Santos, J. Mallory, C. Fineman, T. Pourpoint, S. Son, S. Heister, P. Sojka, O.
Campanella, , . Characterization of Gelling Systems for Development of Hypergolic Gels,
. , . : ,

09/28/2011 21.00 C. Yoon, S. Heister, G. Xia, C. Merkle. Numerical Modeling of Cross-Fed Orifice Flows for Shear-Thinning
Fluids,
. , . : ,

12/30/2011 22.00 S. Snyder, P. Sojka. Secondary Atomization of Elastic Non-Newtonian Drops,
. , . : ,

12/30/2011 23.00 S. Snyder, N. Arockiam, P. Sojka. Secondary Atomization of Elastic Non-Newtonian Liquid Drops,
. , . : ,

    TOTAL: **6**

Peer-Reviewed Conference Proceeding publications (other than abstracts):

Received   Paper

    TOTAL:

Number of Peer-Reviewed Conference Proceeding publications (other than abstracts):

(d) Manuscripts

Received		Paper

04/01/2010   1.00   K. Mooney, S. Menon, D. Schmidt. A Computational Study of Viscoelastic Droplet Collisions,
(04 2010)

08/03/2011 10.00   S. Menon, K. Mooney, D. Schmidt. Parallel adaptive simplical re-meshing for deforming domain cfd computations,
(08 2011)

08/03/2011 12.00   K. Mooney, S. Snyder, P. Sojka, D. Schmidt. Simulation and Experimental Studies of Shear-Thinning Droplet Breakup,
(08 2011)

08/03/2011 11.00   Teixeira, Andrew R.; Mooney, Kyle G.; Kruger, Jacob S.; Williams C. Luke; Suszynski, Wieslaw J.; Schmidt, Lanny D.; Schmidt, David P.; Dauenhauer, Paul J.. Aerosol generation by reactive boiling ejection of molten cellulose,
(08 2011)

08/27/2012 26.00   Travis Kubal, Osvaldo Campanella, Steven Son, Timothee Pourpoint, Jacob Dennis. Rheological Characterization of Monomethylhydrazine Gels,
AIAA Journal (05 2012)

09/22/2011 13.00   J. Dennis, T. Pourpoint, S. Son. Ignition of Gelled Monomethylhydrazine and Red Fuming Nitric Acid in an Impinging Jet Apparatus,
(09 2011)

09/22/2011 16.00   K. Cho, T. Hedman, A. Satija, R. Lucht, S. F. Son, T. Pourpoint. High Repetition Rate OH Planar Laser Induced Fluorescence of Gelled Propellant Droplet,
(03 2011)

09/22/2011 15.00   K. Cho, T. Pourpoint, S. Son, R. Lucht. High Repetition Rate OH Planar Laser Induced Fluorescence of Gelled Propellant Droplet,
(09 2011)

09/22/2011 14.00   Y. Solomon, S. DeFini, T. Pourpoint, W. Anderson. Gelled MMH Hypergolic Droplet Investigation,
(09 2011)

09/23/2010   2.00   J. Mallory, P. Sojka. Dynamics of Sheets Formed Using Gelled Propellant Impinging Jets,
(09 2010)

09/23/2010   3.00   J. Mallory, P. Sojka. A Novel Experimental Facility for Impinging Jet Injector Flow Studies,
(09 2010)

09/23/2010   4.00   J. Mallory, S. DeFini, P. Sojka. Formulation of Gelled Propellant Simulants,
(09 2010)

09/23/2010   5.00   S. Menon, D. Schmidt. Supermesh construction for conservative interpolation on unstructured meshes: An extension to cell-centered finite-volume variables,
(09 2010)

09/23/2010   7.00   C. Lopez-Rivera, P. Sojka. Secondary Breakup of Inelastic Non-Newtonian Liquid Drops,
(09 2010)

TOTAL: **14**

Number of Manuscripts:

Books

<u>Received</u>   <u>Book</u>

TOTAL:

<u>Received</u>   <u>Book Chapter</u>

TOTAL:

Patents Submitted

Patents Awarded

Awards

Graduate Students

<u>NAME</u>	<u>PERCENT SUPPORTED</u>
FTE Equivalent:	
Total Number:	

Names of Post Doctorates

NAME   PERCENT_SUPPORTED

FTE Equivalent:
Total Number:

Names of Faculty Supported

NAME   PERCENT_SUPPORTED

FTE Equivalent:
Total Number:

Names of Under Graduate students supported

NAME   PERCENT_SUPPORTED

FTE Equivalent:
Total Number:

Student Metrics
This section only applies to graduating undergraduates supported by this agreement in this reporting period

The number of undergraduates funded by this agreement who graduated during this period: 7.00

The number of undergraduates funded by this agreement who graduated during this period with a degree in science, mathematics, engineering, or technology fields:...... 7.00

The number of undergraduates funded by your agreement who graduated during this period and will continue to pursue a graduate or Ph.D. degree in science, mathematics, engineering, or technology fields:...... 2.00

Number of graduating undergraduates who achieved a 3.5 GPA to 4.0 (4.0 max scale):...... 5.00

Number of graduating undergraduates funded by a DoD funded Center of Excellence grant for Education, Research and Engineering:...... 0.00

The number of undergraduates funded by your agreement who graduated during this period and intend to work for the Department of Defense 0.00

The number of undergraduates funded by your agreement who graduated during this period and will receive scholarships or fellowships for further studies in science, mathematics, engineering or technology fields:...... 0.00

Names of Personnel receiving masters degrees

NAME

Total Number:

Names of personnel receiving PHDs

NAME

Total Number:

Names of other research staff

NAME	PERCENT SUPPORTED
FTE Equivalent:	
Total Number:	

Sub Contractors (DD882)

Inventions (DD882)

Scientific Progress

Technology Transfer

NAME   PERCENT SUPPORTED

FTE Equivalent:
Total Number:

SPRAY AND COMBUSTION OF GELLED HYPERGOLIC PROPELLANTS

Final Technical Report for work Executed Under Grant W911NF-08-1-0171, 2008 MURI Program, Topic# 19, Spray and Combustion of Gelled Hypergolic Propellants for Future Rocket and Missile Engines

Submitted by

Dr. Stephen D. Heister, PI
765-494-5126 (phone)
765-494-0307 (fax)
heister@purdue.edu
Purdue University
585 Purdue Mall
West Lafayette, IN 47907-2088

Other MURI team members (co-PIs):

Dr. William E. Anderson
Dr. Carlos M. Corvalan
Dr. Osvaldo H. Campanella
Dr. Robert P. Lucht
Dr. Timothée L. Pourpoint
Dr. Paul E. Sojka
Dr. Steven F. Son
Purdue University

Dr. David P. Schmidt
The University of Massachusetts, Amherst

Dr. Terrence R. Meyer
Iowa State University

Dr. Phillip Westmoreland
North Carolina State University

Table of Contents

1.0 Project Summary

1.1 Team Composition & Research Organization

This document provides an executive summary of work performed by a Purdue-led team on DoD MURI Project W911NF-08-1-0171 entitled: ***Spray and Combustion of Gelled Hypergolic Propellants for Future Rocket and Missile Engines***. The team was formed in 2008 for the response to MURI RFP and includes participants from Purdue, University of Massachusetts, NC State University, and Iowa State University. Leadership of the team is summarized in Table 1-1.

Table 1-1: Principle Investigators on MURI Team

Name/Title	Organization	Expertise
S. Heister, Raisbeck Distinguished Professor	Purdue University	Liquid injection, atomization (Team Lead)
W. Anderson, Professor of Aeronautics and Astronautics	Purdue University	Gelled droplet combustion (Combustion Group Lead)
C. Corvalan, Associate Professor of Food Science	Purdue University	Non-Newtonian flow atomization
O. Campanella, Professor of Agricultural & Biological Engineering	Purdue University	Non-Newtonian flows, fluid metrology measurements (Gelled Fluid Group Lead)
R. Lucht, Ralph & Bettye Bailey Professor of Combustion in Mechanical Engineering	Purdue University	Combustion and laser diagnostics of combusting flows
T. Pourpoint, Associate Professor of Aeronautics and Astronautics	Purdue University	Hypergolic propellants and large-scale spray combustion
P. Sojka, Professor of Mechanical Engineering	Purdue University	Gelled fluid atomization Gel Fluid Physics Group Lead
S. Son, Professor of Mechanical Engineering	Purdue University	Combustion and droplet combustion
D. Schmidt, Associate Professor of Mechanical and Industrial Engineering	The University of Massachusetts, Amherst	Non-Newtonian atomization modeling
T. Meyer, Associate Professor of Mechanical Engineering	Iowa State University	Optical diagnostics and ballistic imaging
P. Westmoreland, Professor of Chemical and Biomolecular Engineering	North Carolina State University	Combustion kinetics and reduced order modeling

The overall organization of the research tasks performed by this group is highlighted in Fig. 1-1. Tasks 1.1 and 1.2 (highlighted in green in Fig. 1-1) were structured to address *Rheological*

Characterization of Gelled Propellants while Tasks 2.1-2.5 were developed to assess *Non-Newtonian Flow Physics of Gelled Propellants*. Finally, Tasks 3.1-3.4 addressed the *Combustion Physics of Gelled Propellants*. Numerous team members contributed to the various tasks over the 5-year effort.
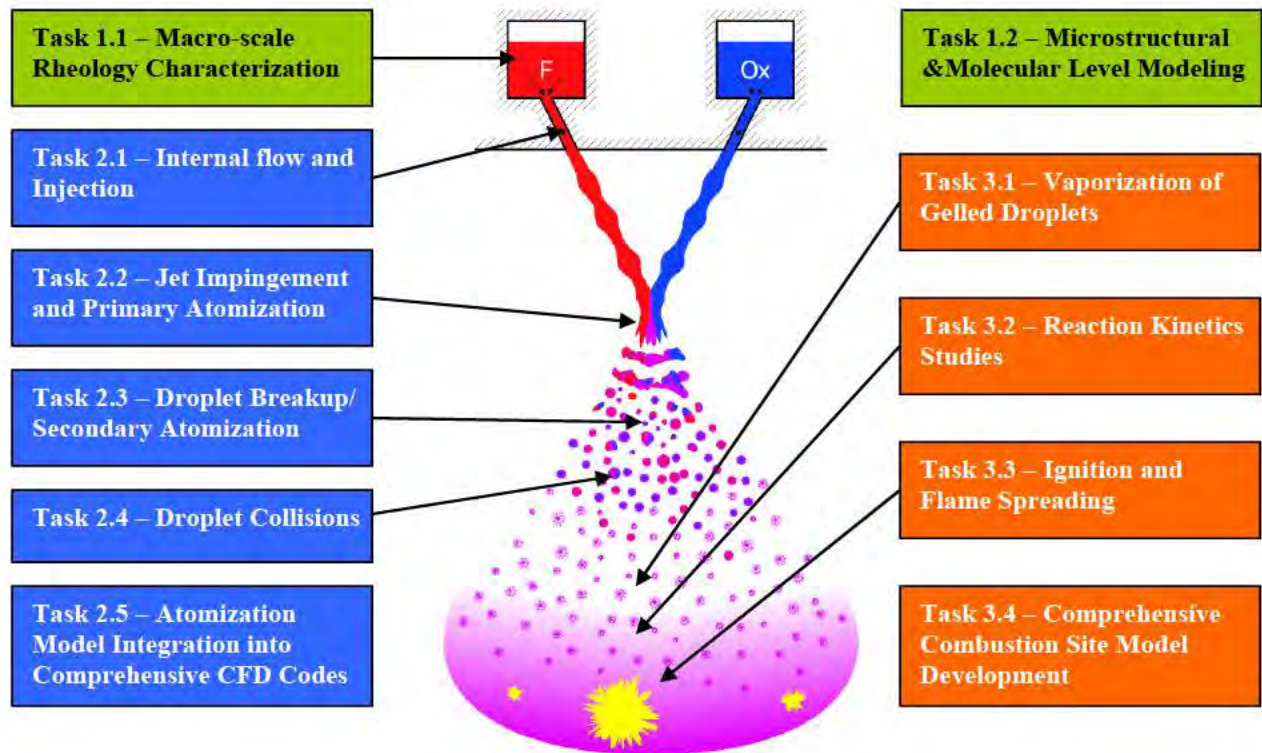
Figure 1-1: Overview of tasks and applicability to a hypergolic injection/ignition flowfield.

Our team included more than 30 graduate students during the 6-year effort. A summary of degrees obtained and post-graduation career placement is included in Table 1-2.

Table 1-2: Summary of Students Employed on MURI Team

Graduated Students	PI	Degree/Grad. Date	Employment
Nat Trask	Schmidt	MS, 8/1/2010	Pursuing PhD at Brown
Travis Kubal	Pourpoint/Son	MS, 5/1/2010	Sandia National Laboratory
Rajeswari Muddu	Corvalan	MS, 8/1/2010	Hewlett-Packard
Celienid Lopez	Sojka	Ph.D, 8/10/2010	Working in Industry
Mark James	Pourpoint	MS, 5/1/2010	SpaceX
Richard Arnold	Anderson	Postdoc thru 2/09	Astrium
Mau DeRidder	Anderson	Postdoc thru 5/10	Spacex
Chenzhou Lian	Merkle	Postdoc thru 8/10	IBM Watson Labs
Changjin Yoon	Heister	PhD, 12/11	GE Global Research Center

Erik Dambach	Heister/Pourpoint	PhD, 5/11	SpaceX
Paulo Santos	Campanella	PhD, 8/11	Ingredion, New Jersey
Dheeraj Kapilavia	Merkle	PhD, 5/11	GE Research Center
Arin Lastufka	Heister/Pourpoint	MS, 5/11	GE Research Center
Sandeep Menon	Schmidt	PhD, 5/11	ANSYS
Robert Janesheski	Son/Pourpoint	MS	Rolls-Royce
Sarah Jo Defini	Sojka	BS	Sandia National Laboratory: ABQ
Nicole Arockian	Sojka	BS	Grad School Gtech
David Shaw	Sojka	BS	Industry
Josh Potter	Sojka	BS	Unknown
Chris Watson	Sojka	BS	Purdue grad school: ME
Ejieh The	Sojka	BS	
Yair Solomon	Anderson	MS, 8/12	Technion
Jordan Forness	Heister/Pourpoint	MS, 5/13	SpaceX
Jennifer Mallory	Sojka	PhD, 5/12	Western New England University
Varun Kulkarni	Sojka	PhD, 8/13	Purdue post-doc
Nicole Labbe	Westmoreland	PhD, ???	Argonne National Labs
Jiakai Lu	Corvalan	PhD, 12/14	Purdue grad school
Clare Fineman	Pourpoint/Son	MS, 8/12	PhD at Purdue
Andreas Zeiner	Pourpoint	MS, 8/13	Germany
Tyler Voskuilen	Pourpoint	Current postdoc	Purdue
Neil Rodrigues	Sojka	MS, 5/14	Purdue grad school
Sharon Snyder	Sojka	PhD, 5/14	Purdue grad school
Necla M. Eren	Campanella	PhD, 12/14	Purdue grad school
Chris Radke	Meyer	PS, 8/12	NASA Johnson Space Center
Ben Halls	Meyer	PhD, 8/14	NRC Post-doc at AFRL
Kaitlyn Weiser	Meyer	BS	Degree expected 2015

Numerous experimental facilities and computational tools were created by the team in order to perform the research. Table 1-3 summarizes these contributions:

Table 1-3: Computational and Experimental Research Infrastructure Developed During MURI Effort

Researcher(s)	Tool/Facility	Reference(s)
Heister, Campanella	Non-newtonian injection dynamics	• Yoon, C., Heister, S.D, and Campanella, 2014. Modeling gelled fluid flow with thixotropy and rheological hysteresis effects, Fuel 128, 467-475
Pourpoint	Gelled Propellants Laboratory design and unlike doublet injector with μs and μm resolution	• J.D. Dennis, S.F. Son, T.L. Pourpoint Critical Ignition Criteria for Monomethylhydrazine and Red Fuming Nitric Acid in an Impinging Jet Apparatus, Submitted to J. Prop. Power, Manuscript ID 2014-07-B35541 • T.L. Pourpoint, J. Dennis, W.E. Anderson, S.F. Son, R.P. Lucht, S.D. Heister, and S.E. Meyer, Design, Development and Operation of a Combustion Test Facility for Monomethylhydrazine and Red Fuming Nitric Acid Gels, JANNAF Meeting, Apr. 2011 • T.D. Kubal, E.M. Dambach, S.F. Son, W.E. Anderson, T.L. Pourpoint, Aspects of Monomethylhydrazine and Red Fuming Nitric Acid Ignition, AIAA 2010-6902
Pourpoint, Heister, Campanella, Anderson	Capillary Viscometer to test gelled propellant and oxidizers at shear rates around 10^6 1/s	• Clare Fineman, Master Thesis, Purdue University • J. Dennis, C. Fineman, C. Yoon, P. Santos, T.L. Pourpoint, S. Son, S. Heister, O. Campanella, Identifying and Characterizing Gelling Systems for Development of Suitable Hypergolic Gels, 4th European Conference for Aerospace Sciences (EUCASS), July 2011 • J. D. Dennis, T. D. Kubal, S.F. Son, O. Campanella, T.L. Pourpoint, Rheological Characterization of Monomethylhydrazine Gels, J. Prop. Power, 29 (2), 2013
Pourpoint, Heister, Lucht, Anderson	Reactive droplets dynamics and combustion	• K.Y. Cho, A. Satija, T.L. Pourpoint, S.F. Son, R.P. Lucht, High-Repetition-Rate Three-Dimensional OH Imaging using Scanned Planar Laser-Induced Fluorescence System for Multiphase Combustion, Applied Optics, 53 (3), 2014 • K.Y. Cho, T.L. Pourpoint, S.F. Son, R.P. Lucht, Microexplosion Investigation of Organic MMH Gel Droplet with 5 kHz OH PLIF, J. Prop. Power, 29 (6), 2013 • E.M. Dambach, Y. Solomon, S.D. Heister, T.L. Pourpoint, Investigation into the Hypergolic Ignition Mechanisms Initiated by Low Weber Number Collisions, J. Prop. Power, 29 (2), 2013 • S.J. DeFini, T.L. Pourpoint, W.E. Anderson, Gelled MMH Hypergolic Droplet Investigation, Y. Solomon J. Prop. Power, 29 (1), 2013 • E.M. Dambach, B. A. Rankin, T.L. Pourpoint, S.D. Heister, Temperature Estimations in the Near-Flame Field Resulting from Hypergolic Ignition using Thin Filament Pyrometry, Comb. Sci. Tech.,184 (2), 2012
Pourpoint, Voskuilen, Westmoreland	Non-newtonian multiphase combustion model	• T. Voskuilen, C. Needham, P. Westmoreland, T. Pourpoint, Predictive Modeling of Hypergolic-Propellant Performance. Part II: Ignition of Hypergolic Liquids and Shear-Thinning Gels of Monomethylhydrazine and Fuming Nitric Acids, In Preparation, Sept. 2014

Meyer	2-D high-speed X-ray radiography and 3-D X-ray tomography	• B.R. Halls, T.J. Heindel, A.L. Kastengren, and T.R. Meyer, Evaluation of X-ray sources for quantitative two- and three-dimensional imaging of liquid mass distribution in atomizing sprays, Int. J. Multiphas. Flow 59, 2014 • B.R. Halls, T.R. Meyer, A.L. Kastengren, Quantitative measurement of binary liquid distributions using multiple-tracer x-ray fluorescence and radiography, submitted to Opt. Express, 2014 • B.R. Halls, S. Roy, J.R. Gord, A.L. Kastengren, and T.R. Meyer, Quantitative flash x-ray imaging of liquid mass distribution in impinging liquid jets, in preparation, Atomization Spray, 2014 • C.D. Radke, P. McManamen, A.L. Kastengren, B.R. Halls, and T.R. Meyer, Quantitative measurement of gas and liquid distributions using x-ray fluorescence and radiography in atomizing sprays, submitted, Opt. Lett., 2014
Schmidt	Diffuse-interface primary atomization model	• J.M. García-Oliver, J.M. Pastor, A. Pandel, N. Trask, E. Baldwin, and D.P. Schmidt, "Diesel Spray CFD Simulations Based on the Sigma-Y Eulerian Atomization Model," *Atomization and Sprays,* 23(1), pp. 71-95, 2013.

1.2 Overview of Flow/Combustion Physics Associated with Gelled Combustion Events

The combustion of hypergolic propellants is one of the most complex physical-chemical processes known to man with complex multiphase flow interactions occurring simultaneously to vastly complex chemical reactions leading up to a combustion event. It is challenging to gain fundamental knowledge of the processes in hypergolic combustion because it is impossible to distinguish between the chemistry and fluid mechanics involved in these violent and highly transient ignition events. Early work was largely empirical: a variety of screening tools such as drop tests or impingement tests were used to assess ignitability and the influence of propellant composition and operating conditions on the ignition behavior. Lacking high speed computational power, researchers developed quasi-analytic treatments to investigate droplet evaporation, mixing, and ignition processes with the goal of providing a design capability. High-speed film cameras provided some glimpse of the millisecond time-scale events. Here we focus on recent knowledge gained from modern tools; the interested reader is referred to reviews of the classic literature.

The ever-increasing capability of modern high-speed cameras and other diagnostics, combined with improving computational power, has allowed significant advancements in the understanding of hypergolic combustion physics. While the kinetics associated with the nitric acid/hydrazine system is daunting, computational tools are now progressing with reaction sets including over 500 intermediate reactions. Recent observations with high speed cameras and other instrumentation have provided an understanding of microsecond-level events and helped uncover the role of liquid phase and droplet atomization/explosion processes revealing micron-scale

features not observed with prior tools. The observation of micron-scale gas layers between sheets of impinging liquids has provided another area of study. As a result of these advances, our current view of the hypergolic ignition/combustion event has evolved to include these new focus areas.

Figure 1-2 highlights many of the processes and features one might observe or envision in a hypergolic ignition event. The lion's share of engines incorporating hypergolic propellants utilize the impinging element injection concept as is highlighted in Figure 1-2. While the non-Newtonian physics community is rich with many applications in chemical engineering, agricultural engineering, and food science, these industries to not push on the gelled substances nearly as hard as we push a fluid in a rocket injector. Injection pressure drops in the rocket application can easily exceed 30 atmospheres, as the atomization requirements are significant to provide fast combustion required in the rocket application. For this reason, the group significantly advanced understanding of high shear physics applicable to characterization and injection of these fluids as described in Sections 2 and 3 of this report.

Impact waves have long been known to be a major observable feature of an impinging jet collision, yet their origin is still of some debate. These waves are very important as ligaments and eventual droplet formation tends to scale from these features. Instability of the stagnation point and classical free surface instabilities (Kelvin-Helmholtz and Rayleigh-Taylor) are potential contributors as is unsteadiness from the injection process itself. Section 4 of this report summarizes the knowledge gained in this critical area.

Droplet collisions are inevitable in the dense sprays formed near the impact location and their outcomes contribute to subsequent chemical reaction events. Collision of unlike droplets produces vigorous gas production thereby providing precursor intermediate species for a subsequent ignition event. Combustion of individual gelled droplets within the dilute regions of the spray contributes significantly to the overall time required for complete combustion. Knowledge gained in these droplet-related areas is highlighted in Sections 5, 6 and 7 of this report.

A less-discussed feature, highlighted in Fig. 1-2, is a very thin gas layer that separates the two propellants as they form the respective undulating fuel and oxidizer sheets. To our knowledge this feature (which is exaggerated for clarity in Fig. 1-2) has never been imaged, although we theorize that it must be present because the two liquids cannot lie directly adjacent to each other without producing large amounts of gases. We know from early experimental concepts aimed at studying hypergolic ignition that coaxial arrangements were discarded as mixing was poor, probably because a gas layer separated the two propellants. Both liquid and gas-phase kinetics create highly complex reaction pathways that govern overall combustion time. Our progress made in understanding these processes is highlighted in Section 8 of this report.

The overall combustion field serves as an aggregate of these individual processes. Our work in resolving inter-related processes in the overall field is summarized in Section 9 of this report.
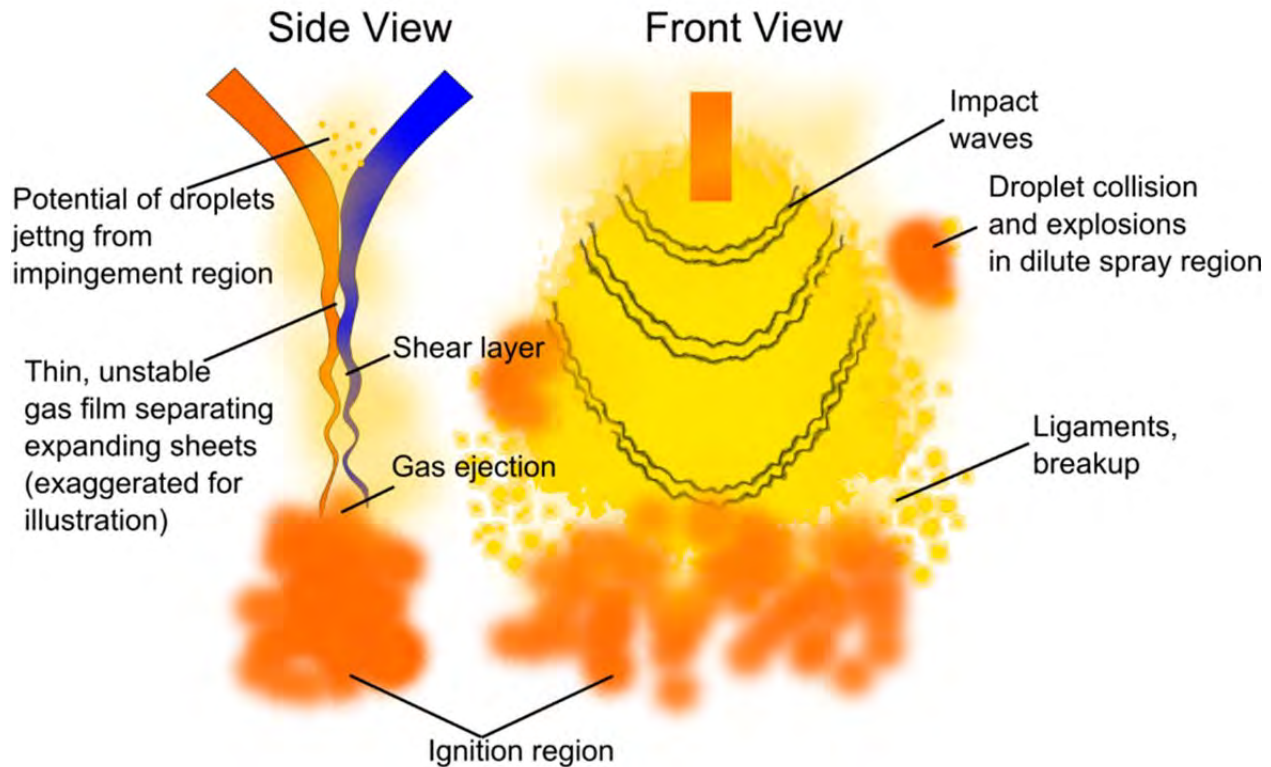
**Figure 1-2: Schematic of impinging jet hypergolic ignition highlighting important physical processes**

2.0 Rheology of Gelled Propellants

Gelled propellants offer a number of advantages compared to liquid and solid rocket propellants, which include high performance, wide-range thrust control and reignitability, and solid-propellant type of storage behavior and safety aspects as gels can be stored like solids in the propellant tank, with a very good leakage behavior in terms of spillage and with a ruptured tank Structure. Gels also provide the potential to add insoluble metallic particles such as aluminum, magnesium, or boron in the gel composite with minimum particle-settling to increase energy density of the propellant and engine thrust [1,2,3]. Thus, three aspects related to the rheology of gels and with application to hypergolic gels were taken into account; they are: (1) viscoelastic properties of the gel, its effects on drop formation and collision, including the gel plastic behavior and the presence of yield stress (2) time dependence of the gel rheology, specifically thixotropy, and its effects on the flow of gels and (3) rheological behavior of the gels at extremely high shear rates (10^6 1/s).

Concerning these aspects, initially and until the construction of Zucrow laboratories and safety requirements were approved by the University we worked with gel simulants prepared with the jet propellant JP-8, the rocket propellant RP-1 gelled with fumed silica (CAB-O-SIL® M-5).

Several properties of the gels preparation such as mixing as well as gel stability and gel characterization were assessed.

Mixing process and gel stability: A comparison between a conventional low-shear and an acoustic high-shear mixing technique (Resodyn ResonantAcoustic® was carried out to determine the influence of the mixing process on the final gel quality and stability. Considerable advantages were observed when gels were prepared with the acoustic mixer due to the uniform shear applied during the mixing conditions used in this mixer. Better mixing performance translated on the measured rheological properties which are illustrated in Figure 2-1 below:
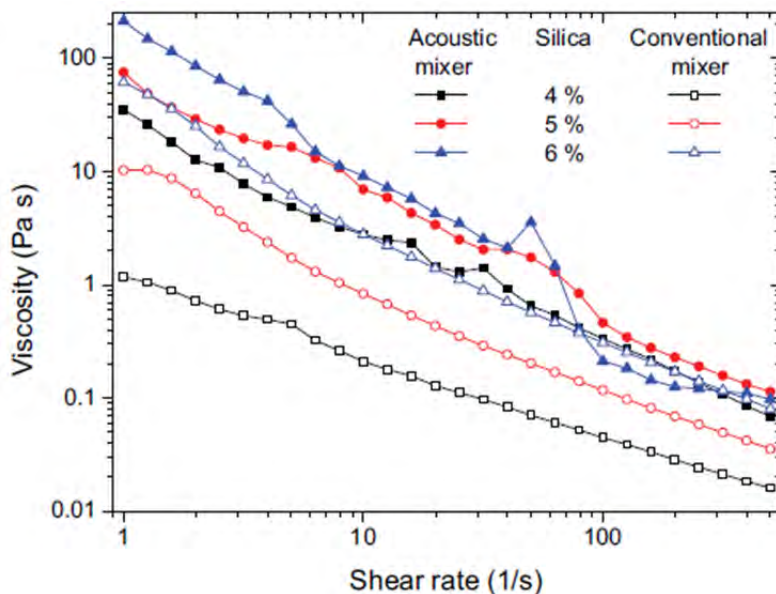
Figure 2-1: Comparison of high shear acoustic and conventional mixing process for JP-8 and silica.

The figure shows a comparison of the high-shear acoustic and conventional mixing for the JP-8 jet fuel using 4, 5, and 6% fumed silica. Conditions used during the mixing in both mixers can be found in Reference 4. As observed in the figure for shear rates in the order 1 – 10 1/s differences in measured viscosities of gels prepared in the acoustic and the conventional mixers are very significant with viscosities of more than one order of magnitude higher when gels were prepared in the acoustic mixer for all the silica concentrations. Results also showed that the acceleration used for the mixing had little effect on the resulting resonance frequency and the acceleration applied during the mixing and these values remain constants after 10-15 seconds of mixing [4]. Other results showed the effects of mixing shear rate (conventional mixer), acceleration (acoustic mixer) and mixing time on the viscosity of the gel. It was clearly shown that mixing time decreased the viscosity. It was speculated that high mixing times can affect hydrogen bonding binding the silica particles thus decreased the viscosity of the gels. This effect of shear on the gel structure was found to be irreversible and with little possibility of recovery within the characteristic times of relevance to the flow of hypergolic gels. This phenomenon translates into the observed time dependence of the gel rheology, a behavior known as thixotropy. Thixotropic effects not only affect the rheological characterization of the gels but also strongly influence their flow behavior [5].

Rheological properties: As discussed above the safety and potential performance advantages of gelled propellants make them attractive for future propulsion systems. More specifically, gelled propellants are shear-thinning liquids whose viscosity decreases as the applied shear rate increases, known as shear thinning fluids. At low shear conditions the gel viscosity is high and the fluid does not flow or flows very slowly, reducing the risk of leaks. Thus, the yield stress of the formed gels is also a functional property of the gel associated not only to their stability but also to their no-flow conditions over storage. In addition the energy density of gelled propellants can be increased by adding energetic particles, such as aluminum or other metals into the gel. Thus the gel structure has to support these particles without sedimentation concerns that commonly arise during use of slurry propellants. The combustion of the metal particles increases the combustion temperature of the propellant and therefore the specific impulse, assuming the molecular weight of the combustion products does not increase enough to offset the temperature increase. We characterized the rheological properties of unloaded Mono methyl hydrazine (MMH) gelled with hydropropyl cellulose (HPC) and Red Fuming Nitrogen Acid (RFNA) gelled with silica. Rheological measurements were performed for various gel formulations and along the viscosity-shear rate relationship the yield stress of these gels were explored. The viscosity-shear rates relationships were described by various models that depended on the presence or absence of yield stress. The models tested were:

The Power Law Model (PL)

$$\eta(\dot{\gamma}) = m\dot{\gamma}^{n-1} \tag{2.1}$$

where m is a measure of the magnitude of viscosity known as the consistency index and n is a measure of the degree on non-Newtonain viscosity variation with shear rate known as the power-law index. The power-law index is 1 for Newtonian liquids, between 0 and 1 for shear-thinning liquids, and greater than 1 for shear-thickening liquids.

Carreau-Yasuda Model (CYM)

For applications where very low or very high shear rates, e.g. in pumping systems or rocket injectors, are encountered the power-law model breaks down because $\lim_{\dot{\gamma}\to 0}\eta(\dot{\gamma}) \to \eta_0 \ or \ \infty$ and $\lim_{\dot{\gamma}\to\infty}\eta(\dot{\gamma}) = \eta_\infty$. For these materials, the viscosity versus shear rate relationship is well described by the Carreau-Yasuda model, which is given by the following equation:

$$\eta(\dot{\gamma}) = (\eta_0 - \eta_\infty)\cdot\left(1 + (\lambda\dot{\gamma})^a\right)^{\frac{n-1}{a}} + \eta_\infty \tag{2.2}$$

where η_0 is the lower shear Newtonian plateau viscosity, η_∞ is the upper shear Newtonian plateau viscosity, and a, n, and λ are curve fitting parameters. The Carreau-Yasuda model is used with η_0 determined either by fitting or experimentally at low shear rates and η_∞ is measured using high shear capillary viscometers. Often is incorrectly assumed that the viscosity η_∞ is that of the ungelled liquid propellant but this research, using a specially designed capillary viscometer, has demonstrated that the assumption is far from reality as measured values of gelled propellant materials showed significantly larger viscosity than the viscosity of the single liquid propellant. This finding has several implications not only on the flow of the gelled propellant but also it may largely influence combustion reactions.

Herschel-Bulkley (HB) and extended Herschel-Bulkley (HBE) models

The lower constant viscosity (Newtonian) plateau is not detected for materials with a measurable yield stress. For these high yield stress materials one of its important flow characteristics, such as plug flow in conducts, are not captured with the power law and the Carreau Yasuda models. Plug flow occurs when the shear stress applied to the material is below the yield stress of the fluid, resulting in a solid plug of gelled propellant moving through the flow field. A model describing that behavior is the Herschel-Bulkley model given by the equation:

$$\eta(\dot{\gamma}) = m\dot{\gamma}^{n-1} + \frac{\tau_y}{\dot{\gamma}} \tag{2.3}$$

where τ_y is the yield stress of the material. It was proposed for hypergolic to include a constant viscosity term to the HB model to force the viscosity at high shear rates to converge to an upper Newtonian plateau [6], which as discussed above is not equal to the ungelled propellant. The model is called the extended Herschel-Bulkley and is given by the following equation:

$$\eta(\dot{\gamma}) = m\dot{\gamma}^{n-1} + \frac{\tau_y}{\dot{\gamma}} + \eta_{\infty} \tag{2.4}$$

The HBE model accounts for shear-thinning behavior, yield stress, and the upper Newtonian plateau, all of which are relevant to the internal flow and high shear rates existing in rocket injectors.

These models were tested to describe the rheological properties of MMH and RFNA gels produced with HPC and silica respectively, which are shown below:

MMH Gels

(a)   (b)   (c)
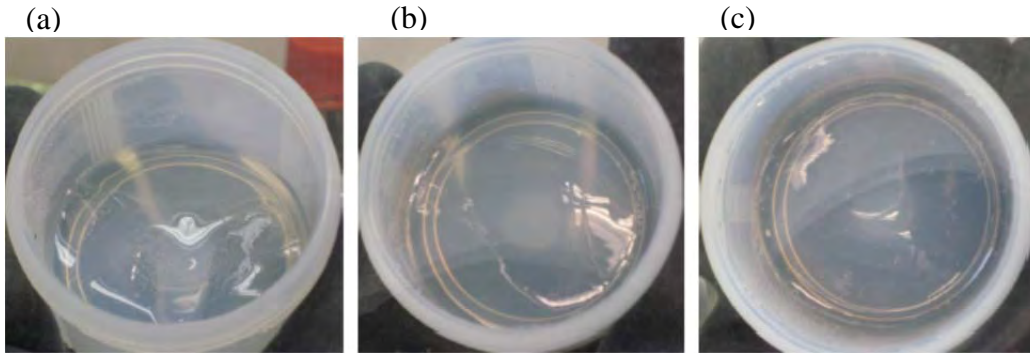
Figure 2-2. Gelled MMH with 4% HPC after: (a) 2 days, (b) 5 days and (c) 7 days

HPC does not require high shear to form a polymeric network since it able to form its network by dissolving into the solvent (MMH in this case) and by diffusion, so in theory only time is needed. To make the HPC/MMH gel, HPC was added to the MMH and the mixture was stirred thoroughly by hand. The mixture was then allowed to sit for one week and was stirred by hand twice in between. After the one week time period the gels appeared uniform and well mixed. Figure 2-2 shows the evolution of a 4% HPC/MMH gel at various stages in the mixing process. It is important to note HPC tends to clump when added to a solvent like water, and that behavior was also observed when mixed with MMH. The mixture in Figure 2-2(a) contains a large clump

of HPC in the center identified by the presence of small bubbles. In Figure 2-2(b) most of the bubbles have dissapeared, but an outline of the HPC clump is still visible. From Figure 2-2(c) it is clear the HPC has difused throughout the entire mixture. Given the importance of the yield stress during storage and the flow, the yield stress in the gel was generated by introducing fumed silica (Cabosil[c] M5) into the mixtures. The total gelling agent concentration was held constant at 5% by mass for the silica/HPC/MMH gels while the concentration of silica was varied from 1 to 3%. Ideally, the amount of silica should be minimized because it is inert and adds no energy to the system. The mixing procedure with silica was similar to the HPC/MMH gel procedure. When only 1% silica was used, the silica was able to be completely stirred into the mixture by hand. When 2 and 3% silica were used hand mixing was not adequated so the mixing was performed on a LabRAM mixer using a setting of 100% intensity. Further details of the procedure and testing can be found elsewhere in Reference 7.

RFNA Gels

RFNA gels can be prepared using fumed silica as the gelling agent with concentrations from 3 to 5% (w/w) [8,9,10]. The inert nature of the inorganic fumed silica makes it one of the few gelling agents that will not react with RFNA. The surface of fumed silica is hydrophilic, meaning that absorbs water readily from the surrounding environment. The amount of moisture absorption on the fumed silica surface correlates directly to the ambient humidity, and can reach 12% by weight at an atmospheric humidity of 90%., Thus, silica was dried in a vacuum oven at $110^{o}C$ and a pressure of 138 mbars for at least four hours prior to use to ensure the silica had minimal water content. The mixing procedure was based on previous work in this project [11,12].

The gels were mixed in a LabRAM mixer at 100% intensity and acceleration of 100 g's for one minute. The aforementioned work had found that mixing for shorter times or mixing at lower intensity did not produce an adequate gel and mixing for longer times would break the gel structure. The mixing method was found to be adequate and produced well-mixed and consistent RFNA gels. A typical RFNA gel is shown in Figure 2-3.


Figure 2-3. Typical 5% silica/RFNA gel

Rheological Results – Low and intermediate shear rates – yield stress determination

Steady Shear Viscosity MMH gels
A typical viscosity-shear rate measurement result for a 3% HPC/MMH gel mix is illustrated in Figure 2-4. The viscosity curves clearly show the lower Newtonian plateau at very low shear rates and the transition to the power law region as the shear rate increases. As observed in the figure after testing 9 replicates the variation in viscosity from sample to sample was small and the percent deviation of all measurements was within 10% of the average viscosity of the mix shown. This result was typical for the 3% HPC/MMH gels, however as the HPC concentration was increased and silica was added, the variation in the viscosity within each mix increased.

The viscosity-shear rate curves were fitted with the power law (PL) and Carreau Yasuda (CYM) models. It was observed that the PL model over predicted the viscosity at low shear rates whereas the CYM converged to the lower Newtonian plateau viscosity. Fitting parameters for the studied systems are given in Reference 7.
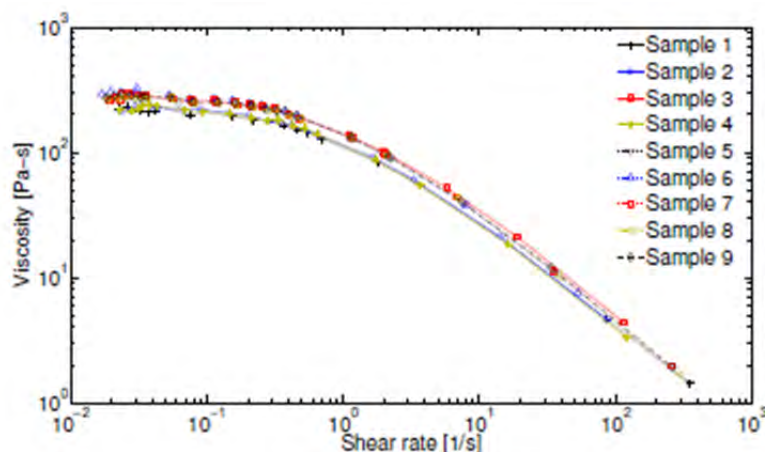
Figure 2-4. Raw data from viscosity-shear rate measurements for a 3% HPC/MMH gel

Yield Stress Measurements
When a stress is applied to a fluid below its yield point elastically deforms and the strain is linearly proportional to the applied stress. Above the yield stress, the stress is proportional to the shear rate and the fluid flows. The yield stress point can be identified as a change in the slope of the strain-stress curve as shown in Figure 2-5. As indicated in the figure the yield stress was determined by increasing the shear stress incrementally until the strain-stress relationship becomes nonlinear (see below).
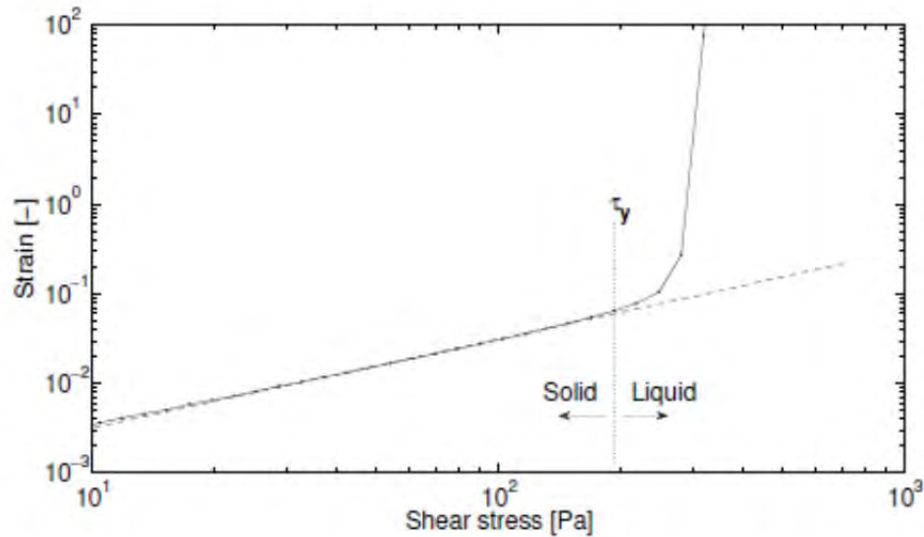
Figure 2-5. Stress-strain curve indicating the determination of the yield stress τ_y

In the case of MMH gels all have negligible yield stresses but using a proper mixing procedure and the right balance HPC/silica it was possible to create a MMH gel with appreciable yield stress. Considering the decrease in energetic content of the gelled fuel using silica new developments with more energetic gelling agents that may provide a significant yield stress may represent a better direction for future research. Further details on the rheology of MMH, specifically on the effects of the gelling agent concentration and decomposition of the gels are given in Reference 7.

Steady Shear Viscosity RFNA gels
Viscosity versus shear rate of RFNA gels prepared with 3% and 4% silica are shown in Figures 2-6 and 2-7:
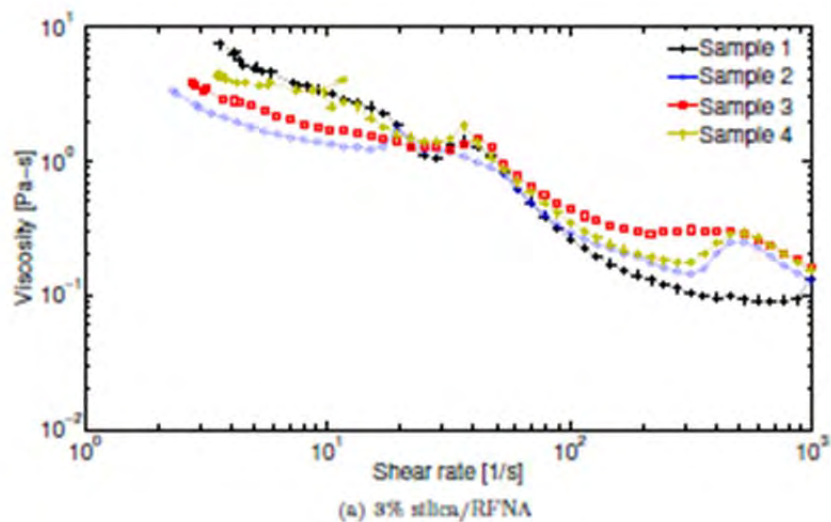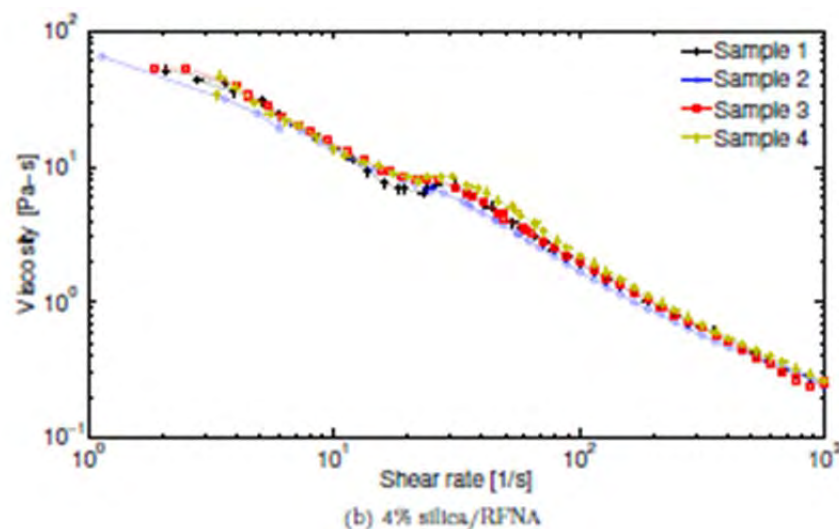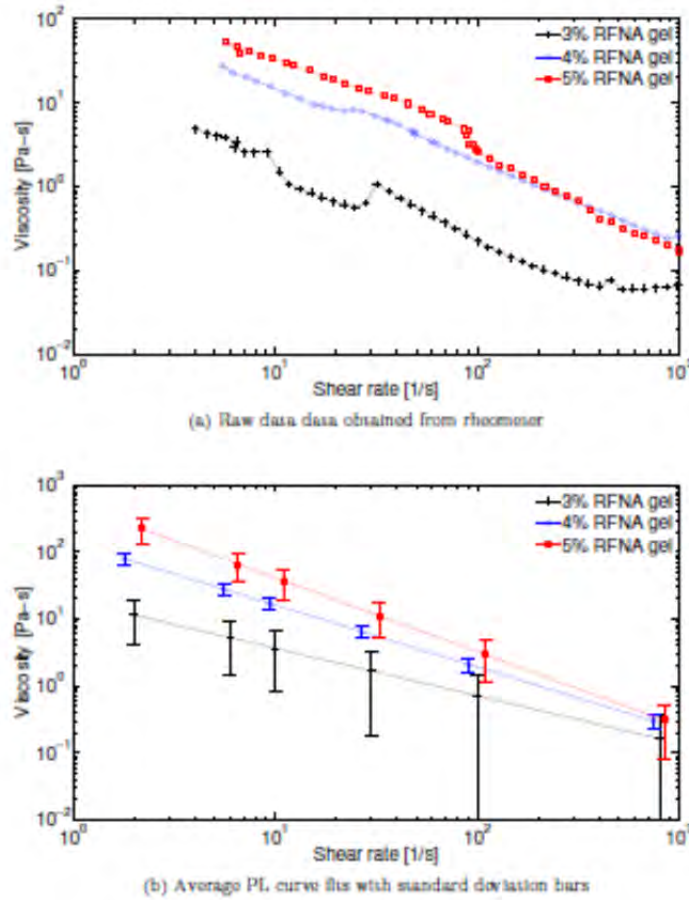

(a) 3% silica/RFNA

Figure 2-6. Raw data from viscosity-shear rate measurements for two silica/RFNA gels; 3% silica

Figure 2-7. Raw data from viscosity-shear rate measurements for two silica/RFNA gels; 4% silica

The results shown are typical of the gels prepared in a single mix. But Figure 2-6 clearly shows an atypical behavior for the 3% silica/RFNA gels compared to the 4% silica/RFNA gel (Figure 2-7). The viscosity does not decrease uniformly with shear rate, instead it tends to oscillate. The reason for this behavior is unclear, but it was observed for all the 3% silica/RFNA gels. A possible explanation comes from the consistency of the gels. The 3% silica/RFNA gels were different from the 4 and 5% gels and were generally very fluid. Conversely, the 4 and 5% gels would not flow under their own weight and would remain suspended on an inverted spatula. Thus, any deformation applied during the gel handling was probably affecting the structure of these weak gels and thus affecting their measured properties rheological. Local deformations could have also created zones with different properties given place to the oscillation during testing.

The change in viscosity of gels prepared with different silica concentrations are shown in Figure 2-8 including a power law fitting of the data. As noted the variability is very large.

(a) Raw data data obtained from rheometer

(b) Average PL curve fits with standard deviation bars

Figure 2-8. Comparison of viscosity versus shear rate results for 3, 4, and 5% RFNA gels

It is clear from Figure 2-8 that increasing the gelling agent concentration increases the viscosity of the gel, represented by the consistency index parameter *m* from the PL model. A less obvious trend is observed with the PL parameter flow index *n*, which appears to decrease with increasing gel concentration. Smaller flow indexes *n* mean that the gels become more shear-thinning as the gelling agent concentration increases. The increased viscosity is explained by the increased number of silica particles bonding together, making the gel more resistant to flow. The increased shear-thinning behavior is attributed to the increase of silica-silica bonds. More silica-silica bonds means more bonds are broken due to the shear flow. The more silica-silica bonds are broken the further the viscosity decreases. It is interesting to see that the viscosities of all the gels are similar at a shear rate of $1000\ s^{-1}$ because at those high shear rates the gel network is almost completely disrupted. The PL curve fits reasonably well all viscosity-shear rate measurements as indicated in the Table 2-1. The variation in the PL model parameters varied from 19 to 58% for the consistency index *m*, and 44 to 88% for the PL flow index *n*.

Gel Concentration	m (Pa.s^n)	COV (%)	$n(-)$	COV (%)
3%	18.8	58	0.29	44
4%	138.4	19	0.072	64
5%	533.9	39	-0.107	88

Table 2-1. Summary of the rheological results obtained on RFNA gelled with different concentrations of silica. Values given in table are average values and COV indicates the coefficient of variance of the results measured in percentage.

The thixotropic behavior of the RFNA gels may in part explain the large variations observed. Thixotropy means the gels are time-dependent and highly dependent on the shear history applied to them. The process of mixing, handling, and loading each sample onto the rheometer may provide each sample with different shear histories that are reflected in the viscosity measurements. For hypergolic gels the structure of the material is not reformed within appreciable time. Earlier discussion about the PL model stated the condition $0 < n < 1$ for shear-thinning liquids. However, values of $n < 0$, which are obtained in the 5% silica/RFNA gels are indicating that the PL model (that assumes time-independent rheological properties or gels that have structures which are reformed immediately after the shear deformation is ceased) is inappropriate.

Results show that RFNA gels are time-dependent, i.e. thixotropic materials. The rheometer measurement process relies on the liquid being at steady-state flow for each measurement point. The RFNA gels never reach that steady-state because thixtropic effects make impossible to reach a steady-state condition as the liquid viscosity is continuously decreasing even at constant shear conditions. The effect of the always decreasing viscosity drives the viscosity lower than that the PL model prediction resulting in negative n flow indices. The negative n value was observed for the 5% silica/RFNA gels because the shear-thinning behavior increases with increasing silica concentration and in addition to the thixotropic effects. A measurement technique that can be used to eliminate, or lessen thixotropic effects relies on pre-shearing the sample.

The effect of thixotropy on hypergolic gels is schematically illustrated in Figure 2-9. As observed in the figure, where the measured shear stress is plotted as a function of the shear rate, the consequence of the shear applied during the test is the breakage of the gel structure, thus for each shear rate the structure of the gel is changed. Instead of the traditional shear stress versus shear rates indicated by full lines in the figure a behavior as the dashed line is observed. It must be noted that simple liquids may also a disturbance on their structures when shear is applied effect but the recovery of the structure is so fast that it can be safely assumed that the structure of the liquid does not change when the shear rate is changed. In other words the material reaches very quickly a steady state in where the measured local shear stress and viscosity are only a function of the applied shear and not a function of time or the shear history.

Thixotropic materials, on the contrary, have a structure that does not recover immediately so once the corresponding shear stress (or viscosity) is measured at a new shear rate or a different time the material has changed and the measurement depends on the shear history (or time). The sum of shear thinning and thixotropic effects results in negative flow indexes when the PL model

is applied. Thus, to model the flow characteristics of thixotropic fluids rheological models that include both shear thinning and time effects must be used. An attempt to develop these types of models was performed in this project and were able to predict better the flow characteristics of hypergolic gels when compared with predictions that used time-independent rheological models like the PL, HB, HBE and Carreau Yasuda models [5].

.
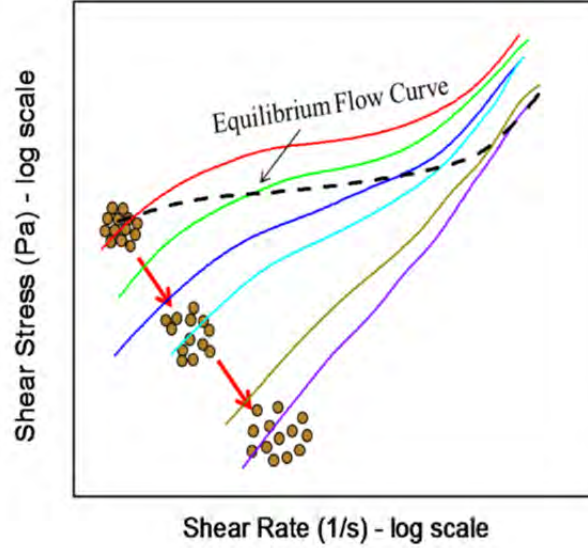
Figure 2-9. Schematic of the rheological behavior exhibited by a thixotropic fluid expressed in a shear stress-shear rate plot

Viscoelastic Properties of Gels

The viscoelastic properties of the gels were determined using oscillatory small strain tests. These tests are based on the application of either a sinusoidally time-varying strain or stress. For the case in which the strain is controlled the following shear strain is applied to the sample.

$$\gamma(t) = \gamma_0 \, sin \, \omega t \tag{2.5}$$

where $\gamma(t)$ is the instantaneous strain, ω is the frequency of the oscillation, γ_0 is the amplitude of the strain and t is time. As a consequence of that strain the stress response of the material under strains that are within the lineal viscoelastic region of the material is:

$$\tau(t) = \tau_0 \, sin(\omega t + \delta) \tag{2.6}$$

where $\tau(t)$ is the instantaneous stress, τ_0 is the amplitude of the stress and δ is the phase angle that measures the shift angle between the strain and stress oscillations. It can be shown that when $\delta = 0$ the material behaves as a perfect elastic material whereas when $\delta = 90^\varrho$ the material behaves as a pure liquid. Values of $0 < \delta < 90^\varrho$ correspond to viscoelastic materials. From these measurements three typical viscoelastic parameters can be determined; they are the storage modulus G', the loss modulus G'' and the phase angle δ (or $tan \, \delta = G'' / G'$) which provide information on the mechanical behavior of the material. In this project these parameters were used to establish the signature of the gelled propellants. Two types of tests were carried out. One

test, in which the amplitude of the strain was varied at a constant oscillation frequency and the above defined viscoelastic parameters determined, was performed to characterize the strength of the gels formed. The test is known as a strain sweep test and is commonly used to determine the range of the viscoelastic behavior of the material. Results of these tests are illustrated for a 3% HPC/MMH gel, a 6% silica/MMH gel and a 2%HPC+and 3% silica/MMH gel (identified as hybrid gel) in Figure 2-10. The oscillation frequency used was 5 Hz. Given the elastic nature of the gels only the storage modulus G'' and the phase angle δ are plotted.
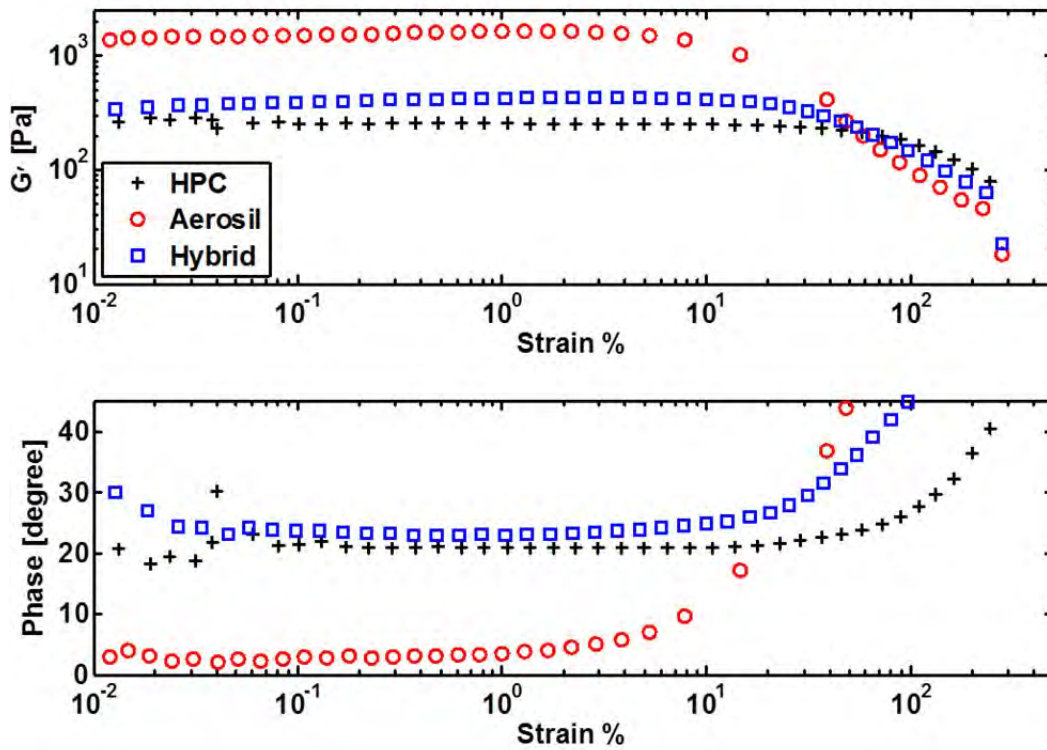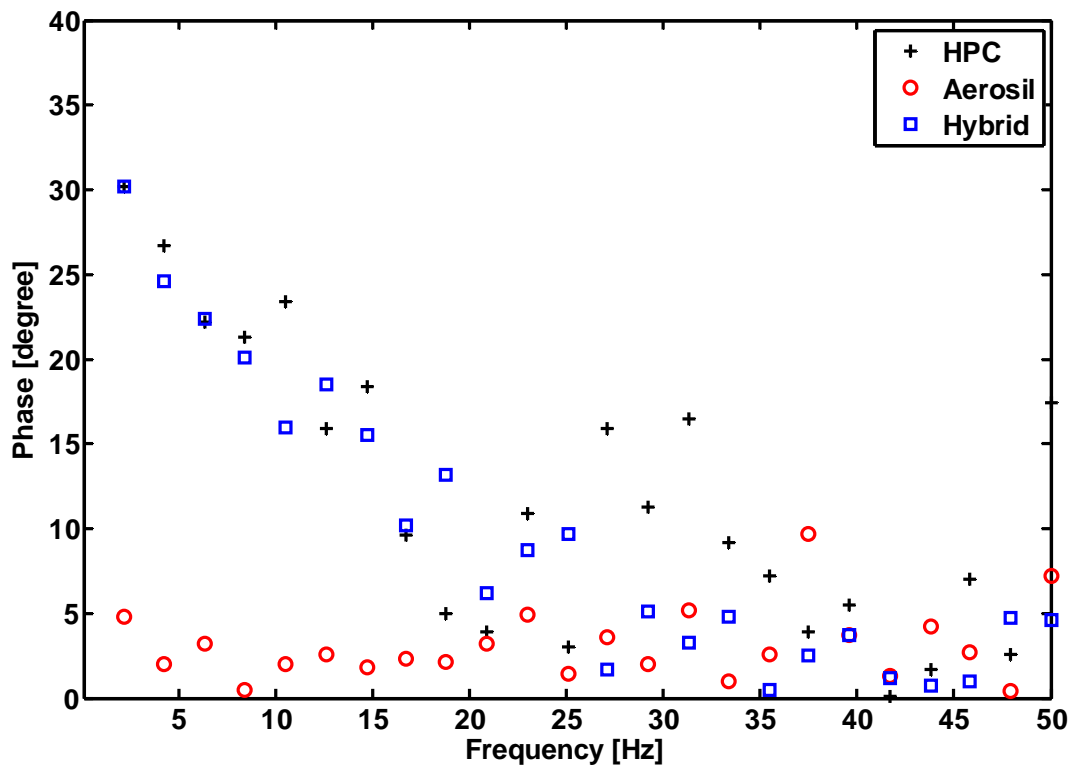

Figure 2-10. Strain sweep viscoelastic tests for three different types of gels

Results show that gels prepared with silica (particle gels) had larger strength (higher G') and were more elastic (lower phase angle δ) than gels prepared with HPC (polymeric gels) and gels prepared with a mix of silica and HPC (hybrid gels). However, particle gels were more fragile and their structure was broken at lower strains γ than the HPC made polymeric gels and hybrid gels. That is evidenced by the strain where the storage modulus (or the phase angle) is no longer constant and decreases (or increase) with the strain.

The other test, known as frequency sweep, is performed at a constant strain (within the linear viscoelastic region of which is previously determined in the first test) and the frequency of the oscillation is varied. Behavior of the gels at different frequencies can be physically related to their functionality. For instance the viscoelastic behavior at low frequencies is associated to long duration events like for example storage or pumping of the gels. Whereas the viscoelastic behavior of gels at high frequencies is associated to short duration events like for example during injection or impingement of the gels.

Figure 2-11 shows results of the frequency sweep tests for particle, polymeric and hybrid gels. It can be observed that polymeric and hybrids gels have a typical viscoelastic behavior which consists in a decrease in the phase angle with increases in frequency which would be indicating that the elasticity of the gel increases with the oscillation frequency. Conversely particulate gels exhibited an elastic behavior that is independent on the frequency, i.e. they act as true elastic materials until the structure of the gel is broken. It is important to note that these experiments were performed at low strain (0.1%), i.e at a strain under which the structure of the gels is assumed do not be disturbed for the shear deformation. However, under flow conditions the structure of these gels are broken and, depending on the type of gel, it may reform. It was observed that polymeric and hybrid gels tend to reform their structure. Conversely, particle gels do not reform their structure after it is destroyed by the shear flow despite particle gels have higher strength and are more elastic when their properties are measured at low strains.


Figure 2-11. Frequency sweep viscoelastic tests for three different types of gels

These different rheological behaviors seem to be related to the behavior of the gels during combustion tests. It was observed that MMH polymeric gels did not ignite and were difficult to atomize in small droplets, instead a sheet was observed during injection. On the contrary MMH particle gels ignited and atomize forming single droplets. The hypothesis obtained from these experiments is that under flow conditions polymeric gels exhibit a typical viscoelastic behavior characterized by longer relaxation times than those determined for particle gels which were extremely short. The main distinction between polymeric and particle gels is their behavior under flow. The structure of the polymeric gels is broken during flow, but some of that structure is able to reform in short times inducing some degree of viscoelasticity to the material and thus affecting the material atomization. This phenomenon is not new as during atomization of polymeric

dispersions during spray drying of viscoelastic material there are many practical problems to form uniform droplets. Conversely, particle gels are very elastic at low deformation, have high yield stress, i.e. they do not flow under low shear strains, but their structure is broken and they are very fluid at high shear rates (i.e. during flow conditions). The structure of these particle gels is not recovered rapidly and they continue having a liquid behavior with little viscoelasticity so their atomization is greatly facilitated.

Figure 2-12 schematically illustrates the importance of the different rheological tests to characterize the functional property of the gels. The singular importance is the rheological properties of the gels at shear rates similar than those existing during injection, identified in the figure as "*High Shear Viscometry*". Initial experiments to test gels at high shear rates were performed in a commercial capillary viscometer (Bohlin-Rossand from Malvern Instruments) and the samples were simulants. Due to the fact that the laboratory was not authorized for testing MMH and RFNA containing materials all tests were performed on polymeric and particle simulants gels. Shear rates reached during these measurements were around 10^5 1/s. The procedure developed in this commercial capillary viscometer was used for calibration of a capillary viscometer that was built during this project for testing real hypergolic gels. Description of this built capillary viscometer is given in next section.
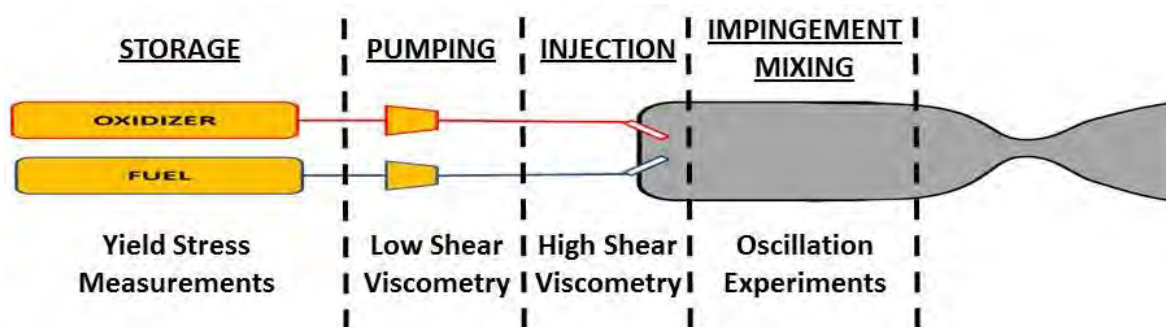
Figure 2-12. Schematic illustrating the importance of the different measured properties

High Shear Rheology – Building of capillary viscometers to characterize the properties of MMH and RFNA gels

The high shear rate capillary rheometer was able to replicate shear rates conditions in jets in the injector orifice which were about 10^6 1/s. The viscometer was rated for remote controlled operation at up to 3000 psi.

Details of the main components of the capillary viscometers are illustrated in Figure 2-13 where the capillary assembly, the viscometer cabinet and the loading tube are shown. The dimensions of the capillary and the design (left) of the holding driving system (right) are shown in Figure 2-14. The capillary diameter is a critical design factor and it has a direct effect on the viscosity measurements. Thus, special care was used in the fabrication of the capillary where a minimum tolerance was established. The design provides the use of multiple interchangeable capillaries of different diameters and lengths which have a great influence on the applied shear rates. The

linear encoder served to monitor the movement of the piston that was used to estimate the shear rate applied during the test.
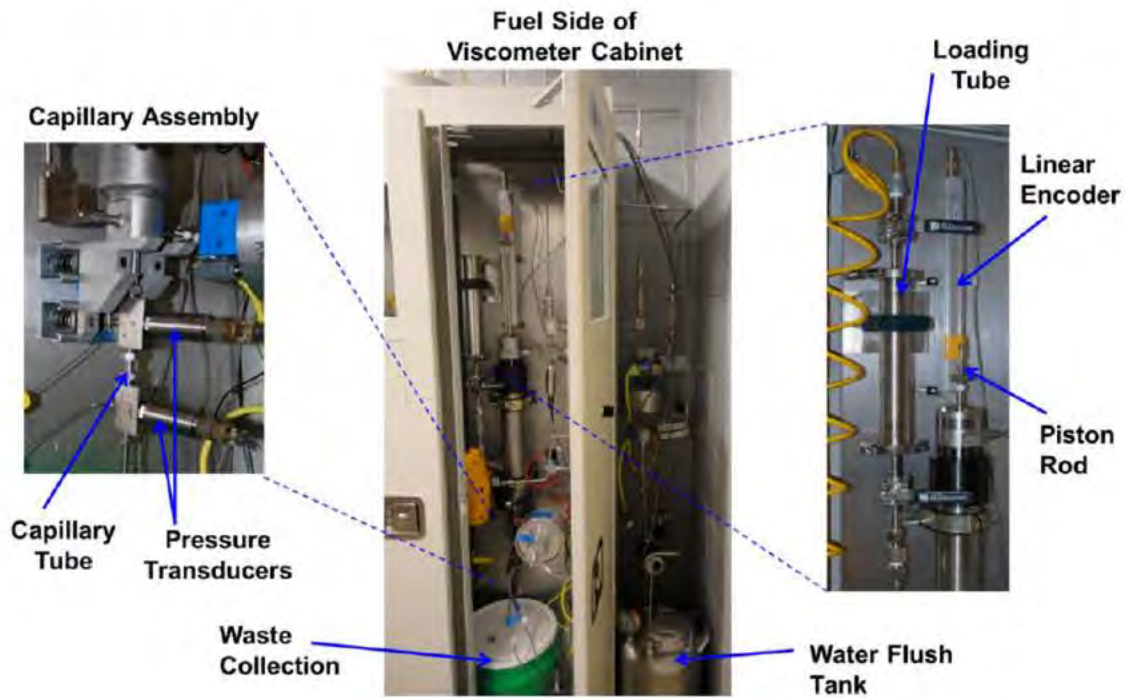

Figure 2-13. Main components of the capillary viscometer built in the project
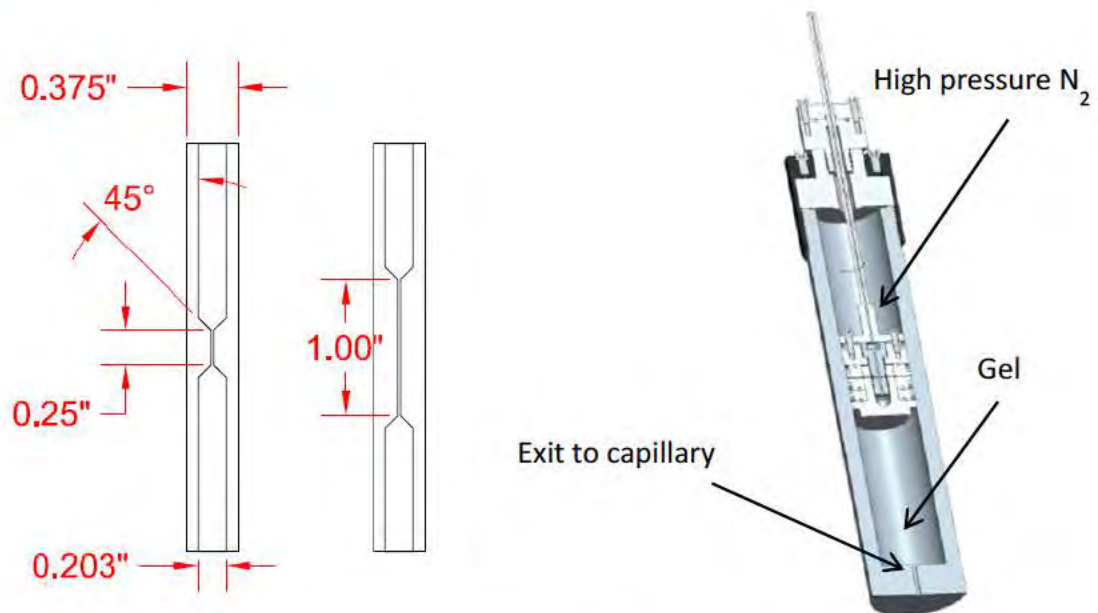

Figure 2-14. Capillary design dimensions (left) and sample driving system (right)

Further details of the system including diagram and operational procedures can be found in 2013 MURI Final meeting of November 2013 held in Pennsylvania State University and the thesis of C. Fineman. Calculations details for capillary viscometers can be found in standard text on Rheology; in particular the reference Morrison (2001) was used to estimate shear stress from measured pressure losses and shear rate from volumetric flow rates[13]. The later determined from the linear encoder data.

Calibration results including correction for entrance and exit effects (Bagley corrections) and increase in the temperature of the oil due to shearing action, which was of approximately $5^{o}C$, is illustrated in Figure 2-15 including temperature gradient along the entrance, length and exit of the capillary.
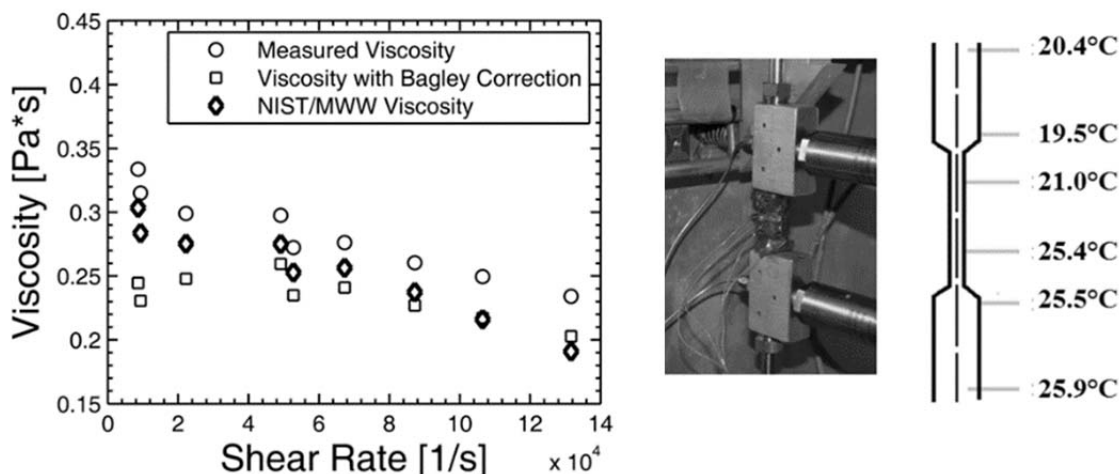

Figure 2-15. Measured viscosities of a calibrating oil (left) and temperature profile in the capillary and vicinity of the capillary (right)

Results using this high shear viscometer showed that the viscosity of polymeric gels at shear rates of about 10^6 1/s were in the order of 200 cP, i.e. much higher that the viscosity of the solvent (water in this case which is 1cP) as it had been assumed in previous research. At those high shear rates these gels were not stable and water (solvent) separated from the polymer network. Since HPC is a polymeric gel that does not break into a spray no further studies were completed. Tests on simulants prepared with JP-8 and 7% silica (Aerosil 380) showed the typically shear thinning and thixotropy observed in previous tests. Two different types of instruments: a rotational viscometer using cone and plate geometry (StressTech) for low to intermediate shear rates and the built high shear capillary viscometer, were used in the test. Results are shown in Figure 2-16, whereas Figure 2-17 shows results using the commercial capillary viscometer in addition to the rotational and high shear viscometers testing a gel formed by the fuel RP-1 and 6% silica (Aerosil R074). As before all these tests show that assuming the viscosity of the solvent as the plateau viscosity at high shear rates in inappropriate. Other results are reported in presentation given during the final review meeting held in November 2013.
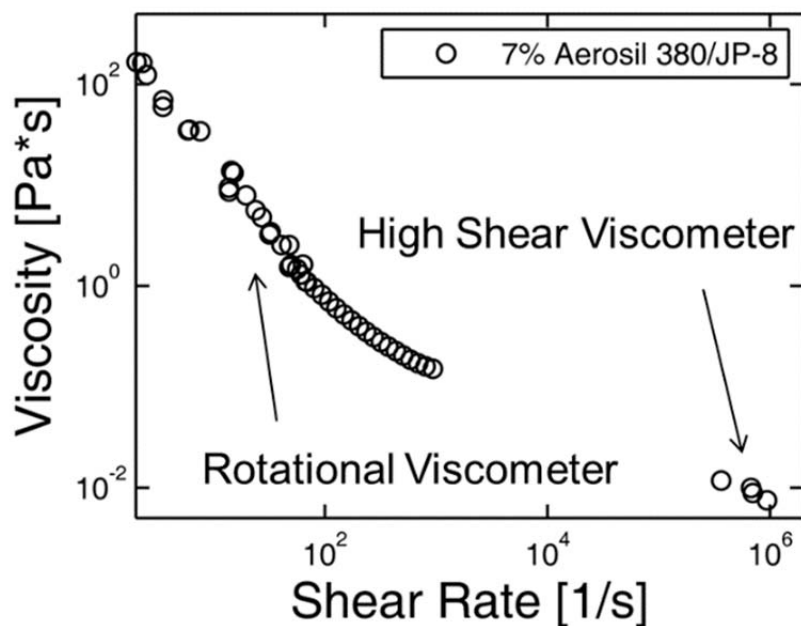
Figure 2-16. Viscosity of a particle gel prepared with 7% silica (Aerosil 380) and the fuel JP-8
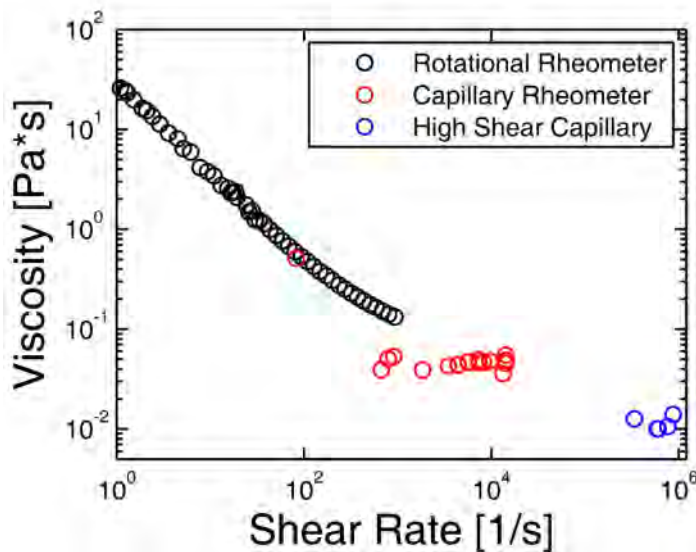
Figure 2-17. Viscosity of a particle gel prepared with 6% silica (Aerosil R974) and the fuel RP-1

The viscosity of the gels at the high shear rates conditions existing during atomization and injection is of great relevance to the flow of these gels from an experimental and simulation standpoint. Thus, the assumption previously used in past research considering that the high shear viscosity plateau of the gel is approximately that of the solvent has a great relevance in the study of these systems, especially when this research has clearly shown that is not appropriate. For example viscosities of MMH and RP1-1 fuels gelled with 6% silica (Aerosil R974) are illustrated in Figure 2-18. Of particular interest must be noted that the viscosity of the MMH gels measured

at 6×10^5 1/s and room temperature was 0.008 Pa.s (8cP), whereas the viscosity of pure liquid MMH at the same temperature was Newtonian and with a value of 0.00086 Pa.s (0.86cP). There is factor of 10 between the previously assumed values of viscosity at high shear rates and the real ones, which leads to different flow regimes. Calculations based on typical flow conditions are given in Table 2-2. Results show that the rheological behavior of at high shear rates is approximately Newtonian which corresponds to the parameter η_∞ is the Carreau Yasuda model (see Equation 2.2). As this model is a large use for flow simulation the measured value rather than the wrongly approximated viscosity of the solvent should be used.
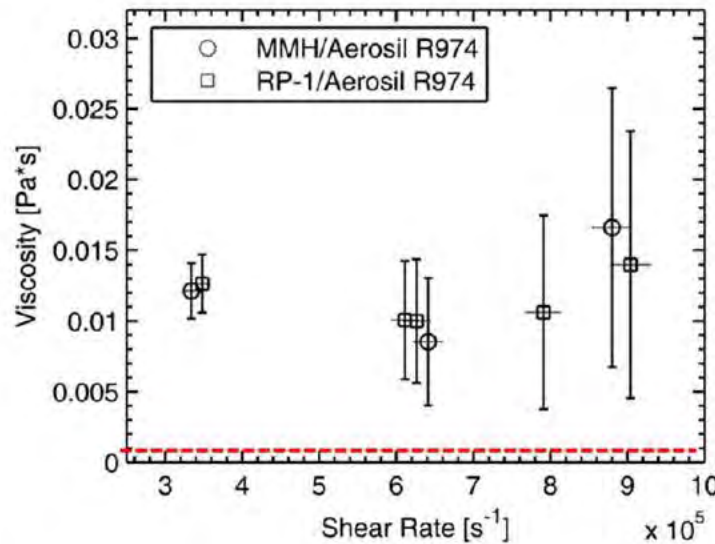
Figure 2-18. Viscosities of gelled fuels measured at very high shear rates in the designed and built high shear capillary viscometer. Red line indicates the previously assumed viscosity.

Fuel Orifice Diameter = 0.025"		
V_{inj} (ft/s)	Shear Rate (1/s)	Gel Reynolds Numbers
50	192,000	554
100	384,000	1108
150	576,000	1662

Table 2-2. Recalculated Reynolds numbers for flow conditions in a typical fuel orifice using the measured gel viscosities at the relevant shear rates

Theoretical Simulations
Several simulations models were used to describe not only the formation of particle gels but also to predict their rheological properties. Specifically the following work was performed in this area
1. Brownian Dynamics study of gel-forming colloidal particles[14]
2. Interplay between potential range and viscoelastic properties of colloidad gels[15]
3. Association of polymers by physical interactions – Rheological characterization (ICEF11, Greece 2011, Best student paper).

Conclusions from the theoretical simulations were:
1. Colloidal gels were able to be simulated by Brownian Dynamics simulations using a shifted Lenard Jones potential
2. Rheological properties for different concentrations followed the same experimental trend
3. There is a relation between potential range and viscoelastic properties of colloidal gels
4. Molecular Dynamics simulations were used to simulate polymeric systems (later described that were not appropriate for use as hypergologic gels)
5. Flexibility of polymeric chains seems to affect the viscoelastic properties of the resulting network. Similar trends with experimental data

3.0 Internal Flow and Injection of Gelled Propellants

The injection conditions (velocity profile, unsteadiness) provide the initial condition for the evolution of the spray in the combustor and hence are of great interest in enhancing understanding of the downstream events. Substantial efforts (experimental and computational) have been made to assess and characterize injection behavior of all major types of rocket injectors over the past 5-6 decades, but nearly all these investigations have been carried out with liquid propellants. While there is a wealth of literature on the flow of non-Newtonian fluids in internal flow passages, these works typically are motivated by chemical and agricultural engineering applications where flow velocities are much lower than in the rocket injection application. For these reasons, there is surprisingly little literature to draw from regarding the detailed processes governing injection. Two notable exceptions include recent work at Technion[16,17] and at DLR[18,19] that are motivated primarily toward ramjet-powered vehicles with gelled fuels.

Flow features inside an injection passage with arbitrary inflow conditions are highlighted in Fig. 3-1. The hydrodynamic instability of the vena-contracta region formed on the windward side of the orifice lip leads to mass flow pulsations at high Reynolds number injection conditions. The main technical achievement in this work has been to develop an unsteady rheological model that can be coupled to a modern CFD solver in order to simulate dynamic injection events.
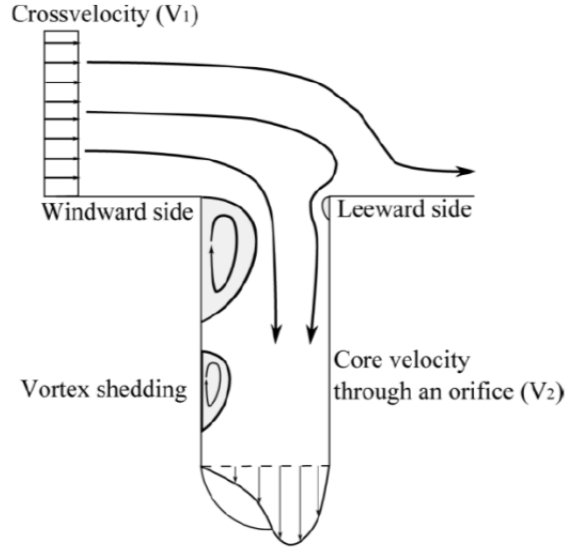
Figure 3-1: Schematic of Injector Internal Flow field under Arbitrary Injection Conditions

Our work began using a standard power law treatment typically employed in the non-Newtonian flow literature. Shear-thinning is a desirable characteristic for rocket applications as the viscosity of the mixture η, decreases with increased shearing rate, $\dot{\gamma}$ thereby permitting better atomization and mixing in the spray. The Carreau-Yasuda model was incorporated into axisymmetric and fully 3-D CFD tools:

$$\frac{\eta(\dot{\gamma}) - \eta_\infty}{\eta_0 - \eta_\infty} = \left[1 + (\dot{\gamma}\lambda)^a\right]^{\frac{n-1}{a}} \tag{3.1}$$

and parametric studies were conducted for a variety of injection conditions, fluid rheologies, and injector geometries[20,21,22,23,24,25]. A typical result is shown in Fig. 3-2. As the fluid relaxes into a plug-type flow in the central part of the channel, the viscosity recovers to higher values per the power law behavior.

This behavior leads to viscous pulsations that emanate from the injector orifice – the physical presence of these structures is not yet known as it is very challenging to get time-dependent massflow/viscosity measurements for fluid exiting an orifice at high speeds. Typical unsteady character of massflow is depicted in Fig. 3-3. The pulsation magnitude and frequency has been characterized for different flow conditions, fluid rheologies, and orifice geometries in order to provide users with a database for future injector design.
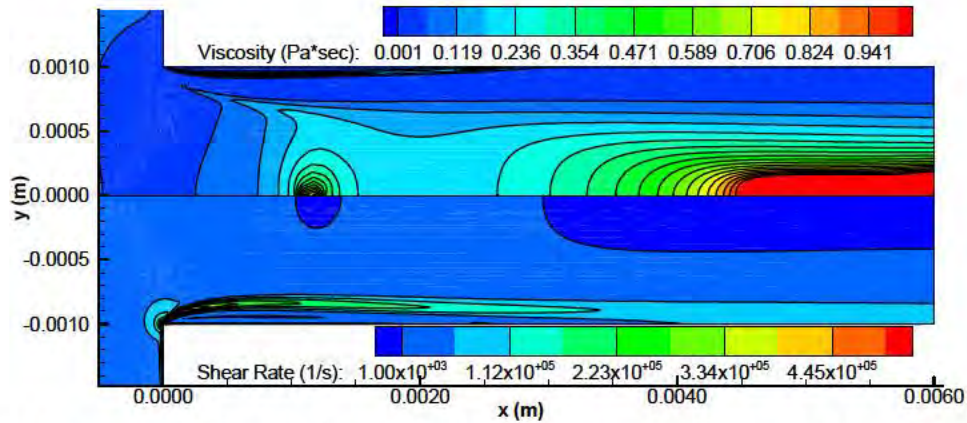
Figure 3-2: Viscosity and Shear Rate Distribution within Orifice Passage – Shear Thinning Model Results
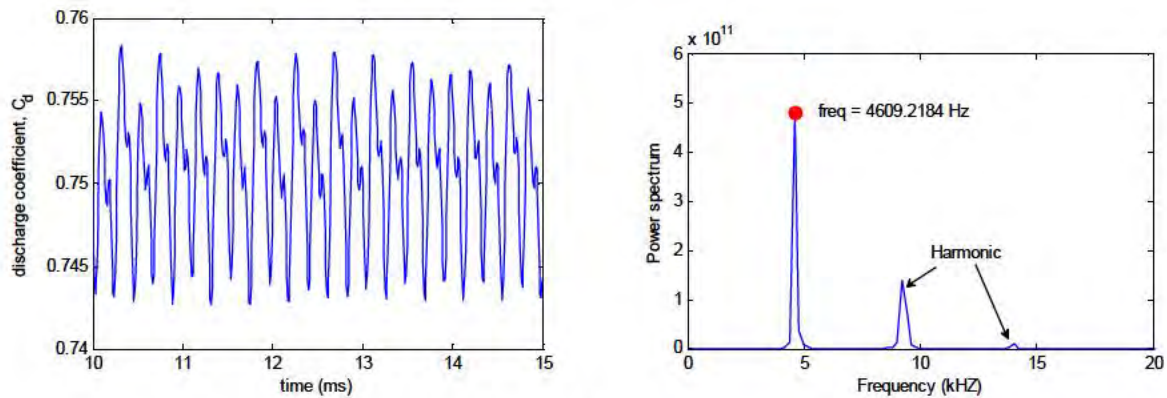
Figure 3-3: Typical orifice massflow (left) and frequency content (right) under high-speed injection conditions. Massflow pulsations of a few percent can be realized – these pulsations convect downstream into the impingement region and can affect subsequent spray development.

Larger engines using multi-element injectors can be fed assymetrically due to crossflow inside the manifold. Complex structures (horseshoe vortices) are shed from the inlet lip under high crossflow conditions. Figure 3-4 shows a typical result. Massflow pulsations (amplitude and frequency) were also characterized for these complex 3-D flows using the shear thinning rheology model.
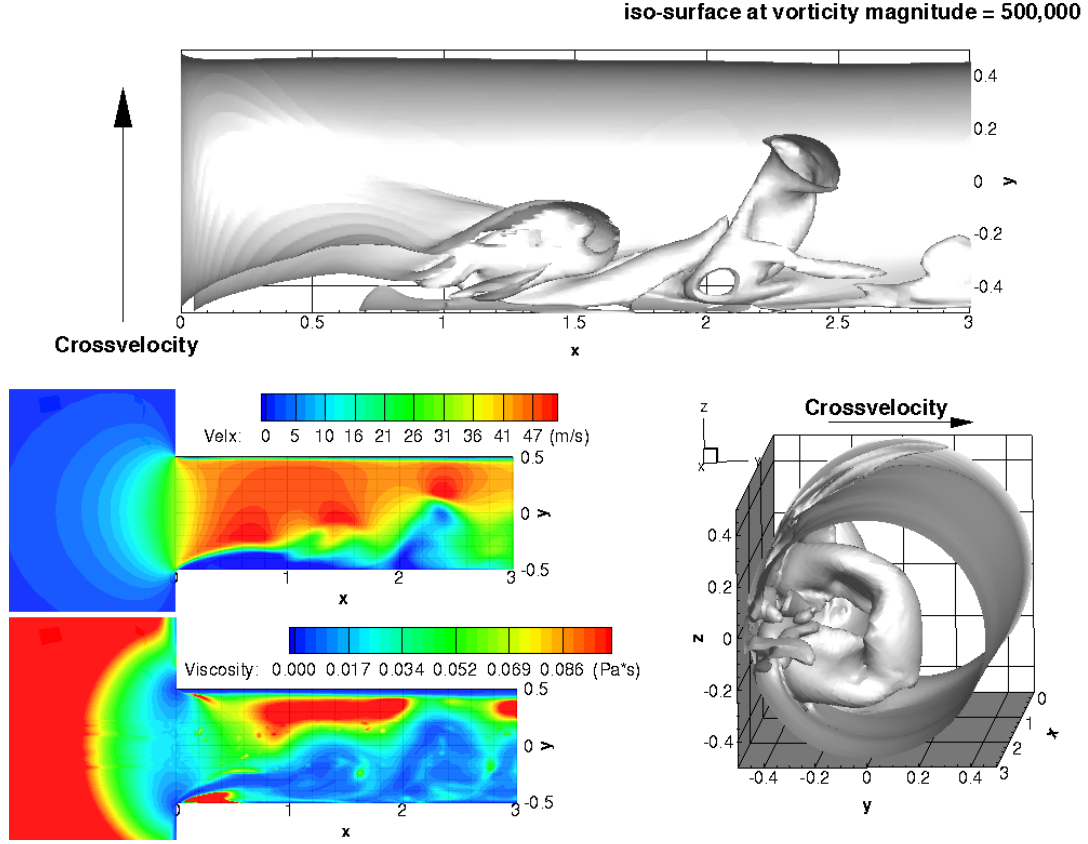
Figure 3-4: Typical structures formed in orifice fed by a strong crossflow.

The rheological model shown in Equation 3.1 was viewed to be sufficient to describe polymeric-based gels because these fluids tend to recover gel structure fairly quickly upon extrusion through an orifice passage. However, particulate gels are known to break down substantially upon shear and do not recover the original gel structure. This effect, referred to as thixotropy, leads to a hysteresis in the rheological behavior as noted in Fig. 3-5. Since the gels that were producing good combustion performance were all particulate based, we turned our attention to the development of a rheological model that could address thixotropic effects. The resulting two-parameter model is[26]

$$\frac{\partial \eta}{\partial t} + \mathbf{u} \cdot \nabla \eta = \alpha \min\left(\eta_{e,1} - \eta, 0\right) + \beta \max\left(\eta_{e,2} - \eta, 0\right) \tag{3.2}$$

where α and β are empirical constants controlling the rate of shear thinning during initial shear application and shear thickening occurring when shear is reduced. Empirical data were used to derive appropriate α and β values for particulate gels of interest. To our knowledge, this is the most advanced rheological treatment for polymeric gels as applied to high shear conditions such as those in the rocket injector. The results showed excellent agreement with measured orifice discharge characteristics as shown in Fig. 3-6.
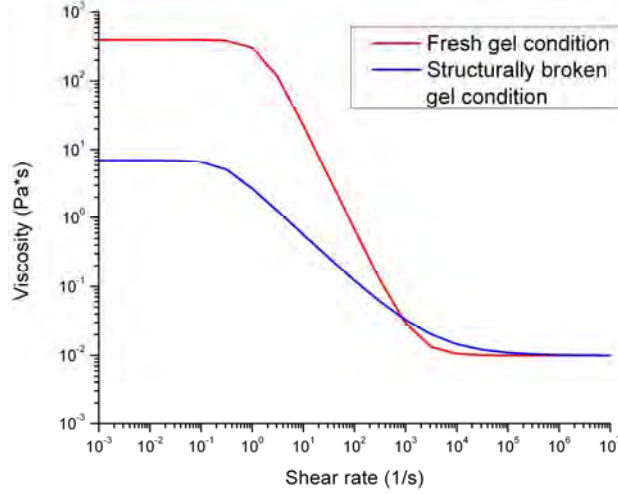
Figure 3-5: Thixotropic behavior of particulate-based gel showing loss of viscosity upon application of shear.
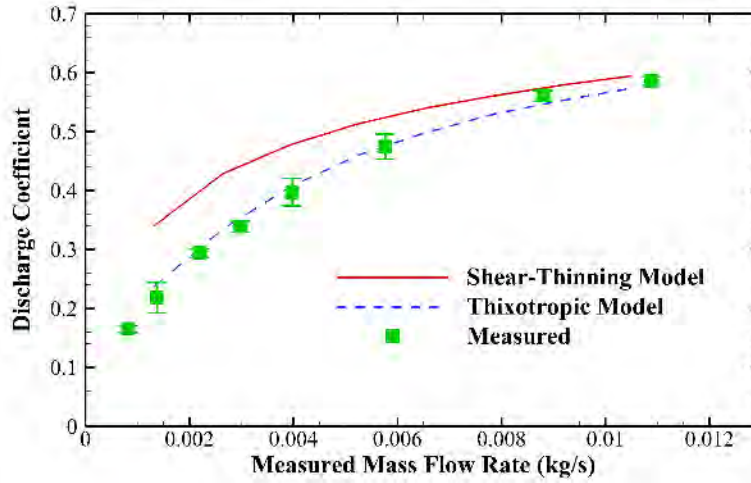
Figure 3-6: Comparison of thixotropic model with measured massflow data showing excellent agreement.

4.0 Jet Impingement and Primary Atomization

4.1 Modeling Efforts

We developed high-fidelity direct numerical simulations to seek a mechanistic understanding of the influence of gel rheology on the dynamics of jet impingement and primary atomization. While the challenge of simulating the transient motion of the deforming interface during jet impingement has led most previous work to use simplified models, in this research we used direct numerical simulation, where the conservation equations governing the flow, capillary forces, and interfacial motion were fully resolved without additional modeling. The numerical scheme employs the finite element method for spatial discretization, along with an arbitrary Lagrangian-Eulerian method to parameterize the deforming interface and implicit time integration. It also incorporates a Carreau-Yasuda constitutive equation to account for the shear-

thinning gel rheology (see Section 2), and a convection-diffusion equation to account for interfacial transport of surface active species. Validation and implementation details can be found elsewhere[76,78,80,82,83]. Parametric studies were conducted for a variety of operating conditions and fluid rheologies.

A typical result illustrating the influence of gel rheology on jet impingement at moderated jet velocities is shown in Figure 4-1. As the fluid is exposed to strong shear stresses during the transition from axial to radial flow in the impact region, the local viscosity rapidly decreases due to the shear-thinning behavior. We have found that this behavior leads to important differences on both the thickness of the radially expanding sheet and the size of the bounding toroidal rim[82,83]. We characterized these differences parametrically because of their critical influence on the stability of the sheet and the size of the drops resulting from the Rayleigh fragmentation of the bounding rim.
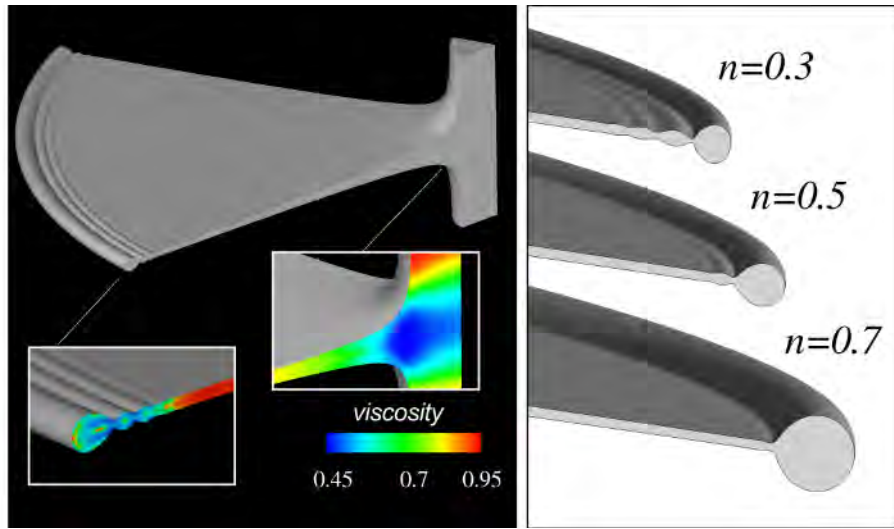

Figure 4-1: (Left) Typical viscosity distribution during the early stages of jet impingement. The viscosity decreases in both the impact region and the neck of the bounding rim due to the shear-thinning behavior. The local viscosity is measured in units of the zero-shear viscosity of a Carreau-Yasuda model. (Right) As the strength of the gel increases (from top to bottom), the size of the bounding rim grows, and the capillary waves disappear through the action of viscosity.

As the velocity of the impinging jets increases or, more precisely, when the Weber number of the jets is above a critical value, incipient impact waves can be observed on the interface of the expanding liquid sheets. Understanding the origin and factors that influence the formation of impact waves is important because of the critical role they play on the initiation and growth mechanisms of downstream interfacial instabilities. Our simulations suggest that the origin of the impact waves can be traced to hydrodynamic instabilities in the vicinity of the stagnation point. As illustrated in Figure 4-2, hydrodynamic wave structures convect downstream from the impact region and approach the free interface, initiating the observed interfacial waves a few jet radii away from the impact point. Simulations are challenging largely because of the highly nonlinear way in which the hydrodynamic instability interact with the free interface. Nevertheless, the direct numerical simulations enabled the study of the factors influencing the impact waves with focus on the fluid rheology and the unsteadiness originated in the injection process[83]. Indeed, as

described in Section 3.0, unsteadiness in the injection process leads to massflow pulsations that emanate from the injector orifice. Results from this study show that, as the massflow flow pulsations convect from the injector into the impingement region, they have a critical effect on the subsequent development of the impact waves. The effect of pulsation magnitude and frequency on the impact waves has been characterized in this study through simulations for different flow conditions and fluid rheologies, as exemplified in Figure 4-3.
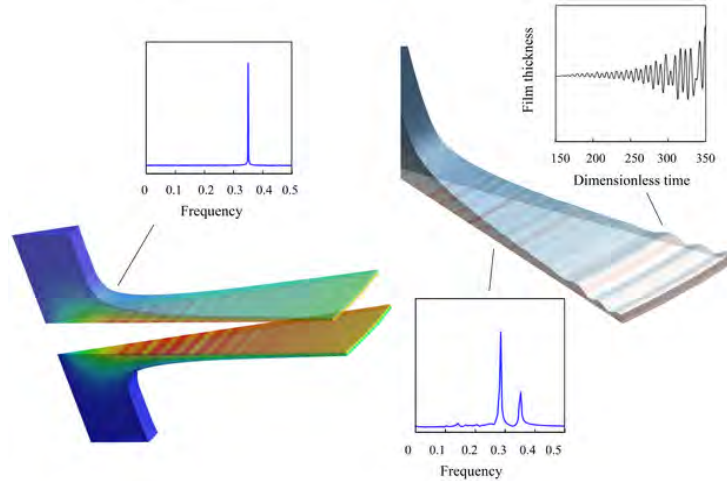

Figure 4-2: (<u>Left</u>) Cross-sectional velocity field illustrates wave structures of hydrodynamic origin that form in the impact plane during jet impingement. (<u>Right</u>) These structures convect downstream initiating instabilities which are observed at the interface as incipient impact waves.
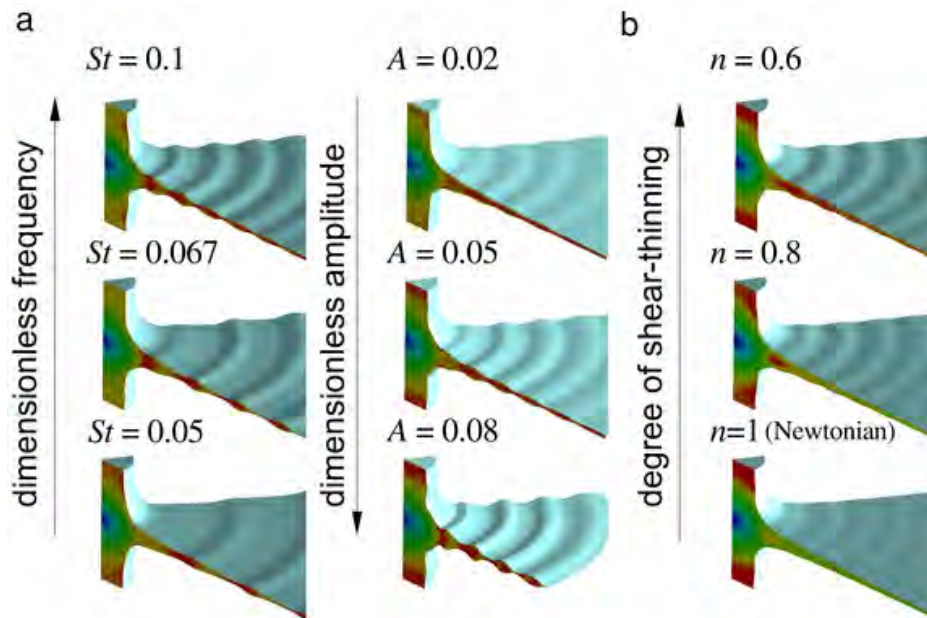

Figure 4-3: Influence of massflow pulsations emanating from the injector orifice on the initiation of impact waves. (a) Effect of pulsation magnitude and frequency on the resulting impact waves. (b) Expanding liquid sheets formed by the impingement of gelled propellants are less stable than their Newtonian counterpart due to the shear-thinning behavior.

The dynamics of the gelled filaments originated by the fragmentation of the expanding sheet during primary atomization (see Section 1.2) is still poorly understood not only because their complex rheological behavior but also because they contain surface active species, such as gelants, adsorbed onto the interface that locally change the dynamic surface tension. Therefore, to gain insight into the physical mechanism involved in the breakup of gelled filaments, we added a convection-diffusion equation to our free-surface algorithm to track the concentration of the surface active species (surfactants). These numerical studies are challenging because, in addition to the flow field and location of the free interface, the surface tension must be calculated as a function of space and time to determine the normal (capillary) and tangential (Marangoni) stresses at the interface. A typical result is shown in Figure 4-4. We have found that shear-thinning effects favor the formation of satellite drops by reducing the viscous resistance to the tangential Marangoni stresses induced by the presence of surfactants[76,77,78,79,86,88]. Similarly, we found that the coalescence dynamics of the drops resulting from the fragmentation of the gelled filaments is strongly affected by the bulk and interfacial rheology[80,81,83,84,85,87,89,90]. For example, results show that shear-thinning behavior accelerates the rate of drop coalescence by reducing the viscous resistance to the grow of the meniscus bridge formed between the droplets, as illustrated in Figure 4-5.
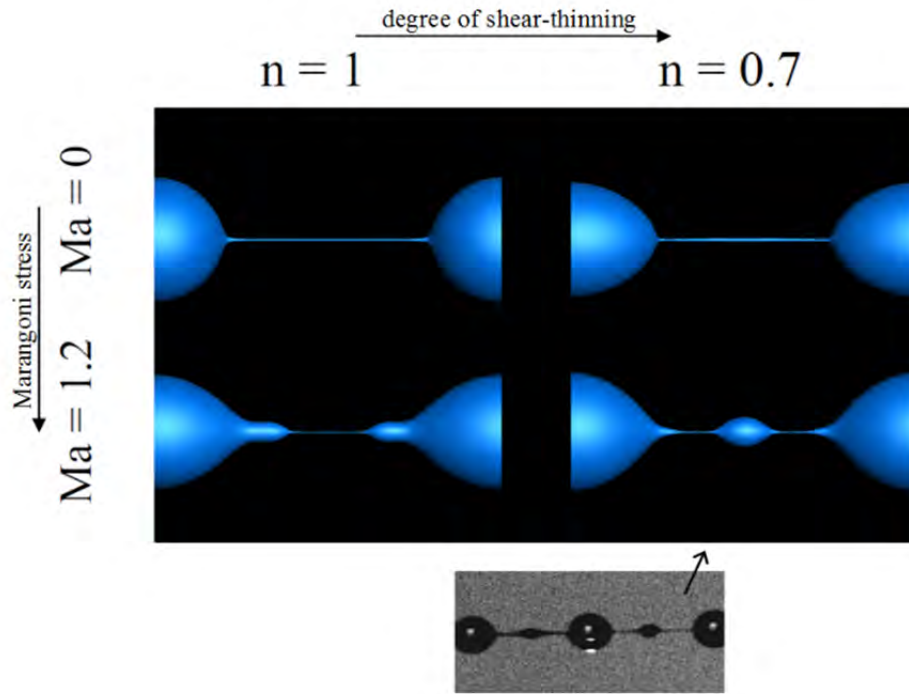
Figure 4-4: Breakup of inelastic gel filaments. Interactions between shear-thinning rheology and interfacial Marangoni stresses favors the formation of undesired satellite droplets (bottom right) during primary atomization. The photograph shows corresponding high-speed visualization experiments on surfactant laden, shear-thinning filaments by A. Dechelette and P. Sojka, Purdue University, illustrating the formation of the satellite drops.
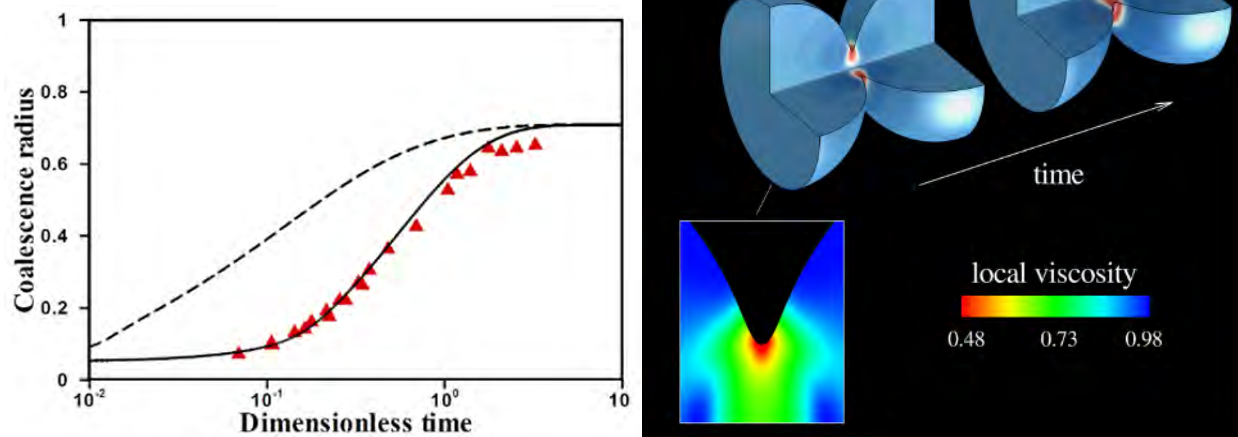
Figure 4-5: Drop coalescence. (<u>Left</u>) Radius of the fusion neck formed between Newtonian (solid line) and Carreau-Yasuda (dashed line) liquid drops. The red symbols correspond to high-speed visualization experiments by Yao et al.[27] for Newtonian silicon drops. (<u>Right</u>) Cross-section local viscosity field (inset) shows that shear-thinning behavior accelerates the rate of coalescence by reducing the local viscosity near the joining meniscus.

## 4.2 Experimental Measurements in the Impingement Zone

The merging if impinging liquid jets creates high shear rates and significant local deformation that can result in rapid mixing. The rate in which the two fluids mix dictates subsequent gas formation and chemical reactions that take place in the case of hypergolic injection. Unfortunately, the high index of refraction gradients and complex 3-D geometry make it difficult to probe the region in which the two fluids merge. The important science accomplishments in this task include:

- Devising methods to probe the optically complex impingement zone and extract important features that control the mixing process
- Measuring the time scale of the mixing process at the impingement zone
- Measuring the spatial scale of the mixing process at the impingement zone
- Determining the relevance of 3-D effects in the mixing process to guide modelling efforts
- Determining the effects of material properties on the spray structure
- Quantifying the magnitude and frequency of instability waves, which later form ligaments and droplets downstream

The diagnostics effort included several approaches, including ballistic imaging, X-ray radiography, X-ray fluorescence, and digital fringe projection (DFP) surface imaging. While ballistic imaging was initially attempted early in the research effort to probe the optical dense impingement zone, it was found that the level of atomization was not sufficient for this approach to have significant advantages over conventional techniques such as shadowgraphy, laser-induced fluorescence, or phase-Doppler anemometry. However, the latter techniques provide key information downstream of the impingement point, and other approaches were needed to resolve

the liquid mass distribution within the impingement zone and to quantify the thickness of instability waves. Hence, in the current work, the focus shifted to extracting information about the internal mass distribution in the impingement zone using synchrotron-based X-ray radiography/fluorescence and measuring near-field surface instability waves using flash X-ray radiography and DFP.

Figure 4-6 shows the nozzle geometry, designed by the Purdue team for use by researchers at ISU. It utilizes ~0.5 mm diameter orifices and a 60 degree included angle. The coordinate system used this discussion is also shown in Fig. 4.6, with the x-z plane encompassing the plane of the injected fluids and the y-z plane encompassing the plane if the liquid sheet that is formed by the impinging jets. The region of interest in this discussion includes the spray structure that forms from 0 mm to 10 mm from the nozzle, with the impingement taking place within 3 mm of the jet exit orifices and the initial sheet formation taking place within 10 mm. Note that the individual jets are visible in the near stream of the shadowgraph images, including instabilities in the jet column. However, there is very little that can be discerned about the mixing process when the jets merge. Moreover, 2-D axisymmetric model described above provides important understanding of sheet instability, but does not allow for the liquids to pass through each other during the mixing process since this would be a three dimensional effect.

(a)   (b)
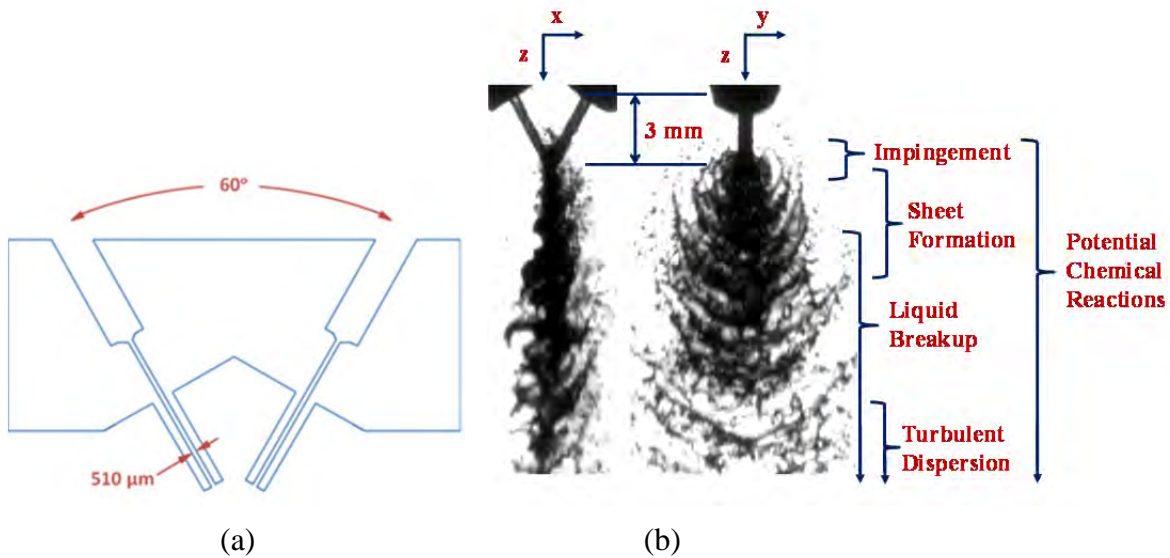
Figure 4-6: (a) Nozzle geometry and (b) spray structure created in the plane of the jets (x-z) and in the orthogonal plane (y-z).

To gain knowledge about the 3-D mixing process, we investigated X-ray radiography and fluorescence as means to interrogate near-field mixing in the optically complex regions of the spray, as shown in Fig. 4-7. Radiography utilizes the attenuation through the spray to mark an equivalent path length of liquid (EPL) using a known (calibrated) attenuation coefficient. This gives total mass but does not distinguish the mass of each liquid because the attenuation coefficient is nearly same for both liquids. To quantify mixing, each jet is doped with minute amounts of two different fluorescent tracers, and the fluorescence from each can be recorded separately to determine the mass of each liquid along the same path and thus mixing.
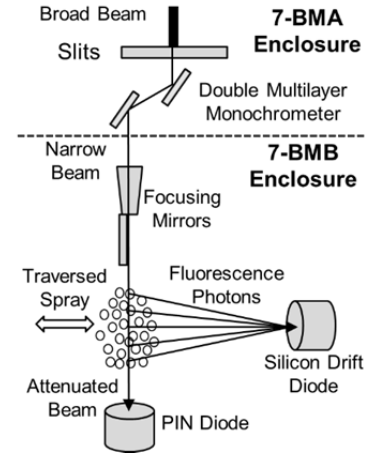
(a)   (b)

Figure 4-7: (a) Synchrotron source at the Advanced Photon Source at Argonne National Laboratory and (b) set-up for X-ray radiography and fluorescence.

In an advanced version of this approach, we seeded each jet with two different tracers to account for the reabsorption of the X-ray fluorescence as it travels from the point of signal generation to the X-ray silicon drift diode (see Fig. 4-7). Since each of the two tracers has a different attenuation coefficient through the spray, it is possible to use their relative signals to correct for this attenuation so that the final signal is not dependent upon the amount of liquid surrounding the measurement location. The absorption spectrum showing that the four fluorescence tracers can be distinguished is presented in Fig. 4-8(a). Figure 4.8(b) shows a sample X-ray fluorescence spectrum from two tracers marking the individual jets during impingement ($z = 3$ mm downstream of the nozzle). It is evident that the two liquids overlap in the x-axis, and yet it is possible to measure the fluid from each stream individually.
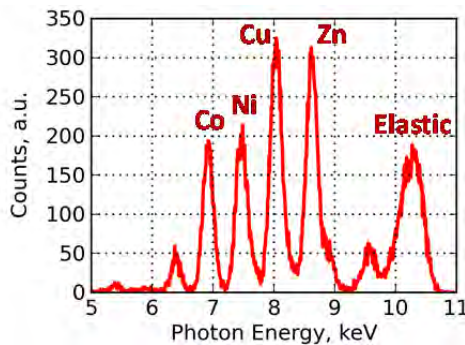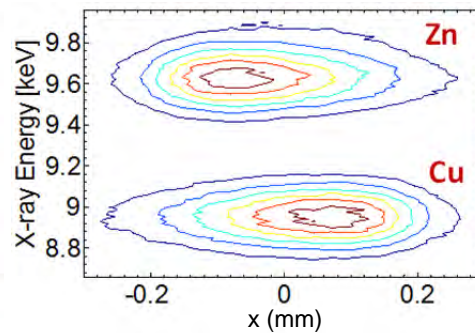

(a)   (b)

Figure 4-8: (a) X-ray spectrum of metal tracers seeded into liquid jets and (b) sample X-ray spectrum detected in individual jets during impingement (3 mm downstream of nozzle).

A complete history of the mass profiles from each 0.5 mm diameter jet is illustrated in Fig. 4-9, starting with the individual jet profiles prior to merging at $z = 1$ mm downstream. As the fluids begin to merge at $z = 2$ mm downstream, there is still very little deformation in the jet profiles. At $z = 3$ mm, however, corresponding to the case shown in Fig. 4-8(b), the liquid jets are significantly compressed to less than half of their original diameter, and there appears to be

significant overlap in their spatial distributions. The compression is expected from the increased strain rate during the merging process, but the overlap is not expected from 2-D simulations. A potential mechanism for this overlap is known as transmitting mixing, as illustrated in Fig. 4-10, where three possible mixing mechanisms are compared. Since molecular diffusion is a rather slow process, then transmitting mixing is the most likely mechanism for mixing during the merging process, which can be followed by atomization at higher Reynolds numbers.

(a)   (b)
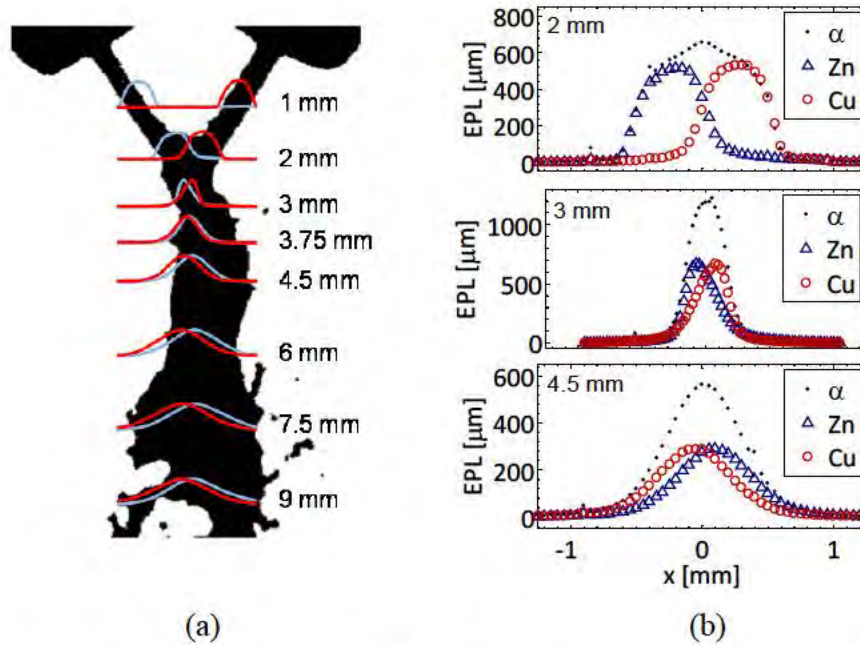
Figure 4-9: (a) Overlay of visible image and X-ray fluorescence spatial profiles marking the fluids originating from the left and right jets at various locations downstream of the jet exit and (b) sample quantitative plots of equivalent path length (EPL) of each fluid (Zn from left and Cu from right), as well as the two fluids combined (α) at three locations downstream of the jet exit.

(a)   (b)   (c)
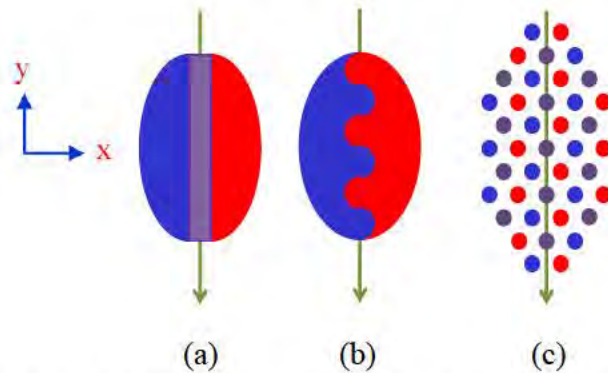
Figure 4-10: Schematic top view of different possible mixing processes as two jets meet, compress, and begin to mix, including the (a) diffusive, (b) transmittive, and (c) atomizing regimes. Coordinate system is consistent with Fig. 4-6.

As the jets in Fig. 4-9 continue to move downstream from z = 3 mm to 6 mm, the jets broaden and it is apparent that the liquids actually move past each other. From z = 6 mm to 9 mm, the jets seem to halt their movement but continue to broaden due to turbulent dispersion. Quantitative

line plots for model validation are shown in Fig. 4-9(b), where it is possible to observe changes in the location, shape, and magnitude of the liquid profiles at various locations downstream. For example, the overlap and complete deceleration of the fluids takes place over a vertical extent of ~ 2–3.75 mm downstream of the jet exit. Given the jet exit velocity of 18.3 m/s, the timescale to reach full overlap of the two liquids (~100 microseconds) is too short for diffusive mixing. Hence, one can presume that the deceleration and overlap in liquid distribution is taking place via transmitive mixing or atomization. Also, based on this time scale, one cannot assume that full repulsion of the liquid phase will occur through rapid gas formation prior to the onset of significant mixing processes, and fluid-chemistry coupling may be important.

Figure 4-11 shows the near-field mixing process for water versus 1% and 3% HPC gels in water. As the gelled liquids begin to merge in the top row of Fig. 4-11, there is a significant increase in the equivalent liquid path length at x ~ 0 mm (centerline), leading to sheet formation in the y-direction due to increased resistance to transmitive mixing or atomization.
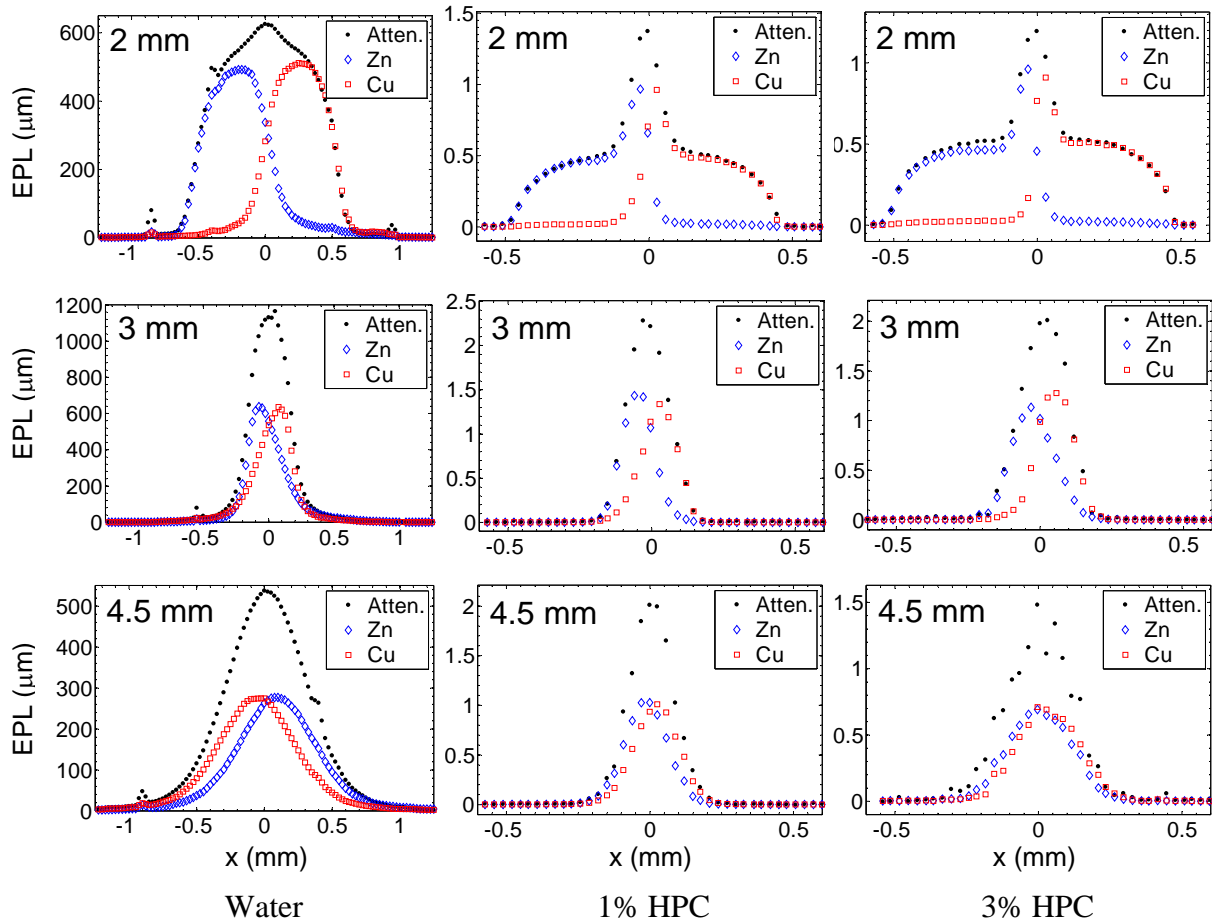
Figure 4-11: Comparison of mixing behavior for water and gels with two different concentrations of 1% and 3% HPC.

This is confirmed further downstream at z = 3 mm (middle row in Fig. 4-11), where the jets have compressed significantly for the case of gelled liquids, even more so than the case of pure water. This is likely due to the reduced instabilities for the case of gelled liquid, making the average profile appear to be thinner. When comparing the sheet thickness for the case of 1% versus 3%

HPC, it is clear that the higher viscosity of the 3% HPC case leads to a thicker sheet due to increased resistance to deformation.

Then at z = 4.5 mm (bottom row of Fig. 4-11), the profiles begin to broaden, perhaps due to the formation of sheet instabilities, which make the spray appear thicker in a time averaged sense. Despite the orders of magnitude higher viscosity for the gels, as shown in Fig. 4-12, they reach full overlap within a vertical span of ~2.5 mm from the start of interaction, compared to ~1.5 mm for water. This would occur at a time scale of about 160 microseconds or less, meaning that the surface area for hypergolic reaction can be significantly altered prior to gas formation.
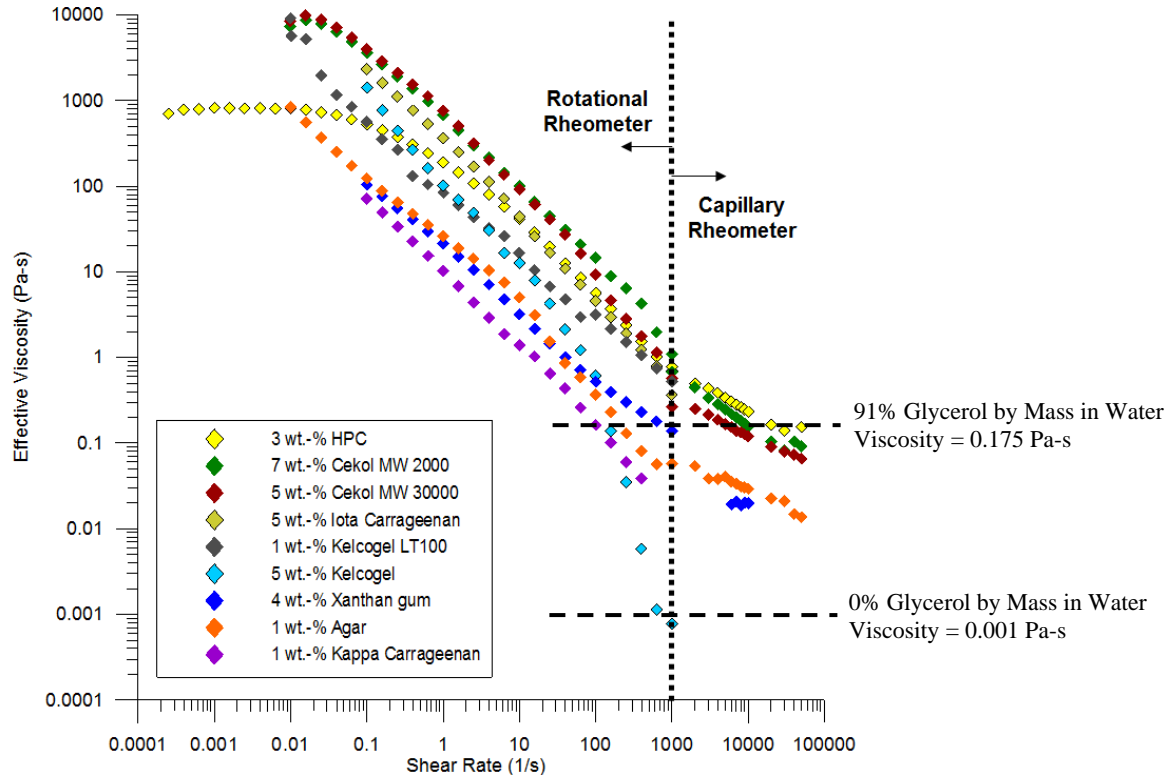
Figure 4-12: Effective viscosity of various gels, including the case of 3% HPC from the work of Mallory and Sojka, along with the theoretical viscosity of pure water and 91% glycerol by mass in water.

According to Fig. 4-12, the effective viscosity for the gels is much higher than that of water even at the highest strain rates measured. To reach a similar viscosity as the gels using a Newtonian fluid, we utilized 91% glycerol by mass in water and investigated the mass distribution for glycerol versus the HPC gels to estimate an effective local strain rate for impinging gelled liquids. Figure 4-13 reports the sheet width and equivalent path length using X-ray radiography for jet velocities of 9.1 m/s (30 ft/s) and for water, HPC gels, and 91% glycerol by mass in water. At 3 mm, the sheet profile for water is very similar to that of 4% HPC near the centerline at y = 0, likely because this is the location of highest shear. This indicates that the local shear rate and effective (lower) viscosity of the 4% HPC gel may be beyond the range available from Fig. 4-12. Further from the centerline at about y = ±0.5 mm, the sheet profile for water matches more closely to the 2% HPC, which is consistent with the shear rate decreasing further from the

centerline. Even further from the centerline at y = ±1.5 mm, the water profile broadens and slowly approaches an EPL of zero, indicating significant break-up has taken place. The gels, on the other hand, retain a sharp gradient at the edge, indicating that an intact sheet is likely present. Further downstream at 9 mm, the 3% and 4% HPC gels actually narrow in their sheet profile, likely because the strain rate decreases. In contrast, the water, 2% HPC, and 91% glycerol in water broaden significantly. As the water shows a rather gradual profile, it is likely undergoing significant break-up and atomization. However, the 2% HPC gel and the 91% glycerol in water cases have nearly identical sheet profiles. This indicates that the 2% HPC has a similar local viscosity (Viscosity = 0.175 Pa-s) as the 91% glycerol in water. Even further downstream at 15 mm, the water spreads due to continuing breakup and atomization, while the 91% glycerol in water likewise spreads into a wider liquid sheet.


(a) (b)

(c)
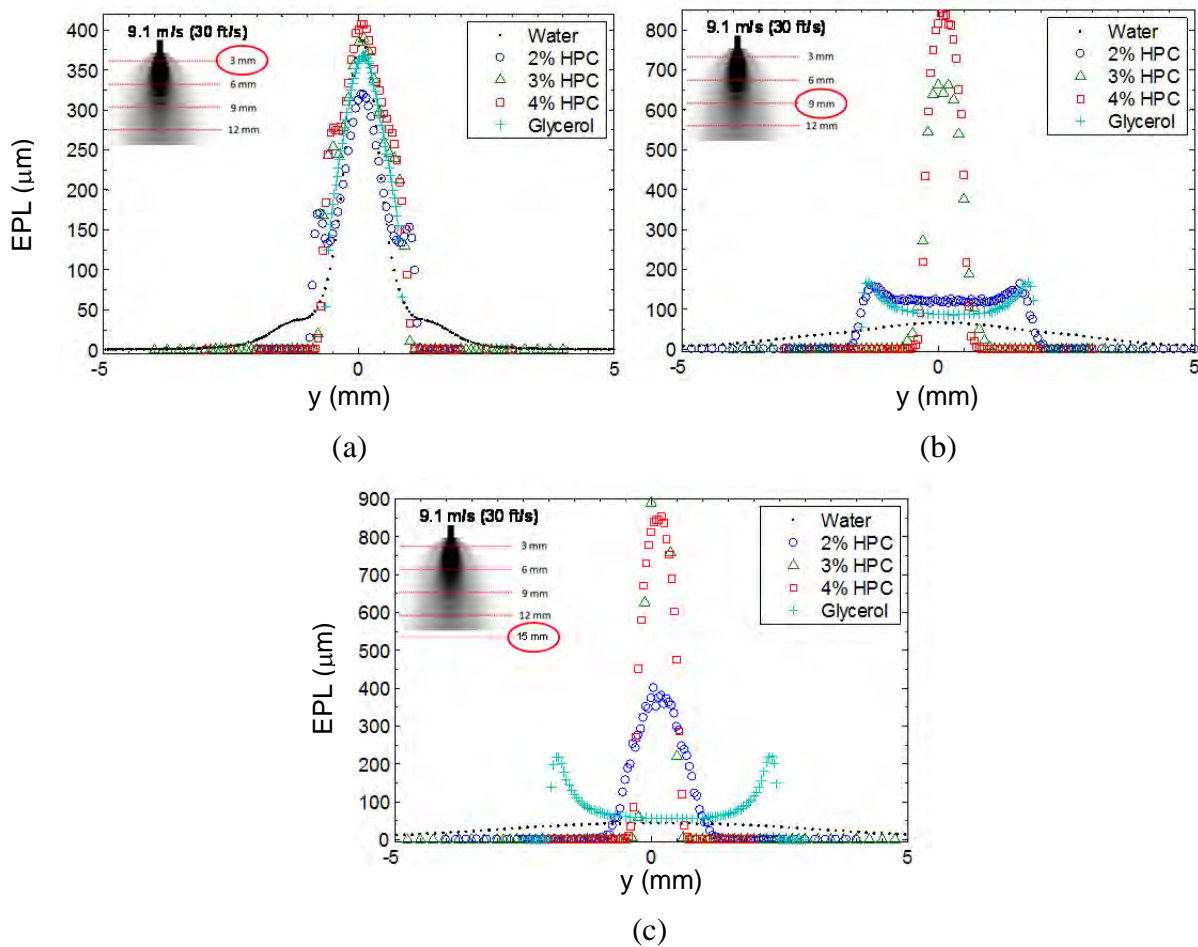
Figure 4-13: Comparison of sheet width due to spreading in the y-direction for water, HPC gels, and glycerol at 91% by mass in water at (a) 3 mm, (b) 9 mm, and (c) 15 mm downstream. The jet exit velocity is 9.1 m/s (30 ft/s) for each jet.

For both water and 91% glycerol in water, their viscosity is not a function of strain rate and so they have predictable trends as they propagate downstream. However, all HPC gelled liquids narrow at 15 mm, again likely due to decreased strain rate and higher viscosity at that location. From these data and the viscosity measurements in Fig. 4-12, it is possible to quantitatively

compare the liquid equivalent path length with great detail and accuracy during impingement and sheet formation, and hence surmise the evolution of the local strain rate and viscosity. The use of water and 91% glycerol in water enables estimation of the range of the strain rate for different locations during impingement and sheet formation.

To understand local instabilities within the sheet, it was necessary to utilize a time-resolved measurement. In this case, we utilized flash radiography and calibrated for the effects of beam hardening due to the broadband tube source. The results are shown in Fig. 4-14. The backlit images are shown just for qualitative imaging with high resolution. However, extracting quantitative information from this data is difficult. The flash X-ray images show the quantitative EPL within the sheet.

| **Backlit Imaging** | **Flash X-ray** | **Comparison with APS X-ray** |
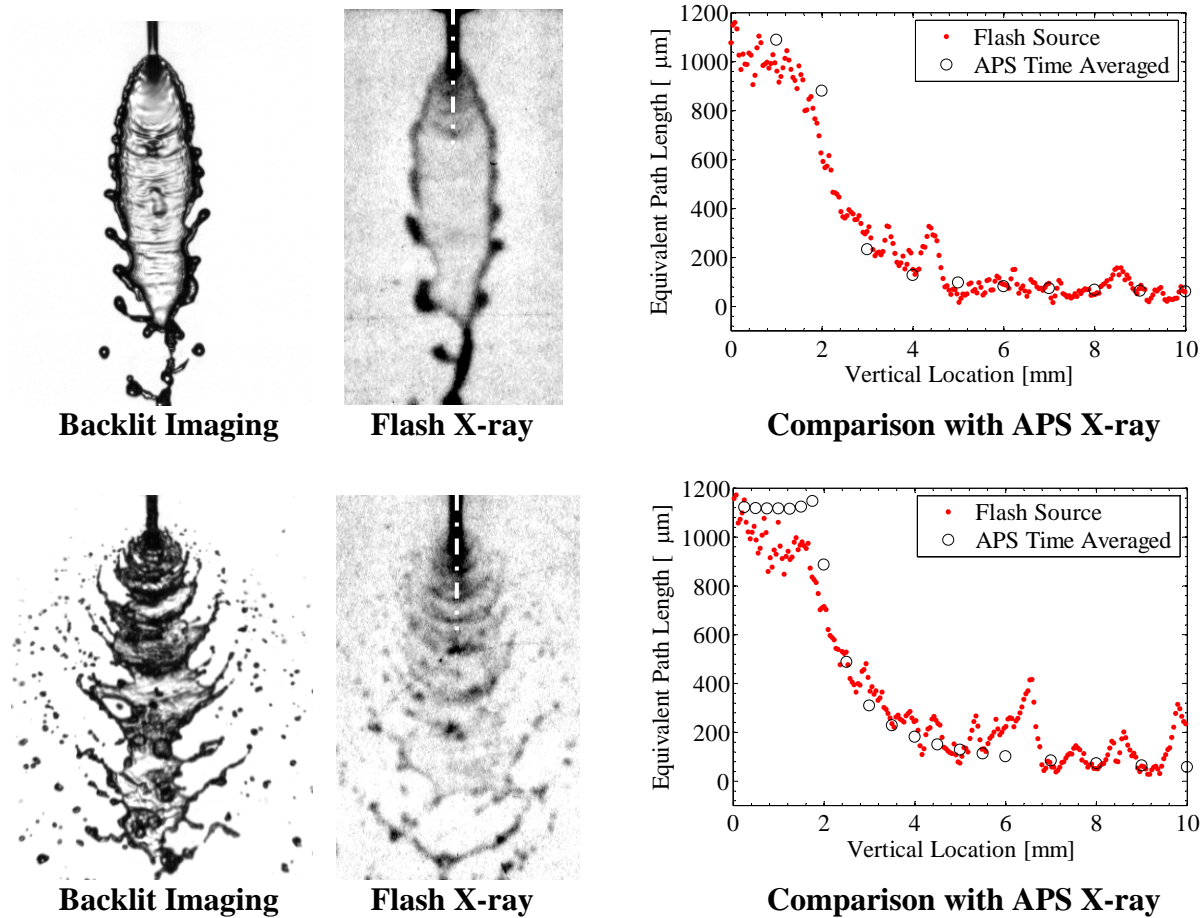
Figure 4-14: Impinging-jet sprays with jet exit velocities of 3.5 m/s (top row) and 8 m/s (bottom row). To the left are diffuse backlit images, in the middle are flash X-ray radiograms, and to the right are centerline profiles comparing flash X-ray radiograms and synchrotron X-ray radiography and showing quantitative accuracy of mass distribution.

The accuracy is confirmed via time-averaged measurements using the synchrotron sources at the APS. The decay of the EPL is accurately measurement by the flash X-ray measurements, implying that the EPL or thickness of the instability waves is also accurately captured. Note that

in the top row of Fig. 4-14 at 3.5 m/s, the high-frequency instabilities just below the impingement point are captured by the flash X-ray images, as are the lower frequency instabilities closer to 10 mm (see dash-dot lines to see vertical range plotted). The instability waves appear to have thicknesses (EPL values) of between 100 to 200 microns at this condition.

For the higher flow rate of 8 m/s in the bottom row of Fig. 4-14, there is significant breakup taking place. In this case, the decay of the EPL as a function of the downstream coordinate is similar, although more of the liquid seems to be contained within the instability waves. This is a powerful approach to measuring the magnitude and frequency of instability waves. However, there are some features at the side edges of the sheet that are visible in the backlit images and which do not appear in the X-ray images because of limited sensitivity and resolution. For example, the instability waves predicted by the numerical model and shown previously in Fig. 4-1 seem to appear near the rim of the liquid sheet in the backlit images. As such, it is noted that both techniques are useful, and the simultaneous collection of both would be ideal.

In fact, in the case of a contiguous liquid sheet, it is possible to utilize a visible imaging technique known as digital fringe projection (DFP) to obtain quantitative information about the topology of surface waves. This is a common approach for metrology and was applied here as illustrated in Fig. 4-15. The raw image of the digital fringes projected onto a liquid sheet is shown in Fig. 4-15 (left), and the processed image taking into account the deformation of the fringes is illustrated in Fig. 4-15 (right). Note that the fringes are not uniformly distributed and have a higher peak in the center of the sheet. This capability was demonstrated at detection rates of 10 kHz and higher, although studies with gelled liquids are ongoing.
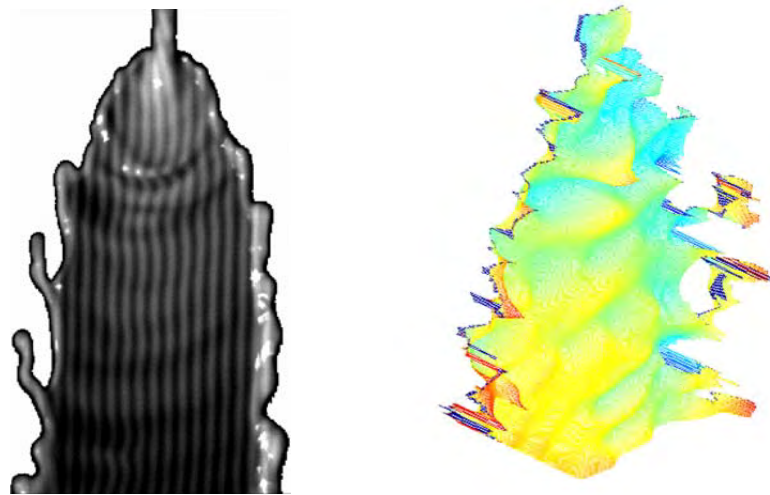

Figure 4-15: Raw image of digital fringes projected onto liquid the liquid sheet (left), and 3-D surface topology extracted by analyzing the deformation of the fringes (right).

These experimental data provide high fidelity quantitative information for the validation of numerical models. For example, the experimental data on jet impingement was compared with a RANS model developed by collaborators at the University of Massachusetts at Amherst. The goal was to evaluate the flow regimes in which factors such as surface tension and viscous

effects might be neglected, as in the case of high Re and We flows. In this case, the spray evolution is driven by turbulent dispersion, and this can be modeled with a k-epsilon model for turbulence.

Figure 4-16 shows a comparison of the data between the numerical simulations and experiments. The data from -1.5 mm upstream of the impingement point to 4.5 mm downstream shows excellent agreement from the free jet case to the case with significant atomization, respectively. In this manner, it is possible to predict the spray development process in the limit where Re and We are very high. As such, the effects of surface tension and viscosity are no longer dominant. This shows the utility of having quantitative information to differentiate subtle changes in the spray profile. However, it is of interest to make a similar comparison with gel radiography data to evaluate the effects of surface tension and viscosity in the case of gels. Additional work is also necessary to ensure grid independence and compare data for other operating conditions.
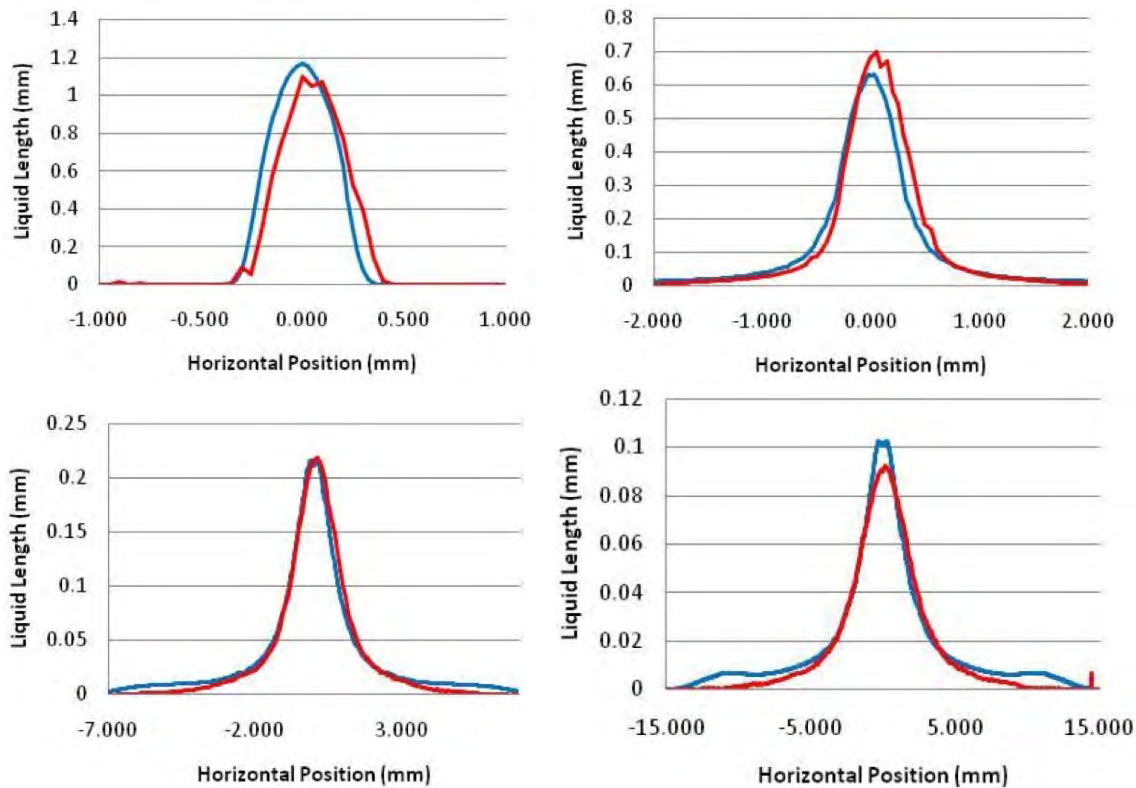
Figure 4-16: Preliminary comparison of experimental data and RANS model at -1.5 mm (top, left), 0 mm (top, right), 1.5 mm (bottom, left), and 4.5 mm (bottom, right) from the point of impingement to test effects of turbulent dispersion. Blue curve is from the simulation and red is experimental.

In summary for the effort to implement advanced diagnostics, it was found the typical optical techniques were not sufficient to extract information about the mass distribution within the spray. However, X-ray radiography and X-ray fluorescence were found to be useful for a wide range of conditions. This allowed detailed analysis of the optically complex impingement zone and extraction of important features that control the local mixing process.

The spatial and temporal scales of the mixing process were found to be very short within the impingement zone, with transmitting mixing occurring even for gelled liquids due to the high shear rates and low local viscosities. This points to the relevance of 3-D effects during the merging process and potentially significant fluid-chemistry interactions at the impingement point prior to the onset of gas formation or chemical reactions. However, the high strain rates that exist near the point of impingement drop substantially as the sheet spreads laterally and propagates downstream. Hence the sheet structure for higher gel loadings differs substantially from that of water. Detailed comparisons of sheet formation with Newtonian fluids of varying viscosity furthermore revealed information about the magnitude of the local strain rate in the flow and the effects of material properties on the spray structure.

Finally, techniques were devised to for instantaneous quantitative measurements of the mass distribution and surface instability wave amplitude and frequency, and preliminary comparisons of spray mass evolution were made with a time-averaged RANS model developed by collaborators within the MURI project.

5.0 Non-Reacting Droplet Dynamics

The study of non-reacting droplet dynamics was split into two topics: the study of droplet breakup and droplet collision.

For collision, the computational study solved the incompressible Cauchy equation of momentum conservation on a cell centered finite volume mesh. Conservation of momentum, Eq. 5.5.1 was solved on moving, deforming control volumes.

$$\varrho\left(\frac{\partial \mathbf{u}}{\partial t}+\nabla\cdot\varphi\mathbf{u}\right)=-\nabla p+\nabla\cdot\sigma \tag{5.1}$$

The variable φ is the volumetric flux, $\mathbf{u}$ is velocity, and p is the pressure, all defined at cell faces. ϱ is the density and σ represents the deviatoric stress tensor before application of a constituative stress model. In this work there are two stress models employed to solve for a stress tensor τ: classical Newtonian and the Phan-Thien-Tanner viscoelastic model. For Newtonian cases τ is defined as

$$\tau=\mu[\nabla\mathbf{u}+(\nabla\mathbf{u})T] \tag{5.2}$$

where μ is the dynamic Newtonian viscosity of the fluid. Among the models compiled in the viscoelastic CFD library by J. Fávero[28] (the library used in this study) is the Phan-Phien-Tanner consituative stress model by Xue et al [29] which is of the form:

$$f(tr(\tau))\tau+\lambda\nabla\tau=2\eta\mathbf{D} \tag{5.3}$$

The symbol $\nabla(.)$ represents the upper-convected derivative and λ is the stress relaxation time of the fluid. $\nabla\tau$ is then defined as

$$\nabla\tau=\frac{D\tau}{Dt}-\tau\cdot\mathbf{L}-\mathbf{L}^{T}\cdot\tau \tag{5.4}$$

$\mathbf{L}$ represents the effective velocity gradient

$$\mathbf{L}=\Delta\mathbf{u}-\zeta\mathbf{D} \tag{5.5}$$

where ζ is a shear modifier which represents relative slip of polymer chains. **D** is the symmetric rate of deformation tensor

$$\mathbf{D} = \frac{1}{2}(\nabla\mathbf{u} + (\nabla\mathbf{u})^T) \qquad (5.6)$$

The stress coefficient is

$$f(tr(\tau)) = 1 + \frac{\lambda\varepsilon}{\mu_p} tr(\tau) \qquad (5.7)$$

where ε is an effective extensional viscosity modifier and used along with ζ as a fitting parameter. The effective polymer viscosity is μ_p and $tr()$ is the tensor trace operator. Because $f(tr(\tau))$ is linear with respect to τ, this particular formulation is more commonly known as the linear Phan Thien Tanner (LPPT) model.

Due to the inherent numerical instability of the high Deborah number simulations being considered, the both-sides-diffusion (BSD)[29] technique is used. This makes the assumption that the fluid is comprised of two rheologically distinct components: a viscoelastic-polymeric solute and a Newtonian solvent with independant viscosities μ_p and μ_s respectively. Additional diffusion terms are then added to both sides of the momentum equation as shown in Eq. 5.8 which greatly improves numerical stabiliy.

$$\varrho(\frac{\partial\mathbf{u}}{\partial t} + \nabla\cdot\varphi\mathbf{u}) - (\mu_s + \mu_p)\nabla^2\mathbf{u}$$
$$= -\nabla p + \nabla\cdot\tau - \mu_p\nabla^2\mathbf{u} \qquad (5.8)$$

This is the final form of the momentum equation used in simulation. While many previous numerical studies of droplet collisions employ the interace capturing volume of fluids method (VOF), this paper uses an explicit interface tracking method by Dai et al.[30]. In this approach, the free surface corresponds to a (tesselated) surface of zero thickness, as opposed to interface-capturing Eulerian techniques, where the interface is of finite thickness with smoothly varying properties. A particularly attractive feature of this interface capturing approach is the precise description of interface curvature, which allows surface tension calculations to be performed with a high degree of accuracy and ensures mass conservation up to machine accuracy.

The overall code stucture uses the Open Source Field Operations and Manipulations (OpenFOAM) CFD library by Weller and Jasak[31]. Throughout the literature, the Weber number ($We = \varrho U^2 R/\sigma$), Reynolds number ($Re = 2\varrho RU/\mu$), and impact parameter (χ) are considered the primary dimentionless groups in a study of collision outcome regimes where U is the relative droplet velocity and R is the droplet radius. With the addition of a viscoelastic dimentionless group, the Deborah number ($De = \lambda U/R$), to the typical droplet collision parameters illustrated in Fig. 5-1, a large three dimentional parameter space is created. As this is a preliminary investigation into viscoelastic rheological effects on collision outcomes, parametric data generation will be limited to the plane $De = 70$.
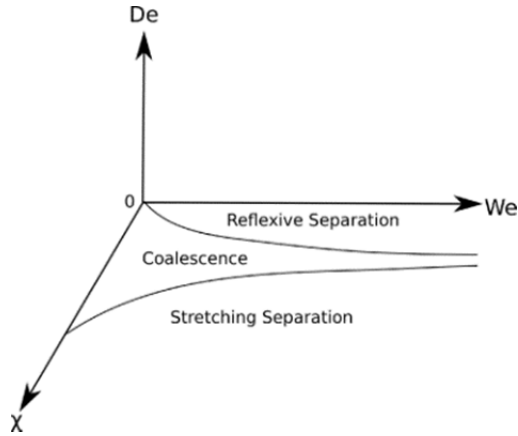
Figure 5-1: Representative viscoelastic collision outcome parameter space with the plane _De_=0 representing a Newtonian fluid.

The further validate the free surface algorithms, benchmark experiments performed by Qian and Law [32] were reproduced in the simulation environment. Good qualitative agreement is shown in Fig.5-2.
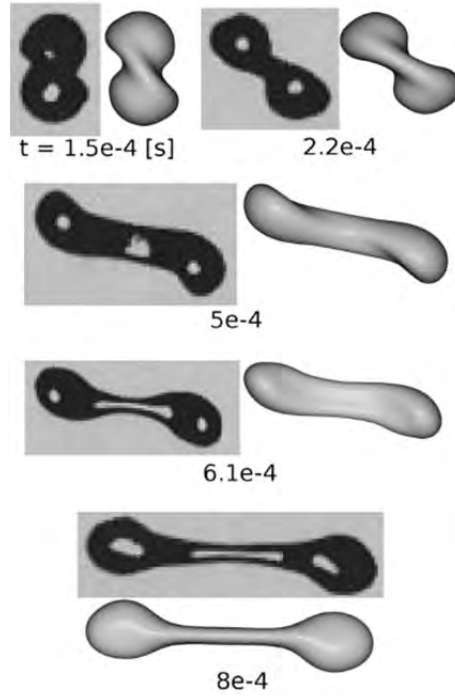
Figure 5-2: Qualitative time paired comparison of experimental run "o" from Qian and Law[32] and simulation result. _We_=60.8,_Re_=313.7,_χ_=0.68.

There exists an analytical solution to the deviatoric stress and velocity profiles of a PTT fluid in pressure driven channel flow derived by Olivera and Pinho.[33] Following a similar validation as G. S. de Paulo et al.[34], these solutions are used to verify implementation of the LPPT model. Case assumptions include no slip velocity conditions at both walls and a channel center line at

$y=0$. A pressure gradient ∇p is prescribed along the flow direction. Analytical velocity and stress profiles are shown to be in excellent agreement with simulation results as shown in Fig.5-3.
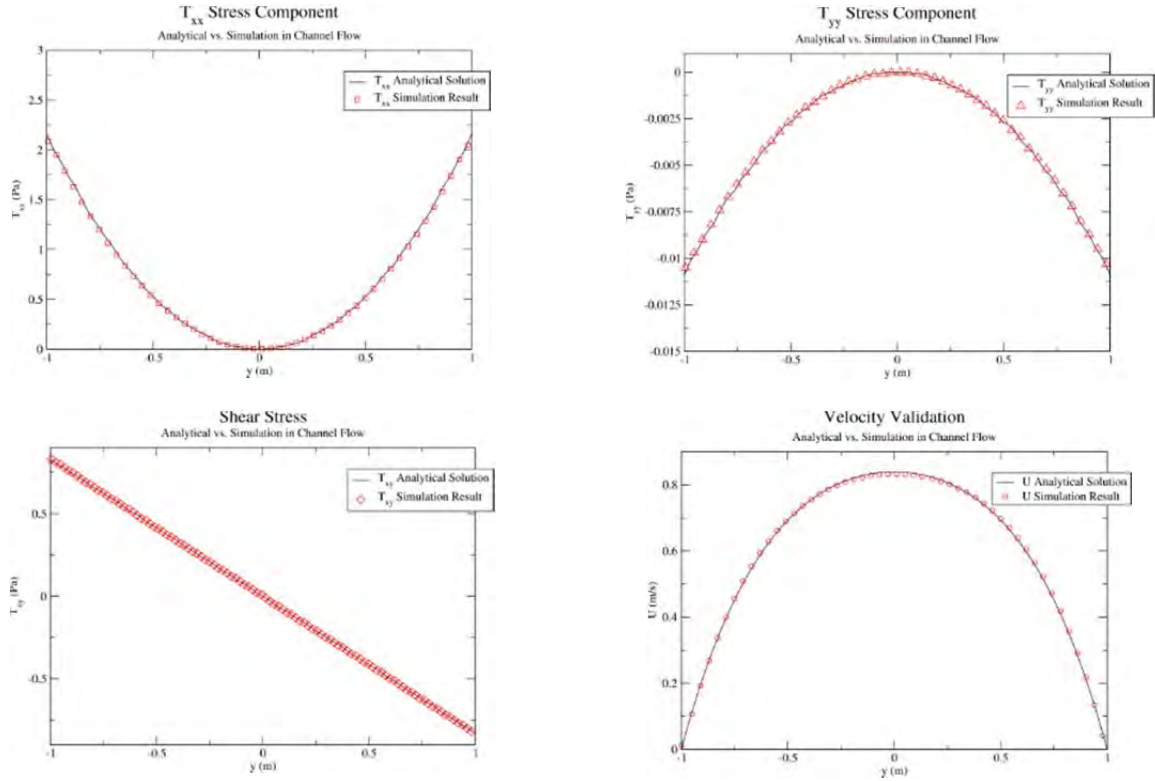

Figure 5-3: Comparison of simulated PTT fluid in channel flow against the analytical solution.

Time lapse images of a simulated viscoelastic droplet collision are displayed in Fig.5-4 along with relevant kinematic and flow parameters. This type of collision outcome is considered a *stretching separation* mode. For collisions at this *De*, viscoelastic effects do not come into play until the final stages of the collision. It is in these final moments that surface driven instabilities initiate the ligament drainage process and begin to collapse the surface onto a point. This cylindrical drainage takes the form of a rapid extensional flow which quickly increases the Troutan ratio effects of the extra viscoelastic stress model. Sample scans of the first normal stress difference ($N_1 = \tau_{xx} - \tau_{yy}$) along a line co-axial with the ligament orientation of frames A-D from the time lapse images are shown in Fig.5-5. There is a rapid jump in viscoelastic stress as the two ligament pinch points drain and extensional gradients increase.
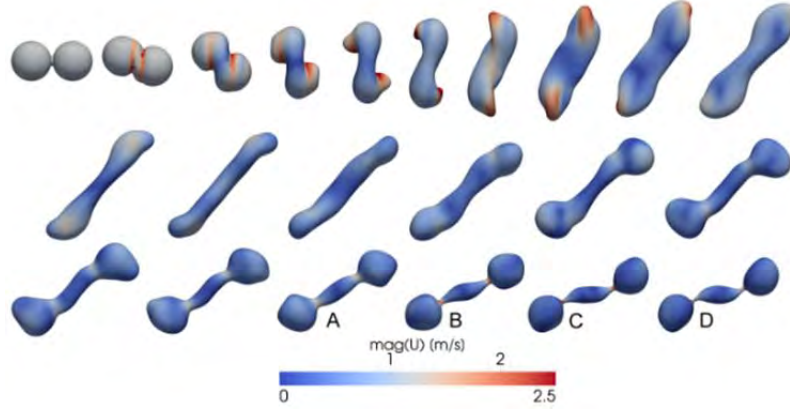
Figure 5-4: Profile snap shots of a viscoelastic droplet collision. χ=0.68, *We*=28.7, *Re*=874, *De*=0.2. The time duration between images is 8e-5. The surface is colored by velocity magnitude. Stress profiles of frames A through D are illustrated in Fig.5-5.
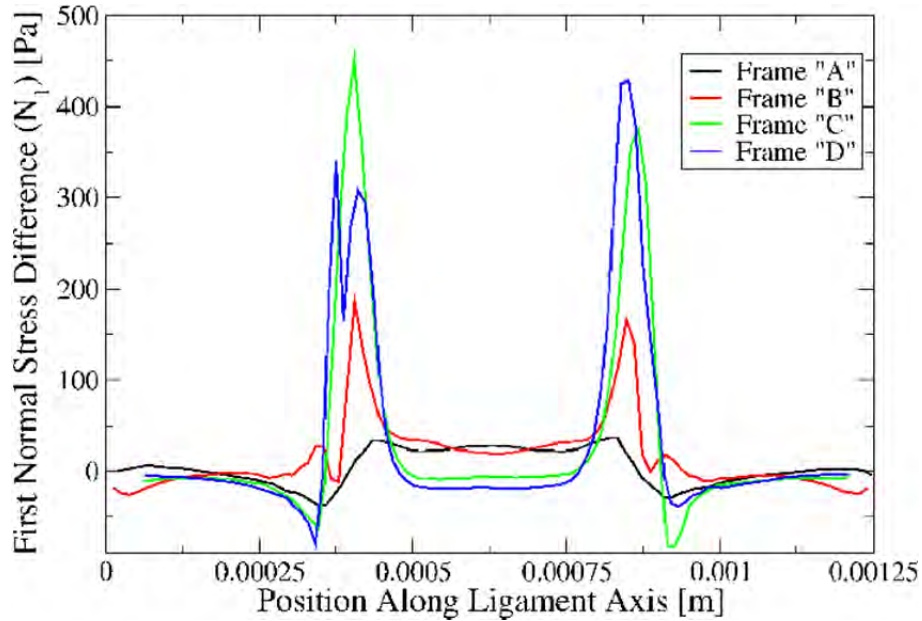
Figure 5-5: Line samples of the first normal stress difference ($N_1 = \tau_{xx} - \tau_{yy}$) of the frames labeled A though D in Fig.5-4. The sample line was re-oriented each time step to be co-axial with the ligament. Stress peaks correspond spatially to the two pinch off points between the middle ligament and two satellite droplets.

Deborah number effects on the late stages of a droplet collision can be observed in Fig.5-6. Here, both the pinch points and the middle ligament are stabilized by additional viscoelastic stress; increasingly so in the higher De droplet. The higher De droplet's stability is evident by the thicker pinch points and a more cylindrical central ligament. Both frames are time-paired.
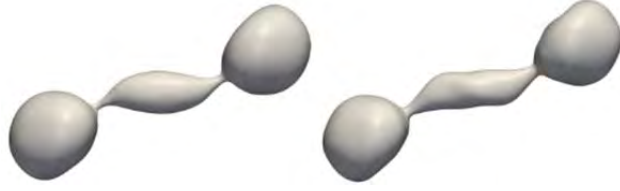
**Figure 5-6: Time paired side-by-side comparison of the final stages of two droplet collisions. Collision parameters: χ=0.68, *We*=28.7, *Re*=874, Left: *De*=0.2, Right: *De*=2.0. Time = 0.001632.**

However, due to the detrimental effects of viscoelasticity on atomization, the most likely gellants will likely not be strongly viscoelastic. Thus, it may be useful to consider a xanthan gum solution, as characterized by a Carreau-Yasuda fit. Sample rheology from the Sojka lab is shown in Fig. 5-7.
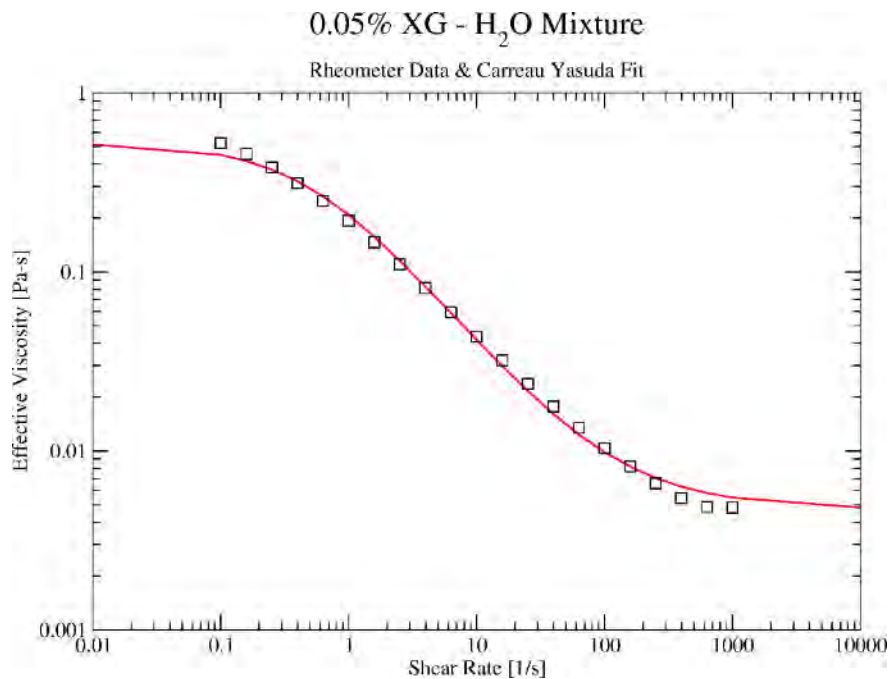
Figure 5-7. Rheometer data for a xanthan gum mixture and the corresponding Carreau-Yasuda fit.

We then examine the trends in viscosity in the part of the droplets that are strained during collision. An illustration of this interaction zone and the line along which viscosities are sampled is shown in Fig. 5-8. This interaction zone is so strongly sheared, that the viscosity remains near the lower plateau value, as shown in Fig. 5-9. These results suggest that the non-Newtonian behavior of colliding droplets composed of shear-thinning fluids may be greatly simplified: the fluid viscosity is practically pegged at the high shear limit.
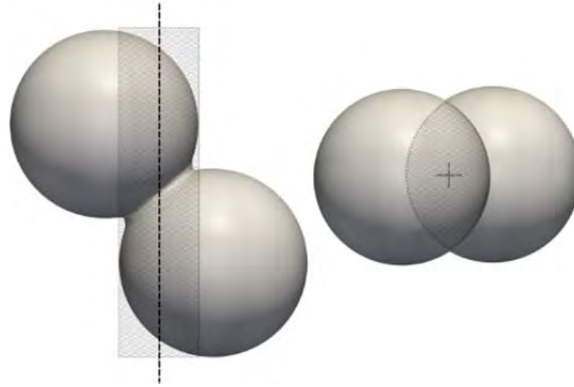
Figure 5-8. The interaction zone between two colliding droplets.
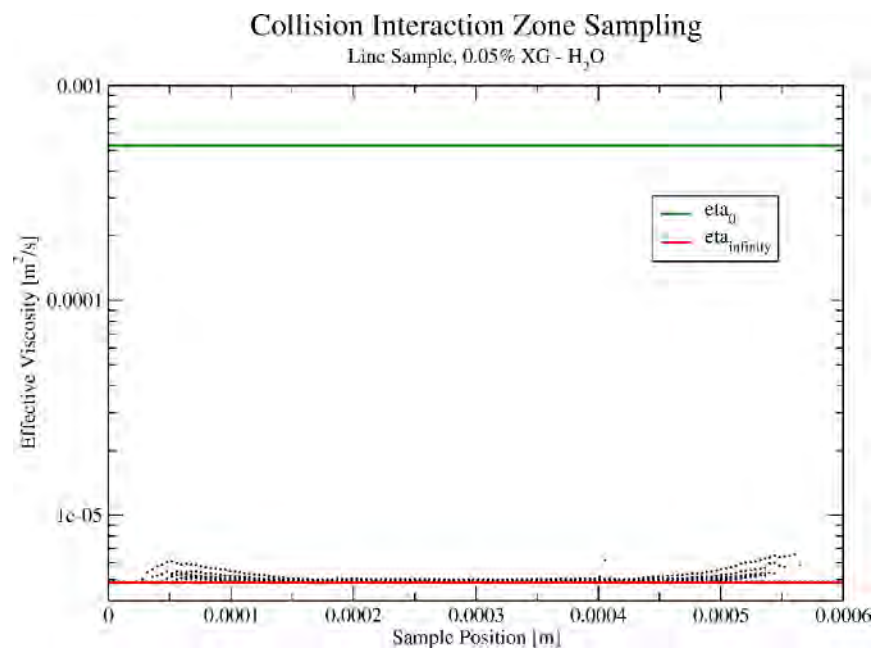
Figure 5-9. Viscosity extracted from a CFD calculation of colliding droplets
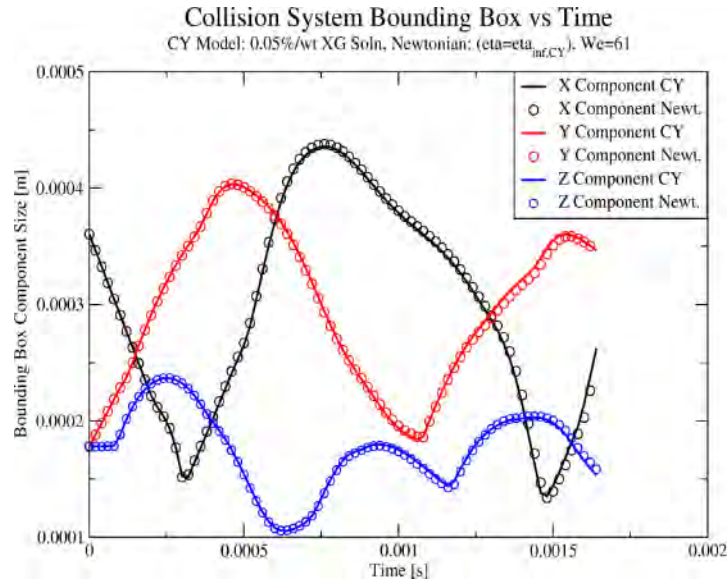
Figure 5-10. The bounding box around a system of colliding droplets. The calculation was performed with both a Carreau-Yasuda fluid and a constant viscosity, Newtonian fluid with a viscosity equal to the high-shear viscosity limit.

was confirmed by repeating the calculation with a constant viscosity equal to the high-viscosity limit and noting that the differences were negligible Fig. 5-10 shows a quantitative test of how the governing physics of non-Newtonian collisions may be simplified. The x,y and z extent of the colliding droplets were calculated by fitting a bounding box around the droplets. Thus, Fig. 5-10 shows three-dimensional quantification of the shape of the colliding droplets. We see that the sizes of the bounding boxes are identical in the two situations. This result strongly suggests that droplet collisions of non-Newtonian droplets are simpler than they first appear.

Due to the strong interaction of surrounding gas and droplet breakup, a volume of fluid approach was used in the study of droplet breakup. The experimental conditions used at Purdue were approximated as a two-dimensional axisymmetric system. The domain was moved with the droplet in order to more optimally dedicate computational resources.

For droplet breakup, the interaction of rheology and droplet behavior was found to be, in contrast, extremely complicated. The first issue was how to characterize the fluid viscosity over the whole range of shear stresses, since this broad fit was found to be necessary for good agreement.
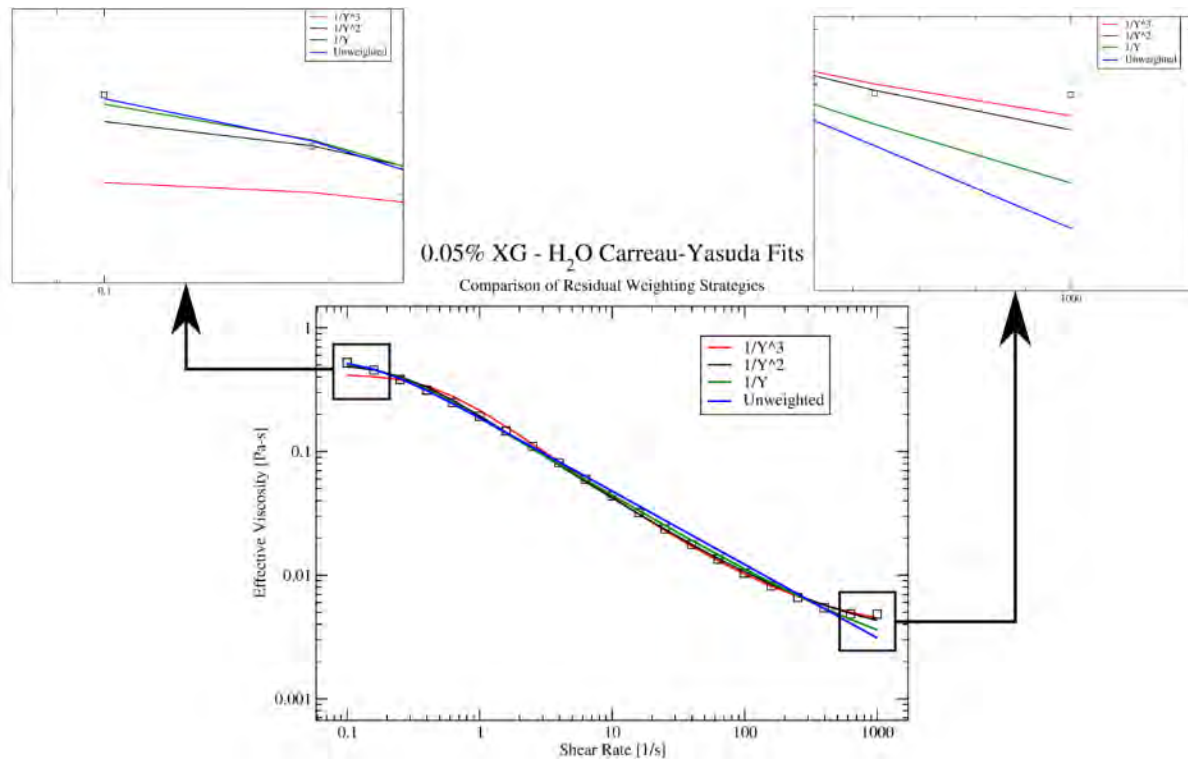
Figure 5-11. An examination of different fitting procedures to determine the Carreau-Yasuda parameters. Fits weighted by the Y values, to various powers, and unweighted fits, were compared to experimental data.

Even when using weighting to better fit the extremely high or low shear sections of the viscosity curve, we could not get a perfect fit. Since the viscosity found in the droplets spans the entire breadth of the curve, these results suggest that a piece-wise continuous fitting process be used. For example, spline fits might offer a better viscosity model.

An example of how broad the viscosity range can be is seen in Fig. 5-12, below. The surfaces of constant viscosity uniformly span 10 intervals from the minimum to maximum viscosities. High viscosity areas correspond to low shear/stagnation zones, while the low viscosity areas correspond to areas of high shear. Of particular interest are the large toroidal vortices created by shear stresses at the interface.
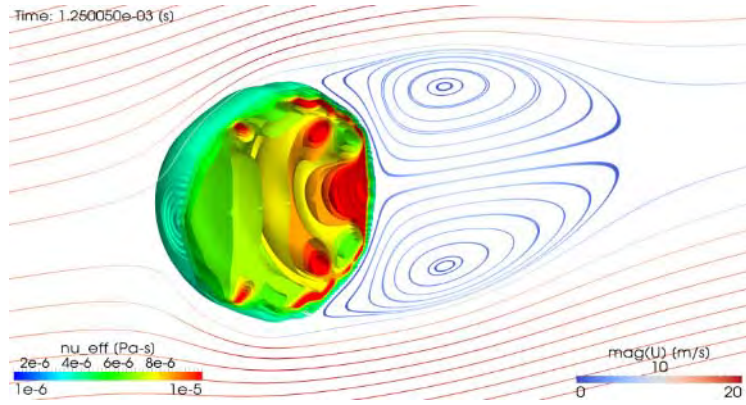
Figure 5-12. Viscosity iso-surfaces inside the droplet and streamlines colored by velocity outside the droplet.
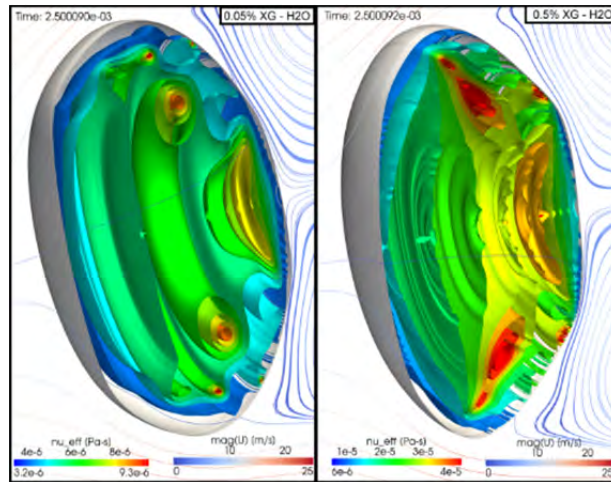
Figure 5-13. Internal viscosities for two different xanthan gum concentrations. Streamlines are shown outside the droplets colored by viscosity.

The results of Fig. 5-13 indicate that the vertical structure in the droplet changes with the changing rheology. The rheological effects are also reflected in the droplet shape, even at this early stage of breakup.

Overall, the assumption of axisymmetry does create some differences between the modeling and the experiments. Because, in the experiments, the droplet falls into the jets, the droplet does not immediately feel the full impact of the jet. In the case of the model, the assumption of axisymmetry, even with the use of a gradually increasing gas velocity slightly accelerates droplet breakup predictions as compared to experiments, as shown in Fig. 5-14. However, the predicted trends are not affected by these simplifying assumptions, and so the computational model is found to be predictive.
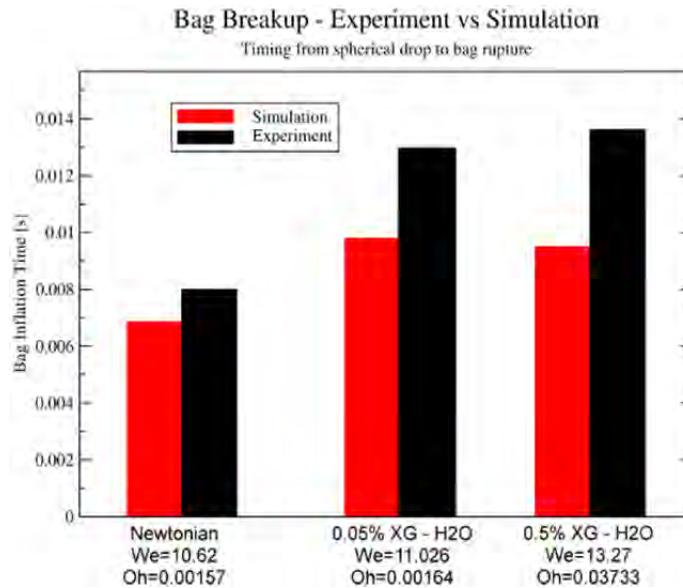
Figure 5-14. Comparison between experiments of Snyder and Sojka to the present computational predictions.

6.0 Reacting Droplet Dynamics

A. Experimental Studies

6.1 Objectives

Classical ignition models due to Catoire et al. and Seamans and Dawson[35,36] are limited to gas-phase reactants because so little information exists about these liquid-phase reactions. For these reasons, experimental data on gas production delays and gas production rates are needed to improve these models or equivalent reacting flow simulations using modern CFD tools (Section 6.B). These factors serve as motivation for the present study.

A specific objective of the study is to investigate hypergolic contact at various impact velocities and impact geometries by measuring gas production delays and gas production rates. High-speed video provide quantitative information on gas production and liquid dispersion subsequent to a collision of a given energy level. Recent low Weber number collisions assessed by Dambach et al.[37] has revealed "explosive" behavior characterized by very rapid gas generation and liquid dispersion after a short incubation period. A secondary objective of this study is to enhance understanding of these events. By extending the Weber number range studied by Dambach[37], we seek to develop a classification of the various outcomes from collision events.

6.2 Approach

The droplet contact chamber, shown in 1, has been used in previous ignition and combustion experiments, and was modified for use in the present research. The chamber was designed to

control and observe the contact between two hypergolic propellants under variable operating conditions. The chamber pressure can be controlled from 1 to 100 ± 1 psia, the temperature can be controlled from 0 to $40 \pm 1°C$, and the atmosphere inside the chamber can be controlled (Ar, N_2, He, air, etc.).

The following experimental variables were studied for their influence on gas production rate and the explosion phenomenon: drop impact velocity, oxidizer temperature, and impact geometry. The drop impact velocity was varied from 1.2 to 2.9 m/s by changing the height of the chamber extension. The oxidizer temperature was varied from 10 to 30°C by cooling the chamber with a TECA AHP-301-CPV cooling plate and cooling the oxidizer in a water bath. The impact geometry was varied from an impact parameter of 0 to 1 by changing the location of the oxidizer pool relative to the impact location of the fuel drop (An impact parameter of 0 corresponding to a head-on collision, and 1 corresponding to a glancing collision). Specific instrumentation and procedures used are detailed in Reference 38.
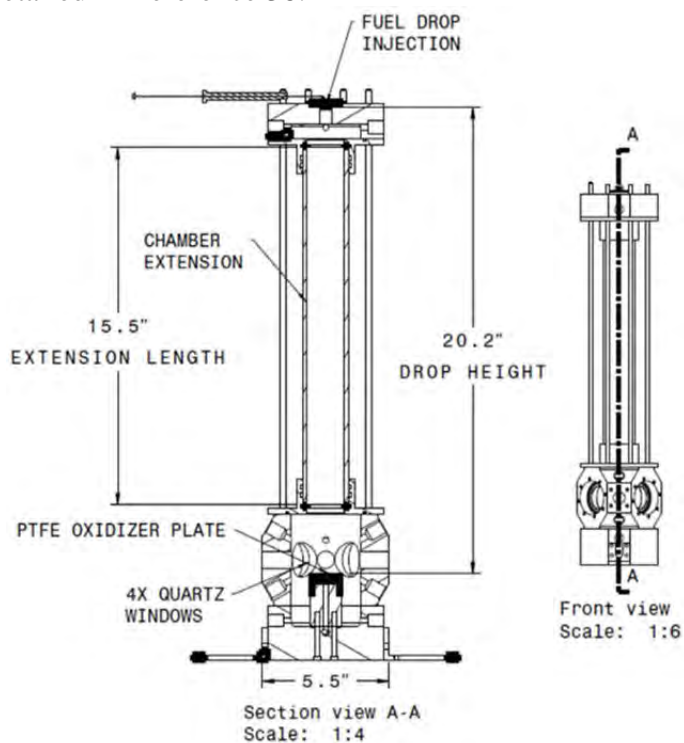
Figure 6-1. Droplet contact chamber cross-section.[11]


6.3 Results

The liquid-phase reactions in MMH/RFNA were studied by capturing impacts at 100,000 FPS, and the first measurement of the time between contact and gas production has been made. These measurements aided in the development of liquid-based hypergolic ignition models by calibrating pre-exponential factors in Arrhenius rate equations to match physical events observed experimentally.

Impact Characterization: Bouncing, Splashing, and Explosion Regimes
While analyzing the test videos, similarities were observed among impacts that suggested a natural grouping of tests. It soon became apparent that different types of impact were occurring. These impact types did not transition linearly from one regime to the other; they were categorically distinct types, which explained some of the scatter in the data.

1) "Explosive" Impacts

Impacts resulting in explosive behavior were categorically different from other tests. Explosions had the following characteristics: The pool was relatively undisturbed on impact, with few, if any, secondary droplets created. There was a very distinct spike in the gas production rate that was an order of magnitude greater than anything else observed. And, most importantly, for every explosion, there was a delay between contact and explosion where the fuel droplet had completely merged with the oxidizer pool. For MMH/RFNA, this explosion delay was 2 ± 0.5 ms, and for MMH/WFNA, the delay was 7 ± 1 ms. Select images from an explosion impact are shown in Figure 6-2. The result of an explosion was a large cloud composed mostly of propellant vapors with some small secondary droplets accelerated away from the point of impact at an average velocity of 7 ± 4 m/s, although local gas velocity has been measured at over 30 m/s. The average maximum gas production rate among explosion tests was 18 ± 16 cm^2/s. The impacts were so violent that little propellant remained in the impact zone.
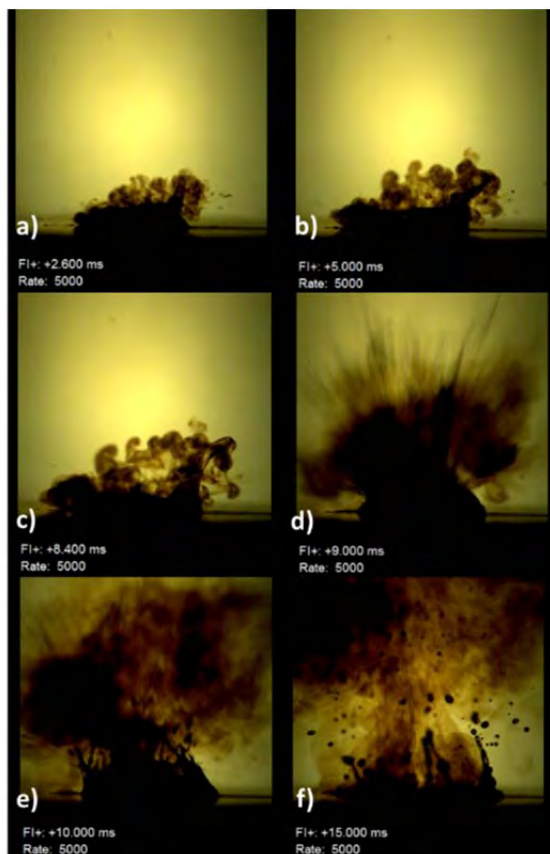

Figure 6-2. Images from a MMH/WFNA explosion impact. d= 2.4 mm, v = 1.3 m/s, We = 100, pool volume = 50 μL. All times are referenced to contact.

2) Bouncing Impacts

It was observed that for some impacts, the fuel drop bounced out of the oxidizer pool mostly intact. These impacts are categorically different from explosions, although they occur under very similar test conditions. The bouncing effect is likely similar to the Leidenfrost effect where gases produced by the contact of the hypergolic propellants create a gas cushion that repels the drop, preventing further liquid contact.[39]

The characteristics of a bounce impact were as follows: These tests were the least energetic of the impacts, with reduced gas area, minimal pool disturbance, and the lowest gas production rates observed: $2 \pm 1 \ cm^2/s$. The rebounding fuel drop was sometimes obscured from view by the gas produced on contact. For these tests, bouncing was determined by the characteristic gas production profile shown in Figure 6-5, and by delayed gas production centralized away from the point of impact. In this case, the drop makes initial contact with the pool, creating the initial spike in the gas production profile and producing the gas that obscures the rebound. Minimal gas is produced while the drop is in the air for $30 - 40$ ms, then the drop re-impacts the pool, usually at a location away from first contact, and a weak, secondary gas production event follows, which is observed as a distinct crest in the gas production profile well after contact. This sequence of events and characteristic gas production profile were confirmed for tests where the rebounding drop could be observed directly, like the one shown in Figure 6-3. The result of a bounce was minimal liquid contact and mixing, minimal gas production, and appreciable propellant vaporization only after re-impact, 50 ms after contact.
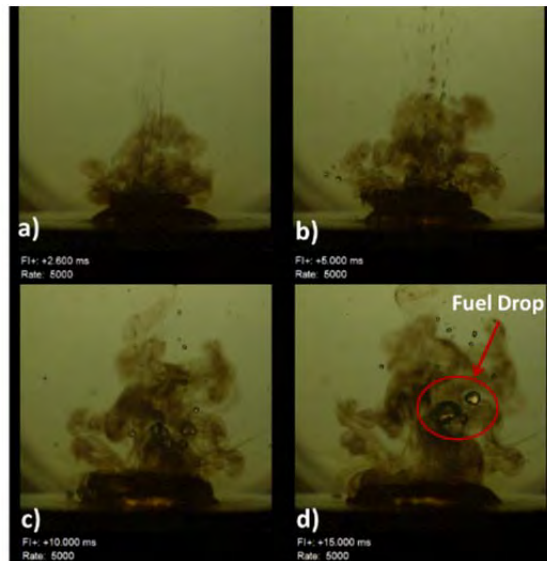

Figure 6-3. Drop of MMH bouncing out of a pool of RFNA. d = 2.3 mm, v = 1.3 m/s, We = 99, pool volume = 60 µL. All times are referenced to contact.

3) Splash Impacts

The last categorically distinct type of impact was determined to be splashes. To begin, it is important to distinguish these from the non-reactive splashes discussed in section II. Impacts conducted with water showed good agreement with results by Rodriguez and Mesler[32], with crown formation but no secondary droplets at an impact velocity of 1.2 m/s and crown formation with minimal secondary droplets at 2.9 m/s. The splashes described herein are significantly enhanced by gas production of the reactive liquids.

The characteristics of a splash impact were as follows: There was significant pool disturbance immediately on contact. It appeared as though the droplet and pool shattered on contact. Nearly all gas production occurred on contact with gas production rates high enough to shatter the pool, at 3 ± 1 cm^2/s, but still less than a quarter of those of an explosion. Figure 6-4 shows frames from a splash impact at the same time after contact as those in Figure 6-2 and Figure 6-3. The results of splash impacts were much more consistent than either explosions or bounces. They produced a cloud composed of mostly secondary droplets and some propellant vapors accelerating away from the point of impact at 3 ± 1 m/s.
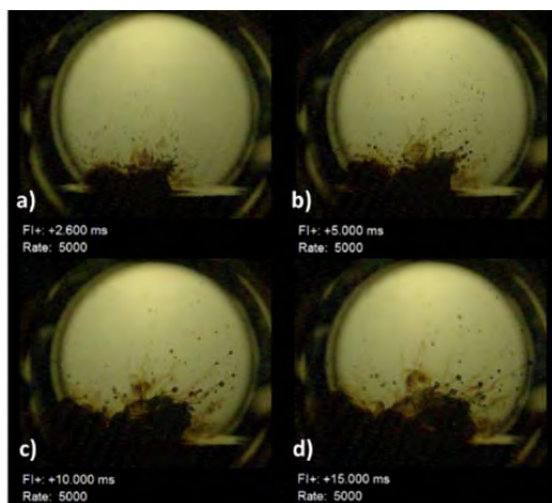
Figure 6-4. A drop of MMH impacting a pool of WFNA resulting in a splash. d = 2.4 mm, v = 2.85 m/s, We = 501, pool volume = 40 μL. All times are referenced to contact.

Impact Characterization: Gas Production Rates

MATLAB[ref] was used to process the videos and measure the gas production rates, as well as the velocity of the gases and droplets resulting from the impact. A complete description of the algorithm is given by Forness.[38]

Examining the gas production history of each impact type revealed a characteristic profile for each, plotted in Figure 6-5. For an explosion impact, there was initial gas production on contact, then an induction time with minimal gas production, followed by a substantial increase in the gas production rate that goes off the scale to 40.6 cm^2/s at 9.0 ms. After the explosion, the gas production ended rapidly, and the gas area actually decreased as the vapors quickly moved out of the field of view of the camera.

Splash impacts produced a monotonically increasing gas area with a noisy, but steady, decrease in gas production after contact. Maximum gas production always occurred on contact, with a sharp decrease soon thereafter.

The most easily recognizable profile was that of bounce impacts. For a bounce, there was initial gas production on contact, similar in magnitude to that of an explosion. The gas production decreased to nearly zero and remained at that level for 30 – 40 ms as the drop rebounded. Gas production slowly increased as the drop came back into contact with the pool, creating a crest in the gas production profile long after all other events had ceased in an explosion or splash impact.

Applying the categories just defined, the data was examined using two different measures of impact geometry defined in literature: impact parameter B and impact angle φ.[33] Impact parameter is a measure of how centered the impact is, while impact angle is the angle between the droplet velocity vector and the pool surface-normal vector. These two measures are equivalent for identical geometries; however, the oxidizer pool shape varied during testing, despite all efforts to maintain constant size and shape. Figure 6-6 illustrates how two tests can have the same impact parameter but different impact angles. Inspection of Figure 6-7 reveals that impact angle and not impact parameter is the more important measure of impact geometry because it successfully separated bounce and explosion tests.
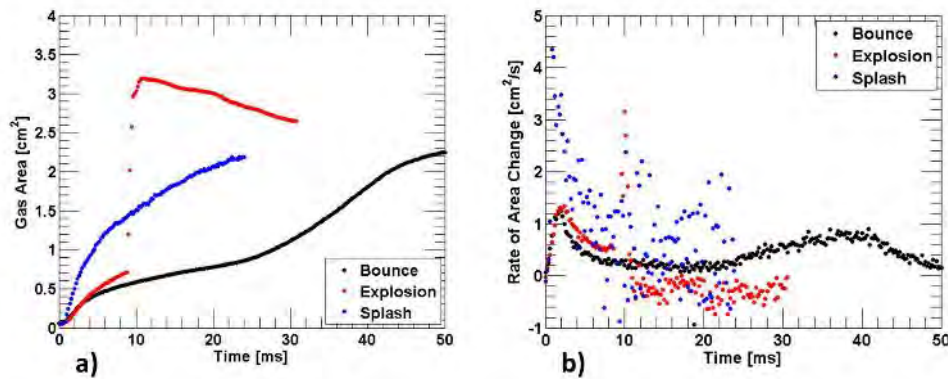
Figure 6-5. Gas production profile for MMH/WFNA bounce, splash, and explosion impacts. Explosion rate of gas production peaks off the scale at 9.0 ms with a maximum of 40.6 cm^2/s, and order of magnitude greater than other impacts.
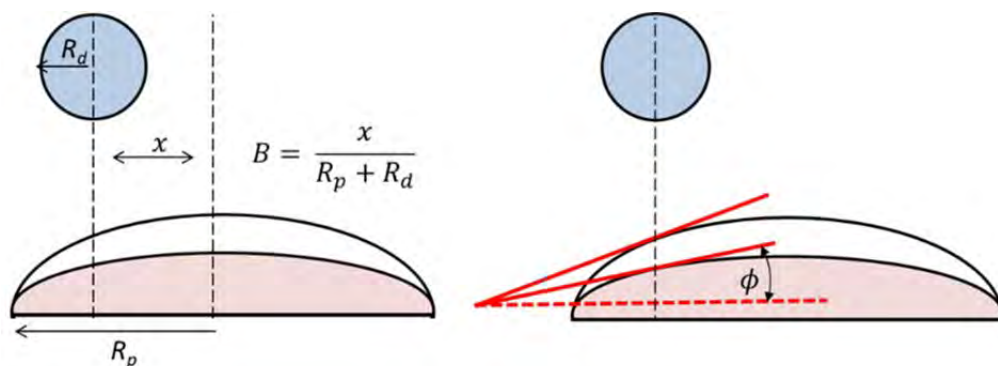
**Figure 6-6. Impact geometry defined by impact parameter, _B_ (Left), and impact angle, φ (Right). Both pool contours have the same impact parameter but different impact angles.**

The three types of impacts observed – bounces, explosions, and splashes – can be predicted based on the impact Weber number and the impact angle, as shown in Figure 6-7b. Any collision above a critical Weber number of 250 will result in a splash, regardless of impact geometry. Below that critical Weber number, explosions will occur for angles less than seven degrees and bounces for angles above seven. Tests were not performed for large impact parameters or impact angles because the drop would impinge on the oxidizer plate as well as the pool, which is not consistent with simulating a drop-on-drop collision. Results are nondimensionalized in terms of Weber number, however, only the impact velocity was varied. More tests are needed to confirm that Weber number is the controlling parameter.
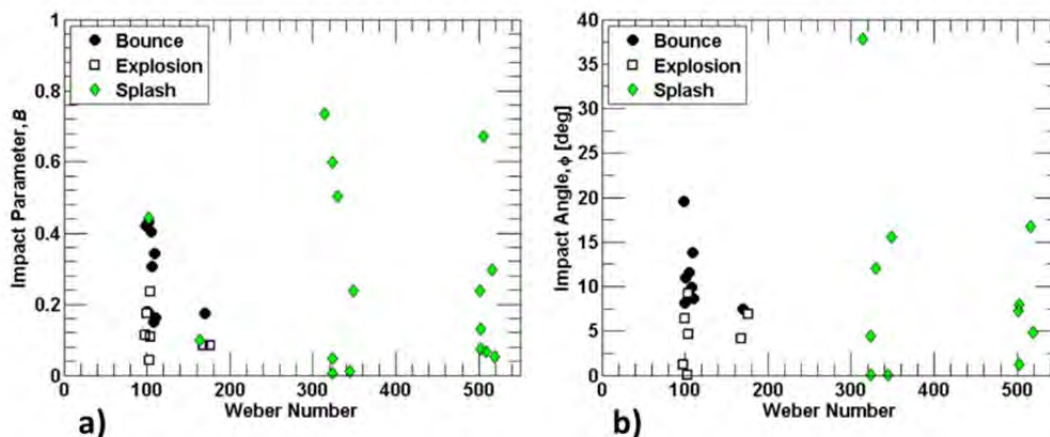
Figure 6-7. Impact types plotted against two measures of impact geometry, impact parameter a) and impact angle b) vs. Weber number. All data from MMH/WFNA tests.

Figure 6-8 provides another perspective to enhance qualitative understanding of the impact regimes. Here, we consider the interaction time and its relationship to the chemical time. The chemical induction time is not a function of impact velocity, whereas the fluid interaction time scales as the inverse of this parameter. When the fluid interaction time is long compared with the chemical time, bouncing or explosive behavior depending on whether we have a grazing or a nearly head-on collision. When the chemical time is long compared to the interaction time,

splashing results as there is insufficient time for gas generation and chemical interaction to contribute significantly to the energy of collision.
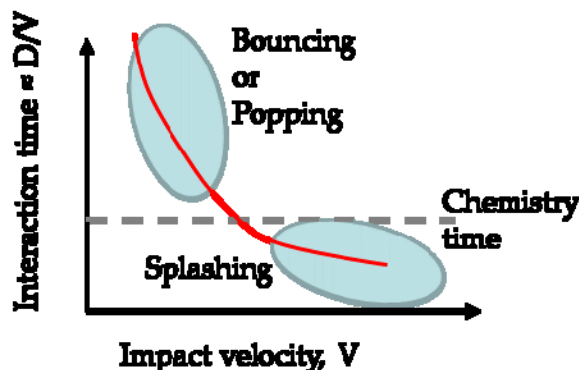
Figure 6-8. Classification of Impact Regimes in Terms of Interaction Time

B. CFD Simulations Studies

6.4 Objectives

In this work, we present a numerical model for multiphase modeling of hypergolic liquids and gels and use it to model a drop-on-pool test and a binary droplet collision involving either hypergolic liquids or gels. Prior gas-phase combustion modeling of such propellants typically assumed that the liquids had already vaporized and used elevated initial temperatures and gas-phase propellants in order to achieve ignition. The actual behavior of these propellants, however, shows that they can ignite even beginning from ambient temperature liquids. To our knowledge, this work presents the first model to include all the necessary physical processes to model the complete pathway from ambient temperature liquids to gaseous ignition products.

6.5 Methods

This work uses the volume-of-fluid method (VOF) extended to include species tracking, evaporation, and chemical reactions in compressible, non-isothermal flows. The basis for the volume-of-fluid method has been well established in the open literature[41,42], so the emphasis of this work is on integration with the tracking of both gas and liquid species, property sub-models, and chemical reaction mechanisms.

The details of the methods developed for these CFD simulations using the OpenFOAM interface are the subject of a two-part journal publication being prepared at the time of this report submission for publication in Combustion and Flame. The reader is referred to the papers authored by T. Voskuilen, C. Needham, P. Westmoreland, N. Labbe, and T. Pourpoint. The main results of these CFD studies are provided below.

6.6 Results

The influence of gelling agents on hypergolic propellant ignition is of particular interest from a storage safety standpoint and a variety of gellants and characterizations have been reported in the literature.[43,44,45] In this work, we compare the 2D model of a standard liquid drop test with experimental measurements of flame temperature and ignition delay and relate the observed behavior with both the zero-D results and some key experimental observations. Finally, we use the model to examine 3D droplet collisions of reacting and non-reacting liquids and shear-thinning Aerosil gels of MMH and RFNA to examine the effects of gelling on droplet interactions.
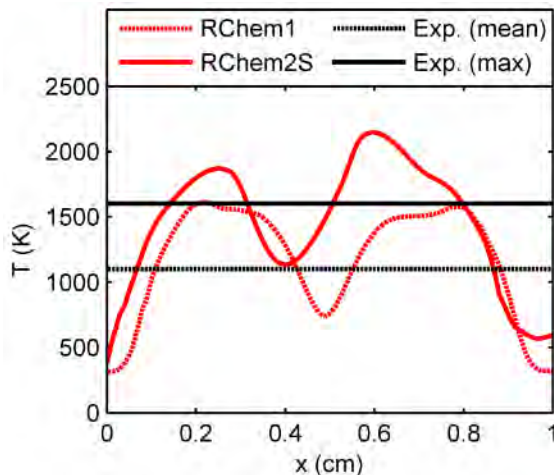
6.6.1 Results: Drop Test Comparisons

The premixed gas-phase reaction mechanism results in zero-D differ from the 2D and 3D calculations in several important ways.

First, the relevant O/F and species mass fractions in the gas phase near the evaporating liquids can be considerably different than the overall O/F and mass fractions due to the difference in volatility between the components in RFNA and other MONs. This difference can change the ignition delay and final temperature considerably.

Second, large temperature gradients exist in such a system, with the liquids remaining near their boiling point while the gas-phase temperature rapidly exceeds 2000 K. A homogenized approach that treats all components as being the same temperature would result in either unrealistically high liquid temperatures, or insufficient temperature for ignition due to the thermal mass of the liquid. Accounting for these important spatial gradients in temperature and composition necessitates a higher dimensional analysis, particularly when considering a hypergolic reaction whose ignition initiation is the result of direct liquid interactions.

The drop test simulations use a 2D rectangular domain with a width of 1 cm and a height of 2 cm. A 2-mm-diameter drop of RFNA is initialized 2 mm above a 1 mm deep pool of MMH, centered at $x = 0.5$ mm. The initial droplet velocity is 0.5 m/s and the entire domain is at 300 K. The bottom and sides of the domain are walls with the top open to a nitrogen atmosphere to mimic a drop test done in a vial. The key points of comparison from these simulations are the ignition delay and flame temperature. The ignition delay observed experimentally for these conditions ranges from 2 to 4 ms, and the flame temperature has been investigated experimentally by Dambach et al.[46] using thin filament pyrometry. A comparison shown in Figure 6-9 between the flame temperatures 4 mm above the liquid with the mean and maximum temperatures reported by Dambach shows reasonable agreement for both chemistry sets, although the mean and max temperatures are closer to those predicted by RChem1 than by RChem2S.

Figure 6-9. Comparison between 2D drop-test flame temperatures 4 mm above the liquid surface and thin filament pyrometry results from Dambach et al. [Error! Reference source not found.]**.**

The ignition delay also varied between the two chemistry sets. The modeled delay with RChem1 was 4 ms, while with RChem2S it was 1.7 ms, compared with 3 ± 1 ms observed experimentally. A key contributor to this difference is the fact that there were considerably more decomposition pathways for MMH present in RChem2S, which caused a higher heat release and faster reaction in the space between the two liquids. As one metric, at the same simulation time there was approximately 1000 times more CH_3NN between the liquids with RChem2S than there was with RChem1. This change not only contributed to the decreased ignition delay, but it also created different distributions of liquid over time. Comparing the temperature and liquid fields in Figure 6-10, it is apparent that there are considerably more gas-phase reactions occurring in the gas pocket separating the fuel and oxidizer in RChem2S.
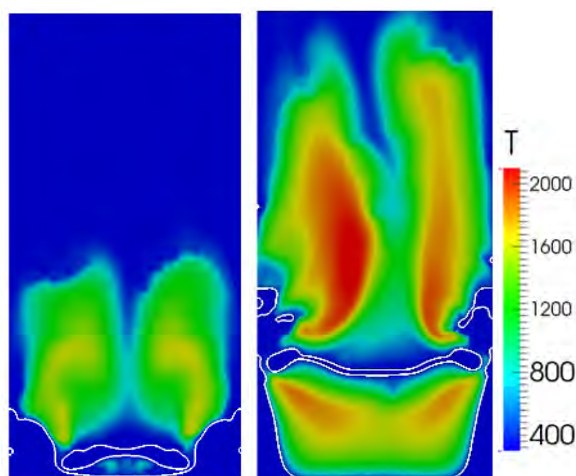

Figure 6-10. Temperatures 7.7 ms after impact of a 2 mm RFNA drop on a 1 mm deep MMH pool for RChem1 (left) and RChem2S (right). Lines show the liquid-vapor interface defined by the contour at a volume fraction of 0.5.

The higher flame temperature with RChem2S is consistent with a zero-D analysis and indicates a gas-phase O/F slightly below stoichiometric.

6.6.2 Results: Gelled and Liquid Droplet Collisions

The effectiveness of gelled hypergolic propellants is largely related to how the presence of the gellant affects the collision and reaction of a pair of gelled hypergolic droplets. In order to assess the differences between gelled and liquid droplets, we examined a moderate Weber number, off-center collision between MMH and RFNA liquids and gels of 6% and 3% Aerosil in MMH and RFNA, respectively, both with and without reactions enabled. For the initial study, the reactions were disabled in order to examine how the differences in viscosity affect the mixing and collision behavior. The generalized Weber number described by Nikolopoulos et al.[47] was used since the two droplets had unequal densities and surface tensions and gave a Weber number of 36 for the conditions in this simulation. We used this moderately low Weber number to examine the scenario where the droplets could have sufficient time to mix and react. The impact parameter for all collisions was set to 0.5 (an offset of 1 mm with 2 mm diameter droplets). The cases for non-reacting liquid and gel droplets are shown in Figure 6-11.
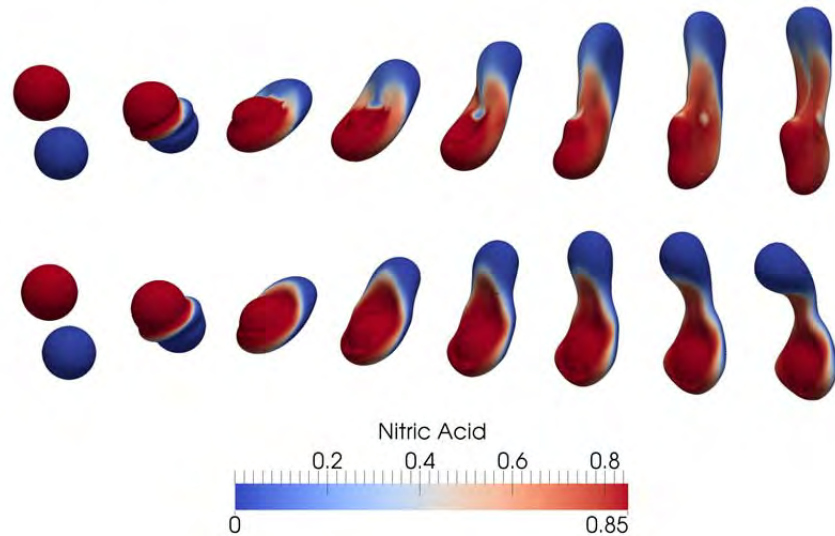
Figure 6-11. Simulations of equal momentum non-reacting liquid (top) and gel (bottom) droplet collision between RFNA (0.281 m/s) and MMH (0.5 m/s) drops with We = 36, colored by HNO$_3$ liquid mass fraction (red) spaced 2 ms starting at t = -0.5 ms relative to impact.

The major difference between the liquid and gel cases is the degree of mixing between the propellants and the shape of the merged and deformed droplets. The higher viscosity of the gels, even at the high shear limit, prevents the shear-induced circulation patterns apparent in the liquid collision. Moreover, the significantly higher viscosity in the non-sheared region of the drop maintains its original spherical shape in the gel droplet collision while the liquid droplet shapes are influenced more significantly by surface tension. Qualitatively, the degree of mixing in the non-reacting drop impacts is quite comparable to the modeling and experimental results of Focke et al.[48]

Another recent publication by Focke et al.[49] modeled off-center high Weber number droplet collisions of Newtonian and shear-thinning liquids in terms of the size and center of mass of the

agglomeration and found them to be quite similar if the Newtonian liquid viscosity was selected as an "effective" value. This effective value was close to the high shear limit for the shear-thinning gel considered, which is consistent with our results but it is important to note that this value does not necessarily correspond with the pure liquid viscosity. Moreover, although the size and degree of stretching of the liquid and gel droplets are similar (Figure 6-11) the degree of mixing between the droplets does differ significantly.

Following the non-reacting simulations, the previously described reaction mechanism RChem2S was enabled in both the liquid and gel simulations. The gellant (SiO₂) was treated as a completely inert species, so no modifications to the reaction mechanism were needed. Images of the collision simulation with liquid drops every 0.4 ms are shown in Figure 6-12 with the temperature shown on a blackbody color scale beginning at 400 K to show the reaction zones. Comparing this collision with the non-reacting version, it can be seen that the liquids rapidly form a gas layer between the droplets, which prevents further mixing and feeds the eventual combustion reaction in the gas phase.
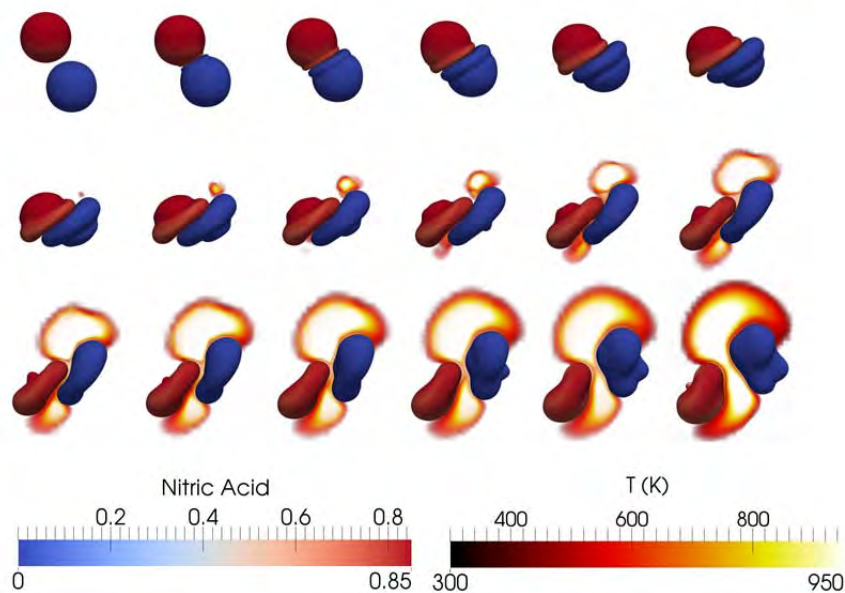

Figure 6-12. Simulations of equal-momentum reacting liquid-droplet collision between 2 mm RFNA (0.281 m/s) and MMH (0.5 m/s) droplets at We = 36, colored by HNO_3 liquid mass fraction (red) spaced 0.4 ms starting at t = -0.1 ms relative to impact. The gas cloud temperature is colored on a blackbody scale with temperatures below 400 K completely transparent. Only the back half of the temperature field is shown so the drops are not obscured.

The liquid reaction mechanism and the treatment of the liquid mixing used herein does not allow for the formation of superheated liquids along the liquid interfaces due to immediate gas production. The effect of this difference is apparent in both the liquid and gel droplet simulations, which exhibit a nearly instantaneous gas layer formation between the droplets. Inclusion of this behavior would change the way the droplets initially interact, but because the experimentally observed time scale for this phenomena is on the order of 100 to 200 μs[50], it is expected simply to make the liquid separation more explosive than is currently shown.

Although the liquid droplets do ignite, the ignition occurs in the gas plume around the contact perimeter where the vaporized propellants have sufficient time to mix. The overall droplet vaporization during this process is quite low; however, in a spray there would be many such interactions occurring, which would increase the surrounding gas temperature over time.

Similar results from the simulation of reactive gel droplets are shown in Figure 6-13 at the same sampling interval. There are differences between the gel and liquid cases worth noting. First, because the gelled fuel droplet has a lower viscosity at the high shear limit than the gelled oxidizer droplet, it is flattened upon impact more than the oxidizer droplet. This flattening creates a gas mixing zone which is on the opposite side as the liquid droplets and which acts to further separate the droplets, creating a larger distance between the propellants than was observed in the liquid simulation.
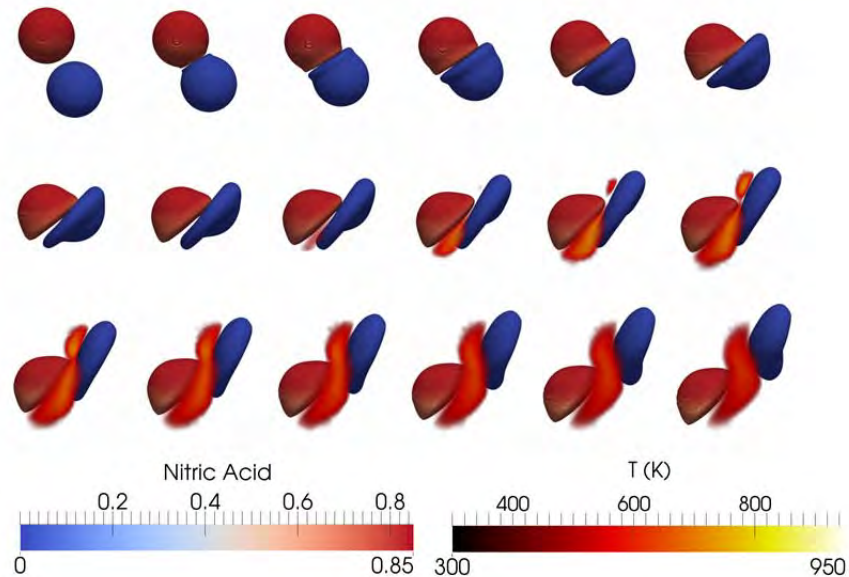

Figure 6-13. Simulations of equal-momentum reacting gel-droplet collision between 2mm RFNA (0.281 m/s) and MMH (0.5 m/s) droplets at We = 36, colored by HNO$_3$ liquid mass fraction (red) spaced 0.4 ms starting at t = -0.1 ms relative to impact. The gas cloud temperature is colored on a blackbody scale with temperatures below 400 K completely transparent.

Second, the overall droplet deformation is slightly lower for the gels due to their higher viscosity, and their recovery after collision is also slower than the liquids. The effects can be observed from the simulation images as well as from the change in surface area over time from both simulations (Figure 6-14).

The formation and bursting of a film on the surface of the gel droplet—which has been observed experimentally—was not considered in this work. The bursting film phenomenon is more relevant for a long-duration burn of a gel droplet where one of the propellants is already vaporized. In this case, the propellant droplets do not significantly vaporize and are deflected apart before their vapors have time to ignite. Comparing the maximum temperatures from the gel

and liquid cases (Figure 6-15), the differences are more apparent. The gas-phase decomposition reaction occurs about 1 ms sooner in the liquid case than in the gel case, and the interface reaches sufficiently high temperatures (greater than 800 K) to trigger an ignition event, leading to peak temperatures of around 1800 K. In contrast, the decomposition reaction in the gel case is delayed and does not build sufficient heat to trigger the ignition before the drops are deflected apart.
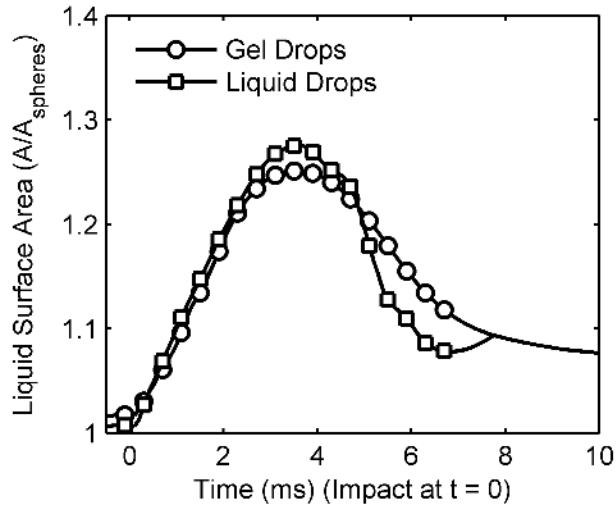
Figure 6-14. Total liquid surface area relative to the surface area of two 2-mm-diameter spheres. Marker spacing matches the image sampling frequency in Figure 6-11 and Figure 6-12.
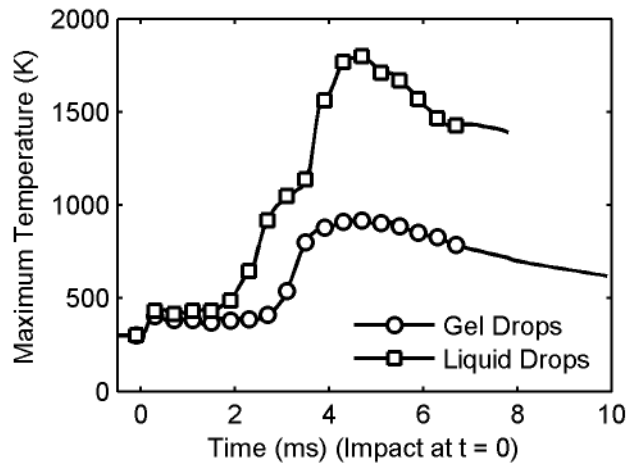
Figure 6-15. Maximum temperature during collision for liquid and gel droplets. Marker spacing matches the image sampling frequency in Figure 6-11 and Figure 6-12.

7. Gelled Droplet Combustion

7.1 Objectives and Approach

The overall goal of this task was to understand the effects of gels on drop burning, and then to evaluate and improve drop burning models for gelled propellants. Specific objectives included design of an experiment to measure drop burning rates, measurement of gelled fuel drop burning rates in an oxidizing environment, and comparison to the classical d-squared burning laws. Additionally the effects of dilution on the ignition of neat MMH drops and its dual flame front were measured. Multiple conference papers and three journal articles resulted from this work.

The journal articles are:
1. Solomon, Y., DeFini, S., Pourpoint, T., and Anderson, W., "Gelled Monomethyl Hypergolic Droplet Investigation," *Journal of Propulsion and Power*, Vol. 29, No 1 (2013), pp. 79-86.
2. Cho, K. Y., Pourpoint, T. L., Son, S. F., and Lucht, R. P. "Microexplosion Investigation of Monomethylhydrazine Gelled Droplet with OH Planar Laser-Induced Fluorescence," *Journal of Propulsion and Power*, Vol. 29, No 6 (2013), pp. 1303-1310.   DOI: 10.2514/1.b34853
3. Cho, K. Y., Satija, A., Pourpoint, T. L., Son, S. F., and Lucht, R. P. "High-repetition-rate three-dimensional OH imaging using scanned planar laser-induced fluorescence system for multiphase combustion," *Applied Optics,* Vol. 53, No. 3 (2014), pp. 316-326. DOI: 10.1364/ao.53.000316

7.2 Approach

The experimental apparatus built in Fig. 7-1 was designed and built to measure the ignition and burning rate of MMH drops in an NTO environment. Necessary procedures for experimentally studying gelled drops under static and convective conditions, and non-reacting and reacting conditions were developed. Specific tasks included the evaluation of means to make and hold drops, the development of a hot gas supply, development of methods for measuring drop size and image analysis, selection of a drop burning model to serve as a baseline, and a repeatable method using an acoustic mixer to gel propellants and measure their viscosity was developed. A rheometer was used to measure the viscosity of samples used in the drop experiments. An experimental approach using a drop on a wire was developed for measuring drop size and temperature history under burning conditions, and a complete set of data on JP-8 drops and MMH drops gelled with silica and HPC were obtained.

The experiment was designed to provide a controlled environment of gaseous nitrogen dioxide (NO_2) around a gelled MMH drop. The system was designed to operate over a range of pressures

from approximately 0.5 bar up to 13 bar at temperatures up to 160ºC. There are three main parts in the system: a) a loading cylinder that controls the chamber pressure, enabling accurate and safe loading of the NTO; b) an evaporation tank in which the oxidizer is vaporized and its temperature is conditioned; and c) a windowed combustion chamber enabling the application of a wide variety of measurement techniques, including high-speed imaging, infrared imaging, and laser diagnostic techniques. Optical access is provided by four windows with a diameter of 38 mm and eight optional 6.8 mm ports for light sources and other measuring instruments. The droplet is hung from a Pyrex rod that minimizes the thermal conductivity to the droplet during combustion. To prevent early hypergolic ignition, the droplet is sealed inside a translating shield tube that traps a small pocket of nitrogen around the droplet.

During an experiment NTO is first chilled below its boiling point of 21ºC at atmospheric pressure. A known weight of liquid NTO is loaded into the loading tube and from this weight the experimental pressure is calculated. The loading tube is connected to the evaporation tank and the liquid NTO is allowed to flow into the tank. The evaporation tank is emptied of air and pre-heated to 100ºC so the liquid can boil and form an environment of high pressure gaseous NTO. Air is evacuated from the combustion chamber and the gaseous NTO enters. After a waiting period of 30 seconds designed to relax the turbulence in the chamber, the protecting piston is removed and the MMH droplet is exposed to the NTO. Images of the burning drops are recorded with a high-speed Phantom camera at a frame rate of 1000 frame/s.
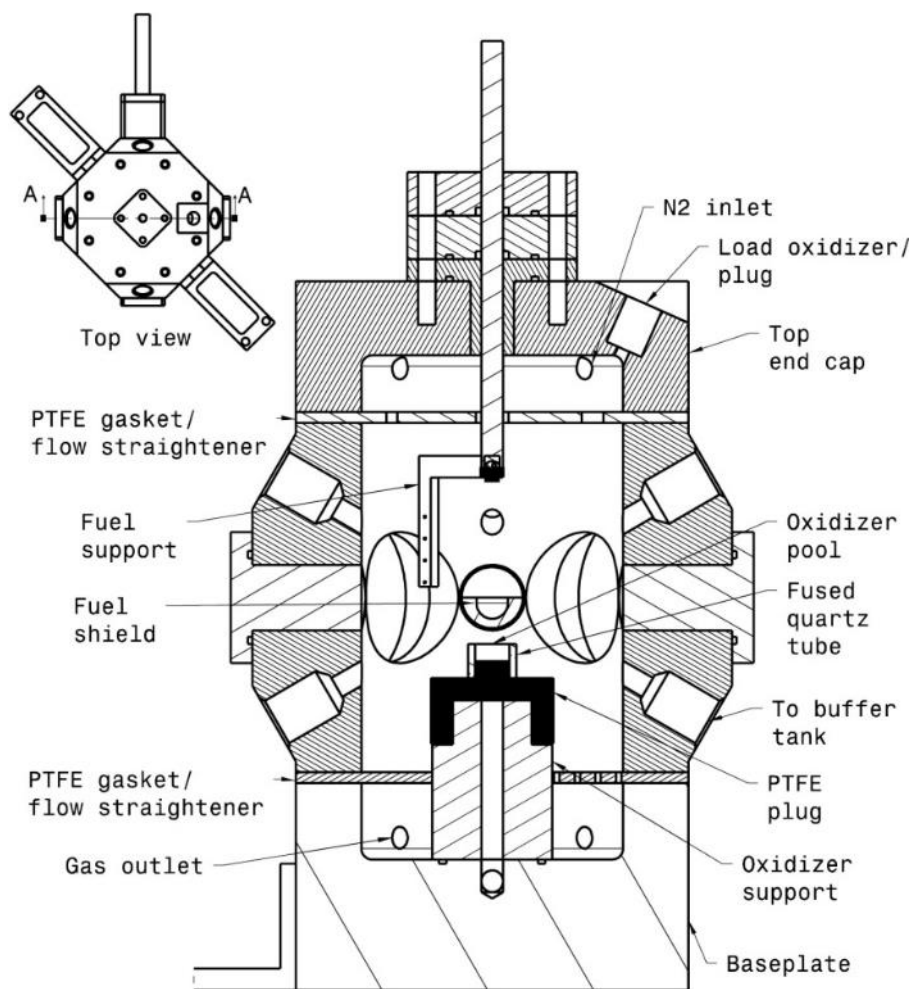
Figure 7-1. Combustor apparatus for measuring ignition and burning rate of a MMH drop in an NTO environment.

7.3 Results

7.3.1 The combustion process of a gel droplet: Diameter & time

During the combustion of an MMH/HPC gel several interesting phenomena can be seen. Bubbles form inside the droplet. Those bubbles cause the droplet volume to grow until the bubbles burst and a jet of fuel is injected from the droplet. Fig. 7-2 shows the process. The formation of the droplet can be seen in frames 1-3. The bubble collapses in frame 4 and the fuel jet is forming and consumed. In addition a double flame can be seen. This process repeats itself during all the combustion period of the droplet.
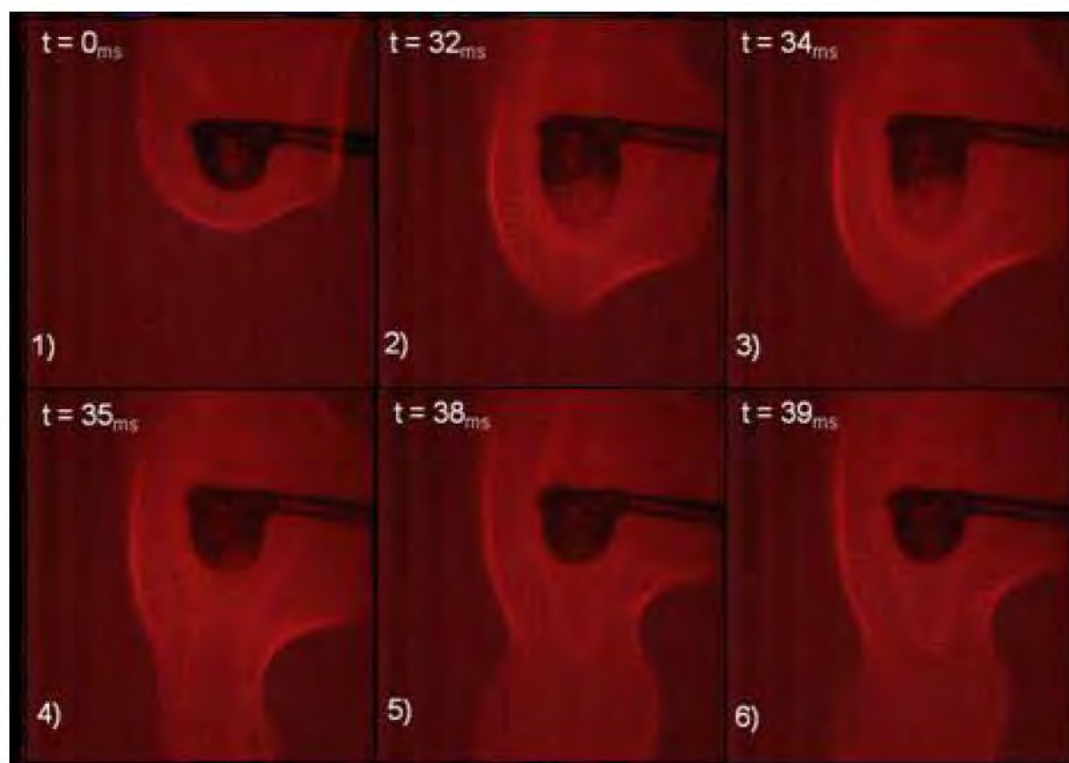
Figure 7-2: Bubble formation and fuel jetting in MMH gel combustion.

The size history of a representative droplet is shown in Fig. 7-3. Near the end of the combustion all the MMH is consumed and only the HPC is burning. The flame is changing from a double flame to a bright yellow diffusive flame.

Figure 7-3: MMH gel with 3% HPC combustion history.
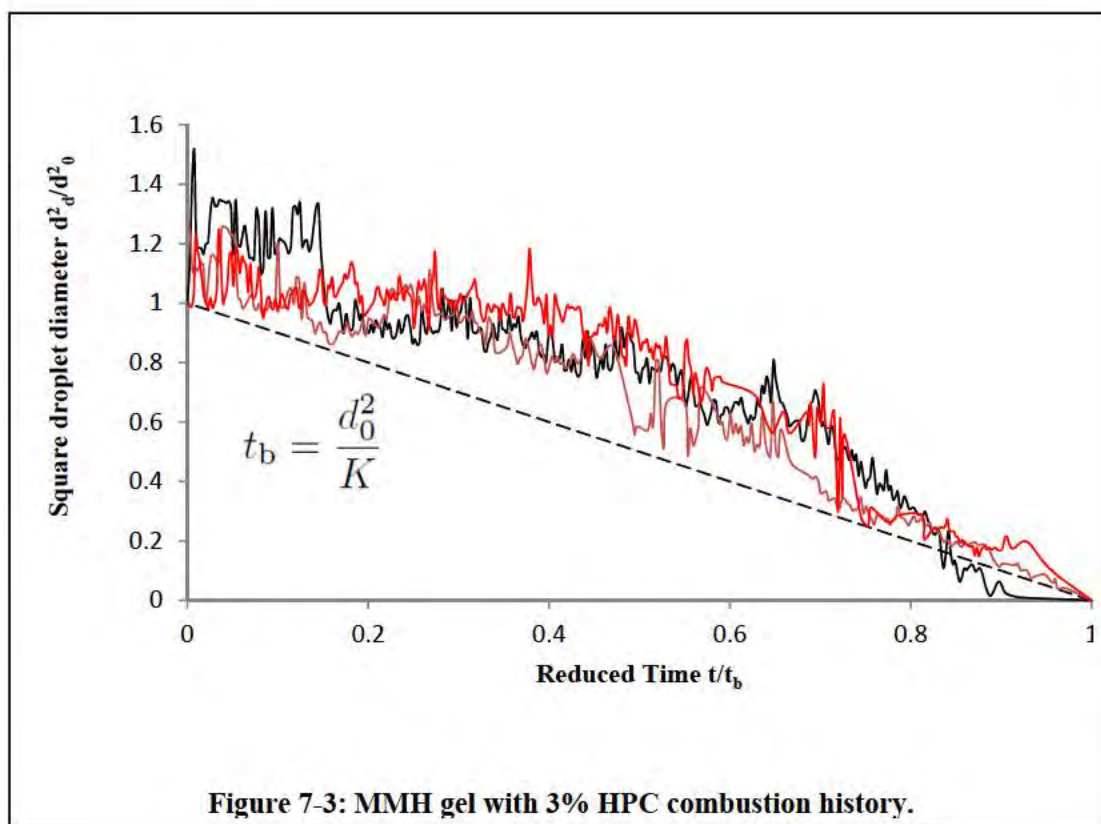
7.3.2. Burning rate as a function of droplet diameter and pressure

Gels with 3 wt.% HPC were tested in a range of droplet diameters from 1.8 to 3.2 mm. The droplet was tested in two ambient pressures, 1.72 bar and 2.89 bar. The burning rate discussed herein, K, is calculated as the square of the initial droplet diameter divided by the total burning time. As can be seen on Figure 7-4 there is a dependency between the droplet diameter and the burning rate. The result that bigger droplets have higher burning rates than small droplets is different than what can be seen in liquids where there is no size dependency. This result was similar to data from the literature for liquid MMH. Whereas there is no apparent dependency on pressure over the limited range tested, it is possible that increasing the pressures range of the experiment will eventually show a relation.

Figure 7-4: Burning rate of MMH gel with 3% HPC.
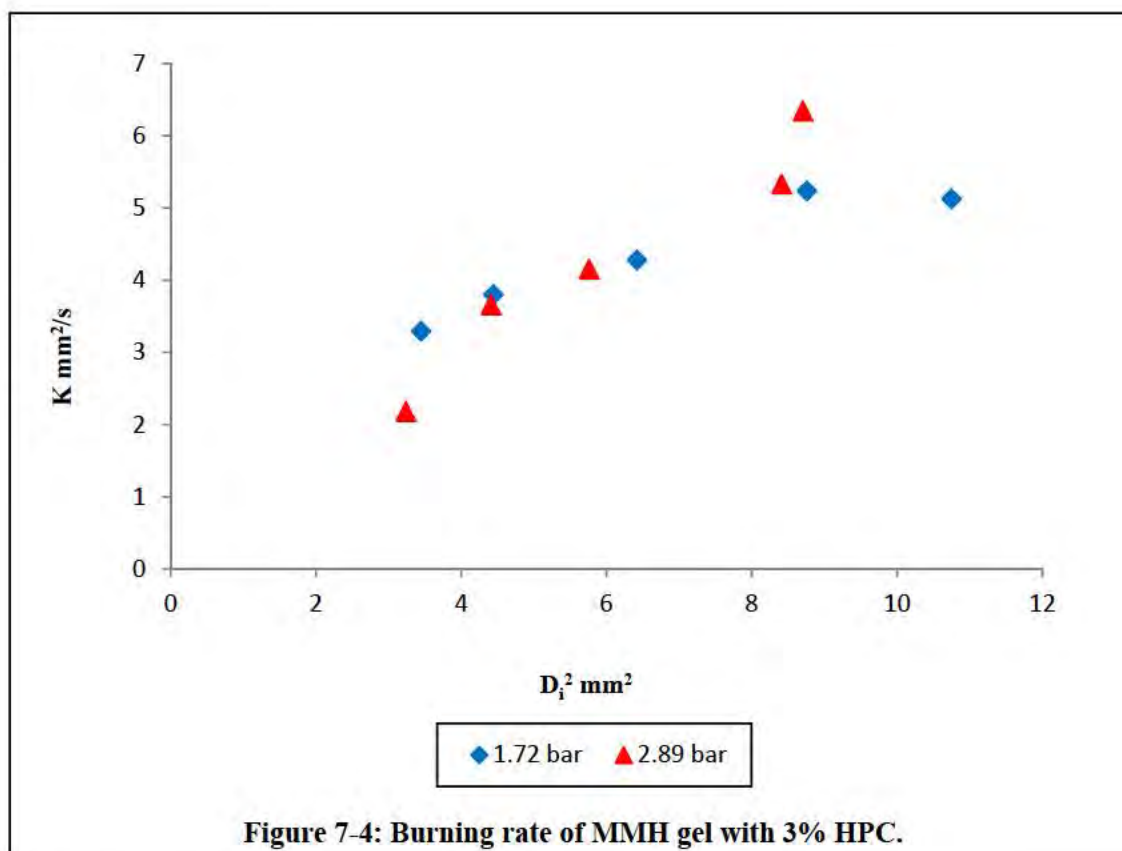
7.3.3. The influence of the gelling agent kind on the combustion pattern

The MMH/Nano-Silica gel burns with an organized, spherical flame front as in liquid droplet combustion as seen in Fig. 7-5a. During the combustion several small "explosions" occurred that threw agglomerates of silica from the droplet, Fig. 7-5b. This process is similar to slurry combustion where bubbles are formed inside the droplet and cause micro-explosions. Near the end of the combustion the droplet loses its mechanical strength and breaks or falls from the droplet holder. Fig. 7-5c shows a burning fragment during the final stages of the combustion. It seems that the MMH serves as a bonding agent for the silica particles and when it is consumed the droplet break and falls. The combustion history of a representative droplet is shown in Fig. 7-6. There is only a small change in the measured droplet volume during the combustion which is probably not representative of the MMH volume, *per se,* but rather the size of the silica structure.
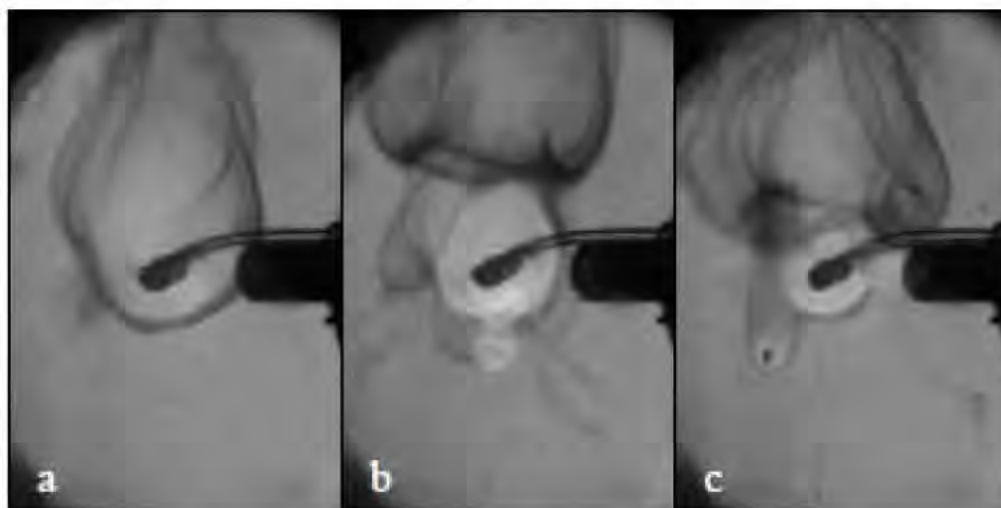
Figure 7-5: combustion of MMH/Nano-Silica gel
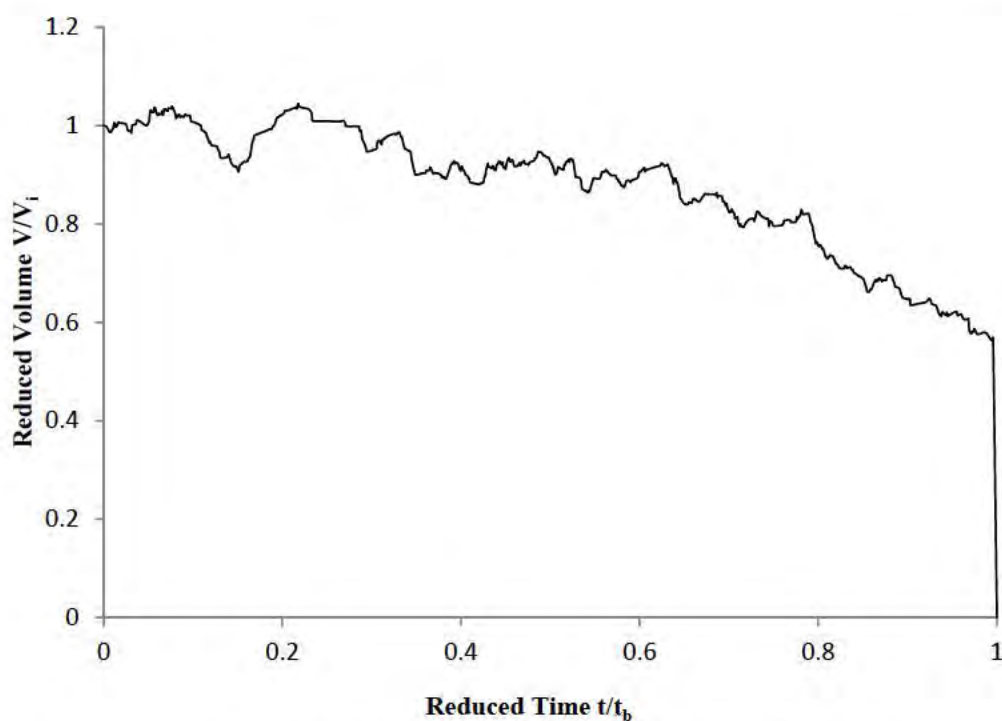
Figure 7-6: Size history of MMH gel with 3% HPC.

At the beginning of the burning process, the droplet gelled with HPC is a fairly homogeneous, highly viscous gel. Figure represents a sector of the droplet with the blue area representing liquid

MMH with a network of HPC polymer chain, represented by the orange lines. The droplet temperature is assumed to be determined by the MMH boiling temperatures of 87ºC at atmospheric pressure or 122°C at a pressure of 2.89 bar. This temperature is lower than the evaporation/decomposition of the HPC polymer and it remains dissolved in the MMH. As the MMH evaporates from the outer part of the droplet, the HPC concentration increases near the surface. Because of the high viscosity it is assumed that gellant concentration gradients do not force mixing that would reduce the gellant concentration. As the MMH evaporates, the homogeneity of the droplet is not maintained and a layer of HPC is formed. Fig. 7-7b illustrates the formation of the HPC layer from the polymer chains that were previously dissolved in the gel while the MMH is evaporating (represented by the blue lines).

As the droplet burns, a fairly impervious HPC layer forms on the droplet surface. At this point an MMH vapor bubble forms inside the droplet (represented in dark blue in Fig. 7-7c. The bubble heats and expands, and the surface is stretched until it is ruptured. A presumed superheated jet of vapor is then ejected from the droplet.

A)   B)   C)
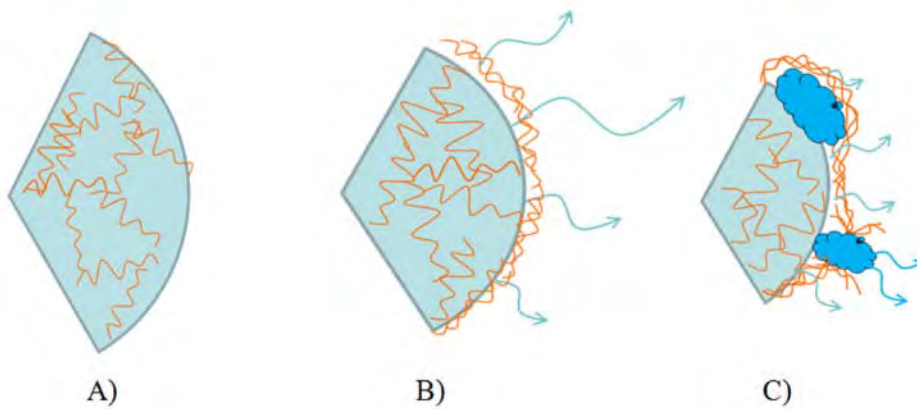
Figure 7-7: Bubble formation inside a burning MMH/HPC gel droplet

As a result of the layer formation and the fuel jetting, the droplet combustion is influenced as follows:

- There is no steady flame front around the droplet. The environment surrounding the droplet is highly convective: the high-speed jets inject fuel from the droplet and disturb the oxidizer environment.

- The swelling of the bubble can move the HPC layer closer to the inner flame front. The droplet temperature will have less influence on the HPC and the thin layer might start to evaporate or decompose.

The resistance of the layer to vapor outflow can increase the pressure inside the droplet, leading to a higher MMH saturation temperature and to flow of gel through weak points in the shell that distorts the droplet shape.

7.3.4. The influence of dilution upon the dual flame front and ignition

An investigation into the effects of dilution upon the dual flame front and ignition of gelled MMH was conducted. Nitrogen, a primary component of both MMH decomposition and MMH/NTO reaction products, was used to dilute an environment of gaseous NTO. The partial pressures of these gases were controlled to maintain a net pressure of 2.9 bar (42 psia). Single droplets of gelled MMH were placed in varying dilutions of this atmosphere, and the subsequent combustion was recorded with a high-speed Phantom camera at a rate of 750 frame/s.

Liquid MMH was gelled with HPC at a concentration of 3% by weight, since there are much data in the Gelled Propellants Lab that have been taken with MMH/3%HPC at 2.9 bar; comparison with other data is thus much easier. The initial test matrix included experiments at 0%, 25%, 50%, and 75% dilution partial pressures. The diluent was then increased in increments of 5% until an ignition limit was observed, with data taken at another 5% beyond that. Diluent pressure percentages were challenging to precisely meet, due to the unpredictability of evaporated NTO final pressures. Noticeable changes in the flame structure occurred in the 70-85% diluent range; therefore, more experiments were performed there.

Droplet and flame front radius histories were extracted from the high-speed movies. Asphericity and jetting due to propellant vaporization inside the drop are the major impediments to obtaining these histories; there are not single quantities that may be used as radii. A MATLAB code was written to extrapolate the lower parts of the flame to spheres, and also to take multiple histories at certain points about the flame.

Thirty-nine experiments were performed within a range of 0.55 bar (8 psi) about the target pressure of 2.9 bar (42 psia). Other studies in the Gelled Propellants Lab have shown that pressure variation in this region has little to no effect on gelled MMH droplet burning rate. An ignition map for the experiments performed is presented below in Fig. 7-8. As can be seen, a mixture of ~85% N_2/15% NTO by pressure is the hypergolic ignition limit for gelled MMH/3% HPC droplets at 2.9 bar. Higher partial pressures of nitrogen result in non-ignition. The position of the inner flame relative to the outer flame stays constant until dilution reaches 60 or 65% N_2. It then moves toward the outer flame until only a single flame is visible at dilutions near 85% N_2. In undiluted oxidizer, the flame thickness history trends of gelled MMH are similar to those of liquid hydrazine.

There is some debate as to whether the flame fronts observed about a burning MMH droplet are true flame fronts, or simply areas of light produced by reaction intermediaries. The existence of

two flame fronts is not disputed; however, their visibility is. Historically, models such as C.B. Allison's have assumed infinitely thin flame fronts. Hersh probed hydrazine flame fronts and found that temperature peaks did not correspond with the visible inner flame front. If MMH decomposition kinetics are slow, this might explain Hersh's observations. The movement of the inner flame front might be seen as the response of chemical kinetics to diluent concentration.
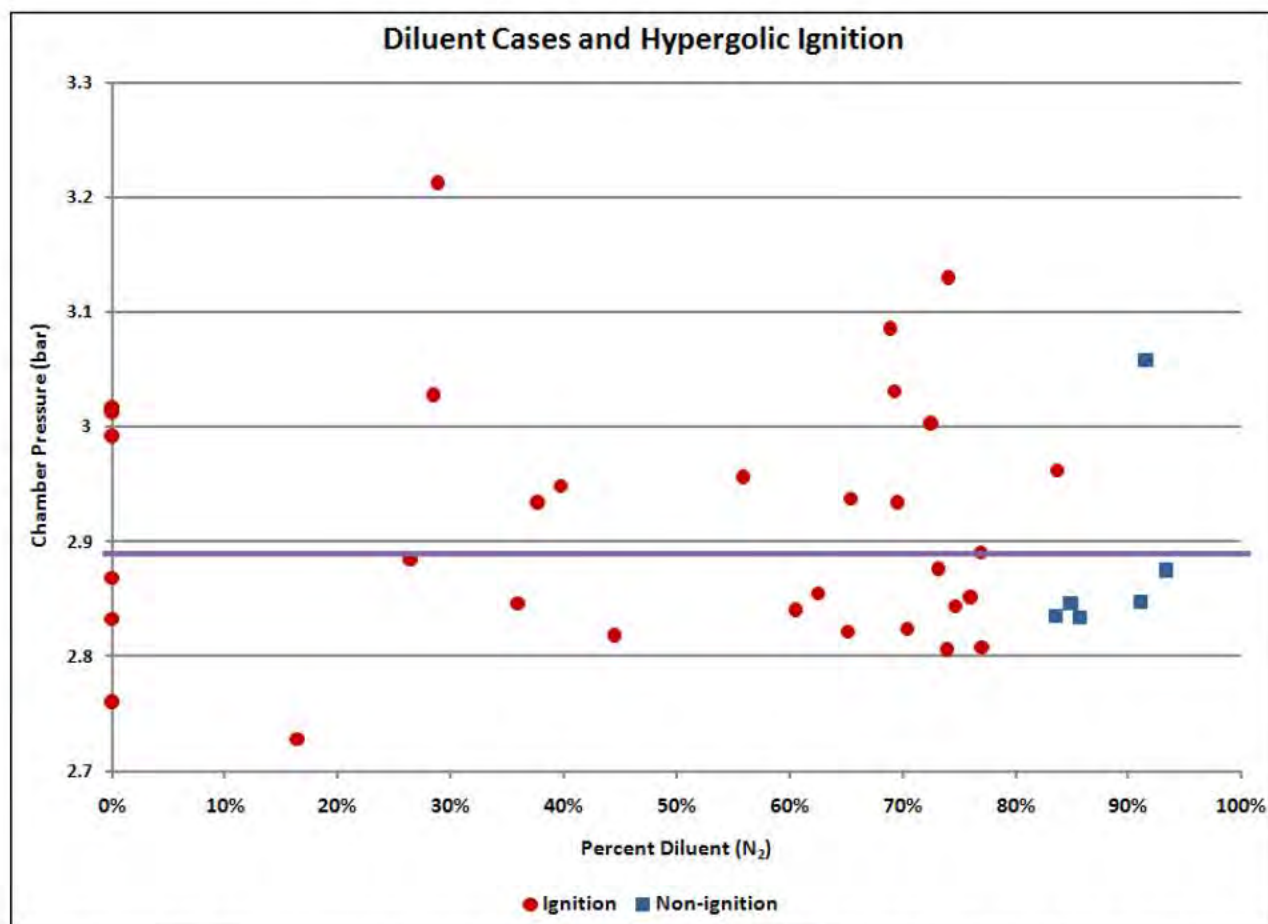
Figure 7-8. Hypergolic ignition for gelled MMH in diluted NTO. The ignition limit in this pressure range is 85% N_2/15% NTO.

7.4 Laser Imaging of Gelled Droplet Combustion

7.4.1 Single-Plane OH PLIF Imaging of Gelled Droplet Combustion

High-repetition-rate OH planar laser induced fluorescence (PLIF) was used to investigate the combustion of gelled and liquid propellants. The experimental system is shown in Fig. 7-9. Framing rates of 5 kHz and 10 kHz were used for different experiments. MMH was gelled with organic gellant HPC at 3 wt.% and 6 wt.%, and burned in air at 35, 103, 172, 276, and 414 kPa. These gelled droplets exhibited significant fuel jetting. The speeds and locations of fuel jets ejected from the burning gelled droplets were quantified for the first time. Different types of interaction of vapor jets and flame front were distinguished, including disruption of the surrounding flame front, extinction of the surrounding flame front (front breakage), and breaking of the flame front and formation of flame balls outside the flame front. Fig. 7-10 shows a sequence of images showing flame extinction as a result of a jetting event. By analyzing the jet speed statistics, it was concluded that pressure and jet speed had an inverse relationship and gellant concentration and jet speed had a direct relationship. This work provided fundamental insight into the physics of gelled fuel droplet combustion.
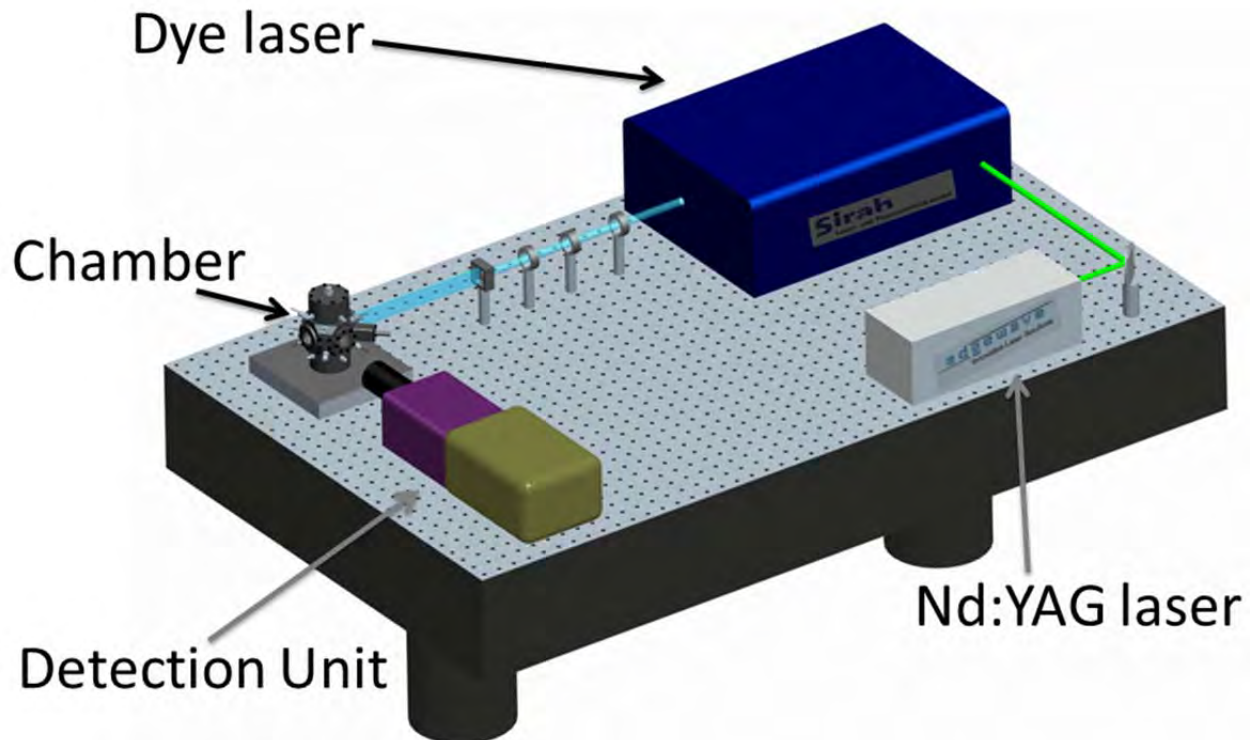
Figure 7-9. Experimental system for high-speed OH PLIF imaging of droplet combustion.
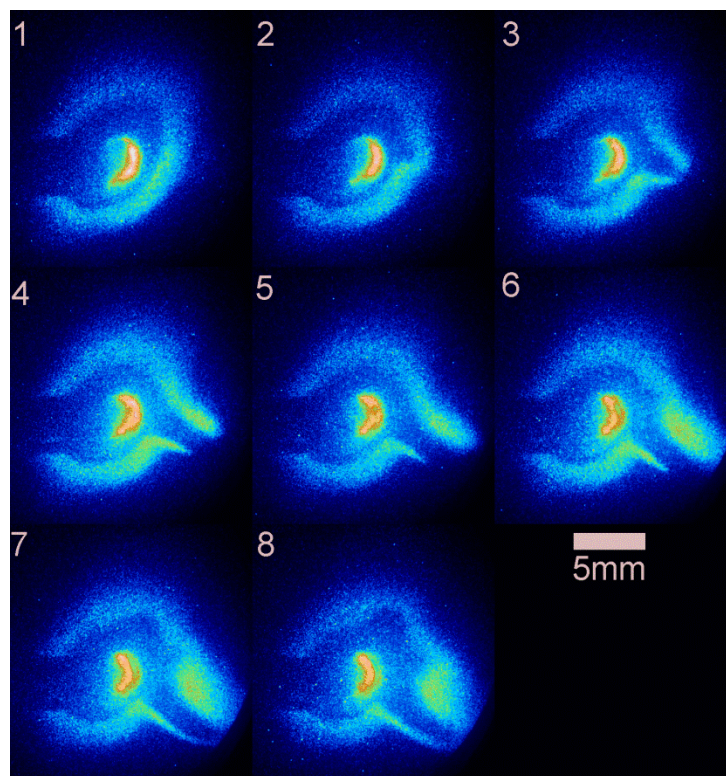
Figure 7-10. OH PLIF images of 6 wt.% HPC MMH gel during a jetting event. The images were acquired at a framing rate of 5 kHz, and the time interval between the images was 0.4 ms.

7.4.2 Three-Dimensional OH PLIF Imaging of Gelled Droplet Combustion

A three-dimensional OH PLIF system incorporating a fast-scanning optogalvanic mirror was designed, assembled, and demonstrated. The system was operated at repetition rates of up to 10 kHz. A schematic diagram of the system is shown in Fig. 7-11. These experiments were among the first demonstrations of the three-dimensional imaging of at framing rates of 1 kHz. A three-dimensional scan time of 1 ms was achieved, with ten slices generated per sweep. The system was applied to 3 wt.% and 6 wt.% HPC methanol gelled droplet combustion at 100 kPa. The system had sufficient spatial and temporal resolution to provide a more complete picture of the complex asymmetrical and random flame structure of the gelled droplet combustion. The results of such a three-dimensional scan are shown in Fig. 7-12, where a three-dimensional image of a jetting event with flame front breakage and the formation of a flame ball outside the flame front is displayed.
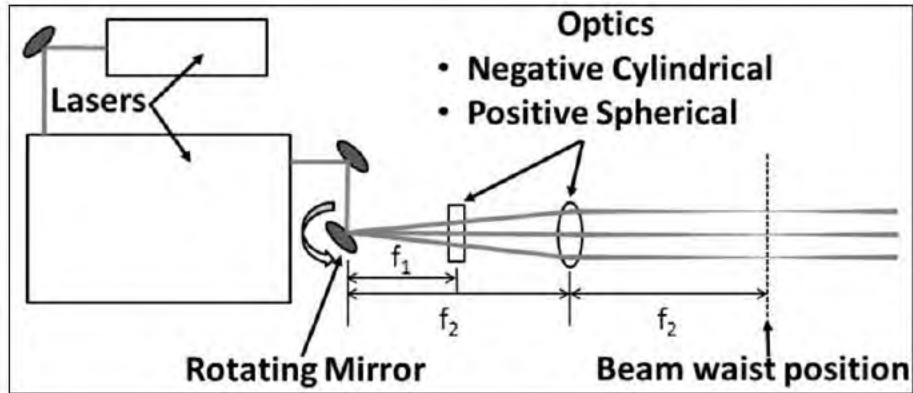
Figure 7-11. Schematic diagram of the scanning optogalvanic mirror system used for the three-dimensional OH PLIF imaging experiments.
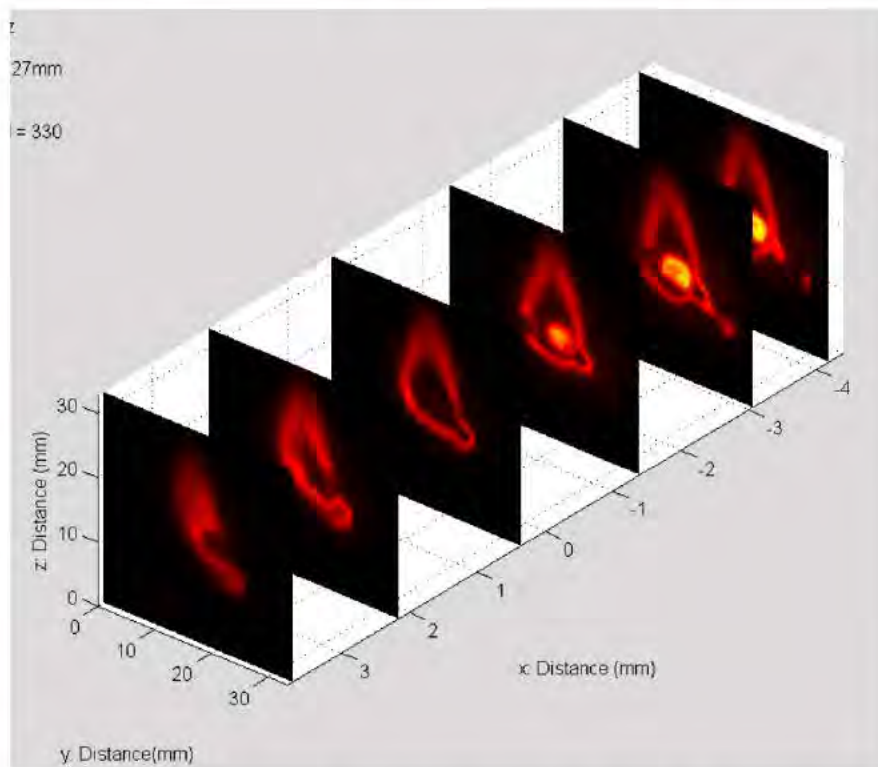
Figure 7-12. Schematic diagram of the scanning optogalvanic mirror system used for the three-dimensional OH PLIF imaging experiments.

7.4.3 Laser Imaging of Liquid MMH Droplet Combustion

The combustion of liquid MMH droplets burning in mixture of N_2O and N_2 was investigated using the 5 kHz OH PLIF system and a visible imaging system. The time history of the OH

profile and the droplet diameter during the process were measured. Experiments were conducted for N_2O mole fractions of 0.2 and 0.4, and for total pressures of 103, 172, 276, 414, and 552 kPa. Analysis of the OH PLIF and visible flame images showed that the oxidation flame front is located between the visible dual flame fronts. The results showed a thicker flame sheet and higher burning rate for increased N_2O concentration at a given pressure. The burning rate increased with increased pressure for 0.2 mole fraction N_2O, but the burning rate decreased with increased pressure for 0.4 mole fraction N_2O. This work provides valuable experimental data for validating numerical models of droplet combustion with detailed chemical kinetics submodels.

2 mm
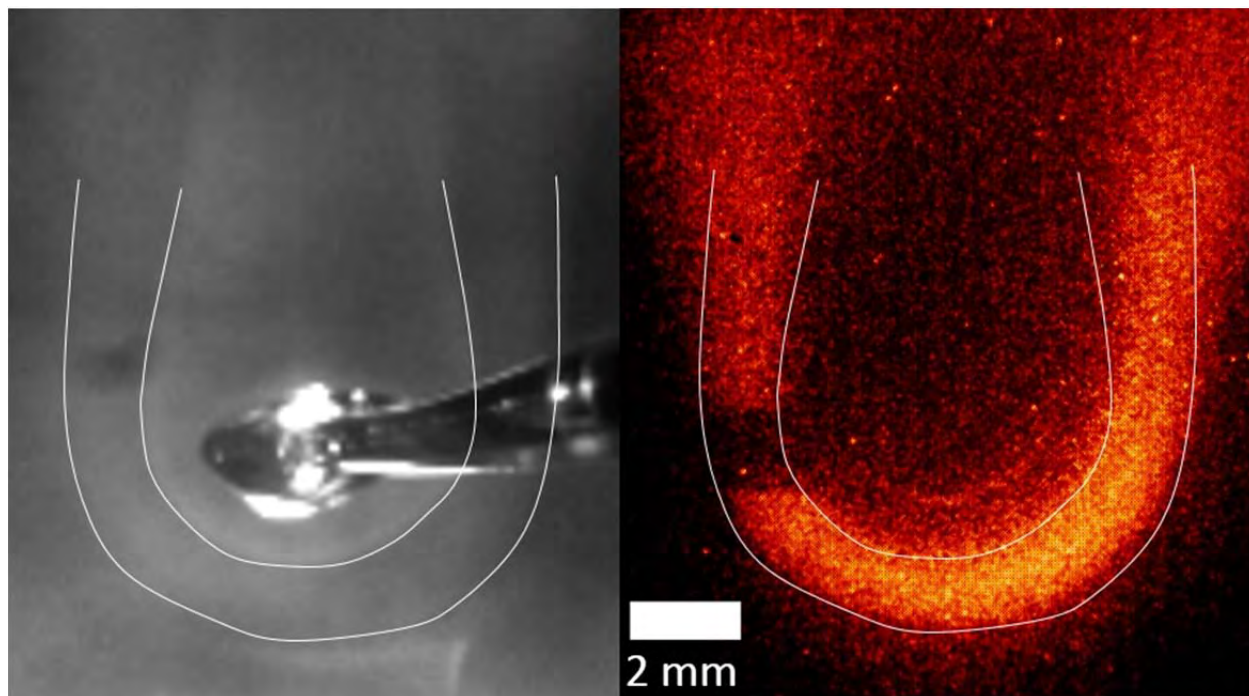
8.0 Reaction Kinetics: Multiphase Mechanism Development for Hypergolic Mixtures

8.1 Objective and Motivation

Elementary hypergolic and reduced mechanisms were developed and evaluated for MMH/RFNA, along with mechanisms and rate expressions for TMEDA and DMAZ hypergolic chemistry. These reaction sets were created primarily for application in propulsion design but also for insights into the reaction pathways, for interpretation of the project's data, and for capstone-application modeling, where reduced-kinetics sets are more suitable for reactive CFD modeling. It was accomplished by interactions with Army Research Laboratory researchers and by our own independent quantum-chemistry and reaction-theory calculations. Mechanisms were tested and refined using data for temperature rise and using NH_3, NO_2, and morpholine-containing flames.

Prior to this study, the principal developments of detailed hypergolic mechanisms were for MMH/HNO$_3$ by Catoire et al.[51] and for MMH/RFNA by Anderson and co-workers. The latter work was unpublished and the ARL expectation was that it would need to stay so. Anderson had constructed his gas-kinetics set carefully using available literature data plus an N$_2$O$_4$ decomposition rate to increase heat release, tuned parametrically until it reached the right ignition behavior. Nusca had tested an ARL reduced-size set, based on this full set, in a combustor model.

8.2 Approach

The task was originally formulated based on the hypothesis that three situations contributed to the hypergolic system's reaction kinetics, distinguished by the phases involved:

- *Liquid-liquid reaction*. Reaction was expected to be almost instantaneous upon contact of the fuel and oxidizer liquids because of fast acid-base chemistry and to be quite exothermic. The plan was to treat liquid-liquid (and gel-gel) reaction as stoichiometric consumption of the reactants up to the point that enough heat was released to vaporize the liquids completely.

- *Droplet-vapor kinetics.* Fuel-oxidizer reaction kinetics at the liquid-vapor interface again was expected to be nearly instantaneous, but a finite reaction rate for the process would be set by the maximum rate of mass transfer. Stoichiometry was to be estimated.

- *Homogeneous vapor-phase chemistry.* This set is classical combustion chemistry except for being O$_2$-free. It includes chain-branching ignition and chain propagation, releasing heat and evolving combustion gases. An improved reaction set was to constructed usinf new or improved kinetics from the literature and our quantum-chemical modelling.

The second part of the study was to reduce the gas-kinetics reaction set by modeling a variety of flames and identifying reactions to be omitted that would have minimal impact on the results. The resulting reduced set was to be used by ARL modelers, and our kinetics research would move on to model other hypergolic fuels.

8.3 Results and Contribution to the State of Knowledge

The results developed naturally from the plan above, leading to a full model with many elements of the original plan. One change was that by the time of the MURI kick-off meeting, internal ARL review had led to the decision to release the detailed ARL mechanism for MMH/RFNA publicly (Anderson et al.[52]) although not the corresponding reduced mechanism. Thus, a new gas-phase mechanism did not have to be built from scratch.

The plan's hypotheses were largely borne out, along with some instructive surprises. First, our mechanism-reduction approach of achieving a minimum number of essential elementary reactions proved effective and should be more extensible than composite-reaction approaches. Second, rapid gas generation on liquid-liquid contact was shown in the CFD parts of the two Hypergolics MURIs to disrupt the droplets and disperse them as aerosols, much as in our original proposal. Third, the Pourpoint group and we built a successful model for droplet ignition and hypergolic combustion our reduced gas-phase set and on findings from the MURI groups of

Thynell and Goddard. They found indications that the gas+aerosol chemistry was crucial for raising the temperature to ignition. We developed effective stoichiometry and mass-transfer-limited kinetics, which was supported by the Pourpoint group's successful CFD modeling.
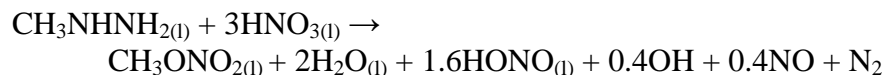
8.3.1 Liquid-liquid reactions

The rapid gas generation on liquid-liquid contact, part of our original hypothesis, was shown in the CFD parts of the MURI to disrupt the droplets and disperse them as aerosols. In the present work, we use an updated set of liquid-liquid and vapor-liquid reactions based on experimental observations of the pre-ignition behavior of MMH and nitric acid. The coupling between the liquid-phase reactions and the presence or absence of ignition has been discussed in recent publications of experimental work in this area.[53,54,55] It has been established that the formation of an aerosol compound of MMH and nitric acid along with formation of key intermediate species (CH_3ONO_2 and HONO, for example) provides a pathway to gas-phase ignition. However, the effect of the extremely rapid heating due to the acid-base reaction between MMH and HNO_3 and the explosive vaporization phenomenon observed in water suggests two possible routes to ignition.

Our original hypothesis, a one-step liquid reaction mechanism generating heat, was used in the CFD implementation of these mechanisms. It immediately produces gas and rapidly forms a vapor layer along the liquid interface. The interface region then consists of a mixture of vaporized propellants and intermediate species produced by the liquid reaction, and its temperature is near the propellant boiling point of the more volatile liquid (*ca.* 360-400 K). At these temperatures, the thermal decomposition of the propellants and intermediates is limited, and the dominant reaction is the H-abstraction of MMH by radicals (predominantly OH and NO_2) and the previously mentioned aerosol formation.

On the other hand, if the liquid reaction is treated as a series of finite-rate steps that do not immediately produce gas at the propellant interface, the liquid at the interface can be heated to the homogeneous vapor nucleation temperature rather than the boiling point. At this higher temperature (*ca.* 500 K), the thermal decomposition of nitric acid and methyl nitrate would become more significant, providing an additional source of radicals for H-abstraction from MMH.

In the present work [55,56], we focused on the one-step liquid reaction approach following one of the proposed pathways by Wang and Thynell[54]. However, based on the observations from the dominant reactions in the multi-step approach and some initial CFD results that did not result in ignition, we used an overall liquid reaction that produces a radical-rich product mixture to enhance the subsequent gas-phase reactivity:

$$CH_3NHNH_{2(l)} + 3HNO_{3(l)} \rightarrow$$
$$CH_3ONO_{2(l)} + 2H_2O_{(l)} + 1.6HONO_{(l)} + 0.4OH + 0.4NO + N_2$$

The activation energy for this reaction was set as 5.9 kcal/mol, which is consistent with the measurements by Smith[56], Catoire et al.[51], and Seamans et al.[57] for similar conditions. The rate constant was set to 10^{16} (mol-cm^3-s units) to match the experimentally observed vapor formation time of approximately 100 μs by Forness et al.[58].

8.3.2 Droplet-vapor reactions

The rapid gas generation on liquid-liquid contact was shown in the CFD parts of the MURI to disrupt the droplets and disperse them as aerosols. MURI experiments on hypergols have also shown that in certain conditions, an aerosol cloud forms just prior to ignition [54]. Providing the crucial insight, Wang and Thynell[54] theorized that the reactions occurring in this aerosol phase help the system temperature rise from the boiling point of the liquids to the ignition temperature, and that the energy was coming from the ability of the aerosol cloud to turn the gaseous fuel molecules into solvated ions.

Tao[59] determined that the presence of two assisting water molecules is necessary to facilitate proton transfer between nitric acid HNO_3 and ammonia. In the case of the hypergols, the assisting solvent molecules are the propellants themselves, which are forming into small droplets dispersed among the gas phase, so a small complex of one solute molecule surrounded by at least three solvent molecules is necessary to facilitate proton transfer between the solute and one of the solvent molecules. This mechanism allows the gas-phase propellants to absorb into aerosol droplets and form intermediate complexes, which then produce energy by solvating the propellants.

The MURI model[55,56] was developed to help the CFD code simulate the reaction between gaseous MMH and a small liquid HNO_3 (nitric acid) droplet. MMH is the more volatile species, so it was assumed that it would be completely vaporized, while HNO_3 would remain liquid. An analogous analysis can be made for the reaction of $HNO_{3(g)}$ with $MMH_{(l)}$, but only the following representation was used here. It was further assumed that even though the aerosol cloud was not seen in all experiments, this aerosol chemistry was still responsible for heating the system.

A multi-step, elementary-reaction mechanism was developed on that basis:

1. $MMH_{(g)} + HNO_{3(l)} \rightarrow MMH \bullet HNO_{3(l)}$
2. $MMH \bullet HNO_{3(l)} + HNO_{3(l)} \rightarrow MMH \bullet 2HNO_{3(l)}$
3. $MMH \bullet 2HNO_{3(l)} + HNO_{3(l)} \rightarrow MMH \bullet 3HNO_{3(l)}$
4. $MMH \bullet 3HNO_{3(l)} \rightarrow (MMH \bullet H^+)(NO_3^-) \bullet 2HNO_3$
5. $(MMH \bullet H^+)(NO_3^-) \bullet 2HNO_3 + HNO_3 \rightarrow (MMH \bullet H^+)(NO_3^-) \bullet 3HNO_3$

and then these five steps were combined into a single overall absorption reaction:

$$MMH_{(g)} + 4HNO_{3(l)} \rightarrow (MMH \bullet H^+)(NO_3^-) \bullet 3HNO_3$$
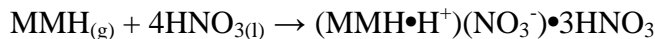
The rate of the overall absorption reaction was assumed to be the rate of mass transfer of the MMH gas to the liquid HNO_3; i.e., MMH gas would react instantly with liquid HNO_3 once they came into contact. The mass transfer rate was calculated using a Lewis number correlation[60]:

$$\frac{h_G}{k_Y c_p} = Le^{0.567} \tag{8.1}$$

where h_G is the heat transfer coefficient of the gas (W/m^2 K), k_Y is the mass transfer coefficient (kg/m^2 s), c_p is the heat capacity (J/kg K), and Le is the Lewis number.

After absorption, the solvated complexes should be stable until they separate and vaporize at near the ignition point. The primary contribution of the aerosol formation reaction to the overall mechanism is the addition of heat in the early reaction stages. For the work presented here, the

subsequent vaporization and reverse of this aerosol formation was not included explicitly. With these parameters set, the reaction rate coefficient for the aerosol formation reaction was determined as $1.42 \cdot 10^5 \, T^{1.861}$ with reaction order of one with respect to HNO_3.

8.3.3 Homogeneous vapor-phase chemistry – Detailed kinetics

A new reaction set was developed to describe gas-phase combustion chemistry of fuels containing only hydrogen, carbon, oxygen, and nitrogen, using it to study combustion of hypergolic monomethyl hydrazine and tetramethylethyldiamine with red fuming nitric acid. Reactions were also developed for DMAZ[61].

H/N/O mechanism. The foundation of the larger mechanism was a new reaction set to describe combustion of ammonia flat flames[57], thus containing only H/N/O chemistry for simplicity. This work and the construction of the mechanism are described in full detail in Chapter 5 of the dissertation of Labbe[75]. Model predictions were compared successfully to data from the work of:

- Bian et al.[62], who mapped a fuel-lean, 35-torr flame of 48% NH_3, 51% O_2, and 1% Ar ($\Phi=0.70$);

- Vandooren et al.[63], who studied a fuel-rich, 54-torr flame of 46.1% NH_3, 47.2% NO, and 6.7% Ar ($\Phi=1.46$);

- Duynslaegher et al.[61], who studied eight different flames of NH_3, H_2, O_2, and 43-48% Ar and at pressures of 50-120 mbar (0.049-0.118 atm);

- Sausa et al.[64], who studied a $\Phi=1.1$ $H_2/N_2O/25\%$ Ar flame at 30 torr and the same flame doped with 4% NH_3; and

- Davidson et al.[65], who pyrolyzed NH_3 in a shock tube using 2200-3300 K, 0.75-1.025 atm, and 1000, 3000, 8000, and 10000 ppm NH_3 in Ar.

H/C/N/O model. The base H/N/O mechanism was expanded to include carbon chemistry and was tested against flames of dimethylamine, ethylamine, and a methane/ammonia mixture (Labbe[75], Ch. 6) and against other literature reaction sets. This reaction set was further tested against fuel-rich flat flames of morpholine[52,62,63] and Labbe[75], Ch. 8), a six-membered ring with both ether and amine functionalities, and of tetrahydropyran[53,58,60] and Labbe[75], Ch. 7), the monoether analogue to cyclohexane and basic ring in cellulose. Experimental concentration data were obtained using both MBMS and chemiluminescence techniques. Also, the model was tested against high-pressure shock-tube studies of morpholine[54] and (Labbe[75], Ch. 9) for both oxidation and pyrolysis at elevated temperatures and pressures, collaboratively within the MURI with the Hanson Group at Stanford.

MMH/RFNA model. A MMH/RFNA reaction set was developed, building from the base H/C/N/O mechanism. Additional reactions for MMH combustion were added along with the kinetics calculated for possible MMH pyrolysis, calculated elsewhere in the MURI by Sun et al.[66]. Details of MMH/RFNA model development and testing are presented in Chapter 10 of Labbe[75].

87

With a proposed RFNA composition of 84% HNO_3, 13% N_2O_4, and 3% H_2O, the overall reaction for stoichiometric MMH / RFNA combustion is:

$$CH_3NHNH_2 + 1.9084 \text{ RFNA} \Leftrightarrow CO_2 + 3.859 \text{ } H_2O + 2.050 \text{ } N_2$$

A skeletal mechanism for MMH was developed (Fig. 8-1), and the thermochemistry and kinetics were adopted from the literature including the ARL set[52] and/or computed with computational quantum chemistry at a CBS-QB3 level in Gaussian 09 [67] and the NIST Chemrate codes.[68] The resulting new set then included 177 species and 1619 reactions.
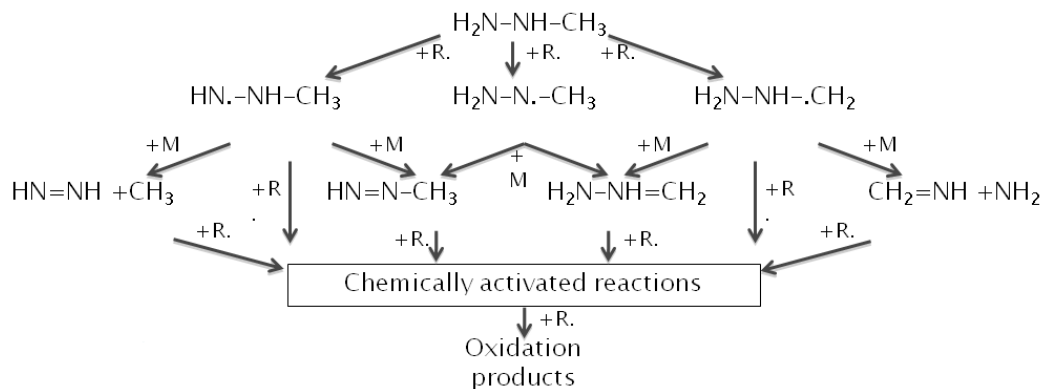
Figure 8-1: Skeletal reaction mechanism for MMH combustion showing possible hydrogen abstraction routes and their subsequent products, used as a basis for developing a new MMH/RFNA reaction set.

Using CSTR calculations performed with Chemkin Pro[69], this set was tested for internal consistency and to identify dominant pathways for further examination. Mixtures from Φ=0.8 to 1.3 were burned in an adiabatic, zero-D, 1-atm constant-pressure, perfectly stirred reactor, starting with an initial temperature of 1000 K. Composition changes during induction were followed by the rapid temperature rise at the time of ignition, shown in Fig. 8-2 to decrease with increasing richness of the mixture.
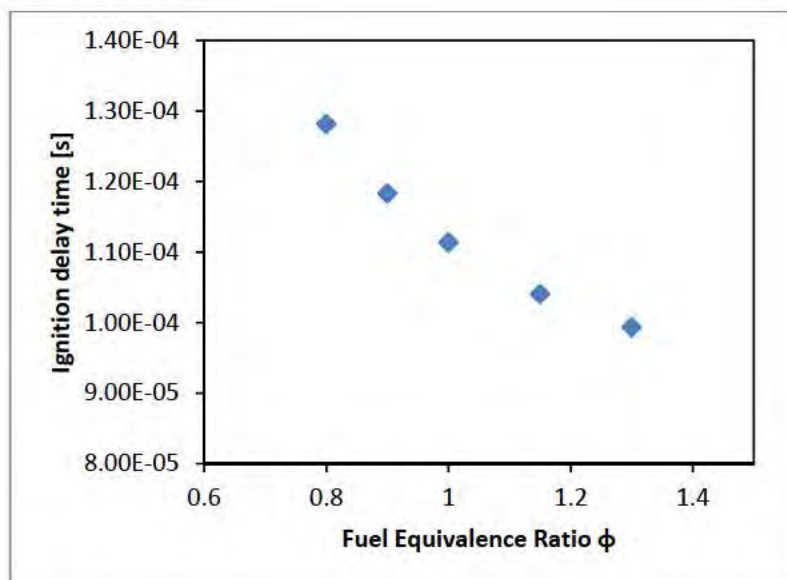
Figure 8-2: Dependence of MMH/RFNA ignition delay times on fuel equivalence ratio.

The results were post-processed as reaction flux diagrams to show the dominant reaction pathway for MMH/RFNA. Analysis of the stoichiometric mixture (Fig. 8-3) reveals that OH and NO_2 are the dominant radicals. Chain-branching is by decomposition of molecules: NO_2 from the rapid decomposition of fed initiator N_2O_4 at low temperatures; then as the system heats up, OH and additional NO_2 from HNO_3 decomposition; and finally OH+NO from HONO decomposition. This behavior is quite different from hydrocarbon and O_2-based combustion, and reactions of O do not contribute, as no O_2 is supplied. Destruction of fuel MMH is very analogous to hydrocarbon consumption, though. MMH is first attacked by a radical, R, to form $CH_3\text{-}N^-\text{-}NH_2$, which is further attacked by another radical to form CH_3NNH. Often the abstraction partner is NO_2, forming HONO. Once formed, HONO then decomposes to form NO and regenerate OH radicals. The CH_3NNH is attacked once again by a radical abstraction partner to form CH_3NN. CH_3NN decomposes into CH_3 and N_2. The methyl radical then undergoes subsequent reactions to form CO.

This mechanism was subsequently used to generate reduced mechanisms, as described in Section 8.3.4.

89
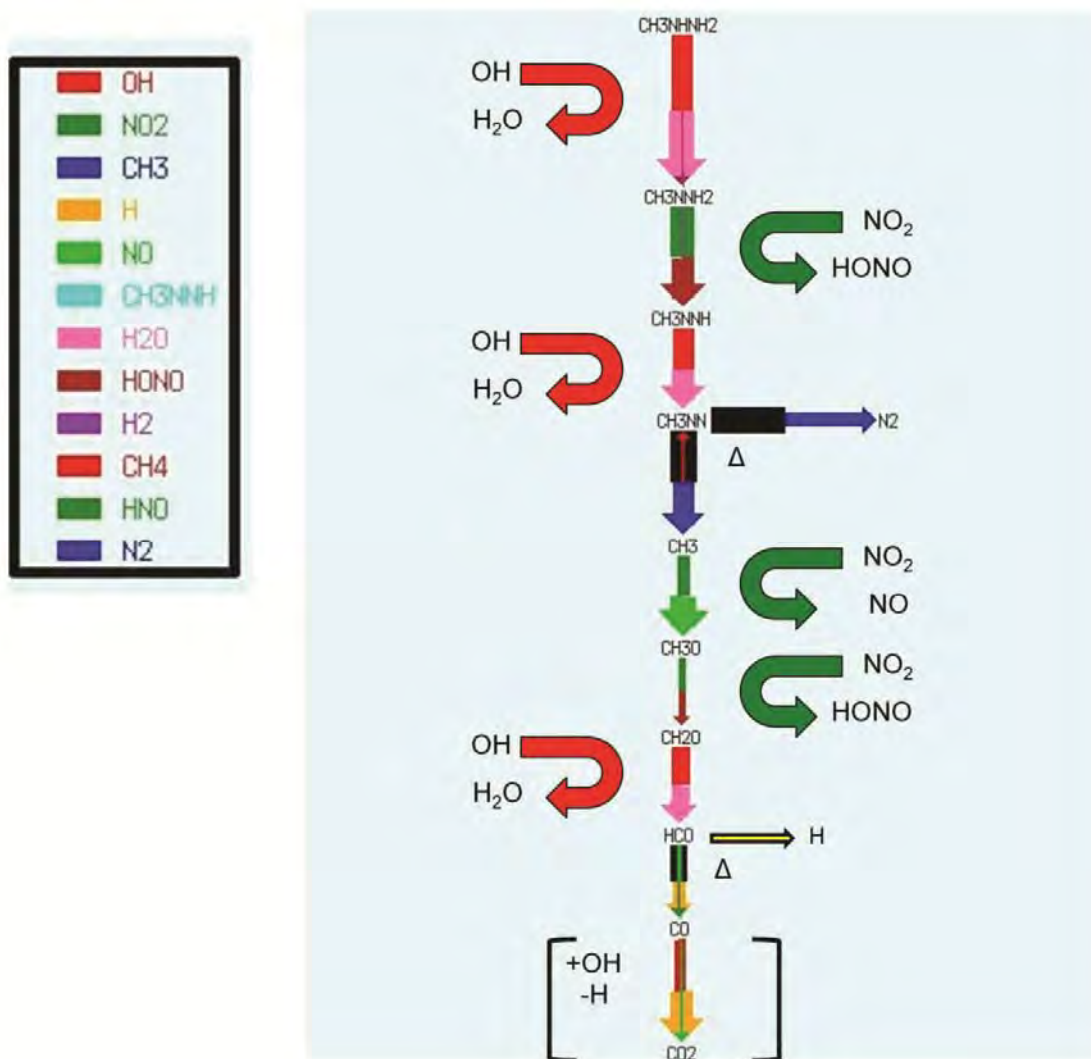
Figure 8-3: Reaction fluxes from stoichiometric MMH/RFNA hypergolic combustion. Arrow tails are colored by the co-reactant, heads are colored by the co-products, and arrow thicknesses correspond to reaction flux on a per-carbon basis.

TMEDA/RFNA model. A skeletal mechanism for TMEDA was developed (Fig. 8-4), and the thermochemistry and kinetics were computed with computational quantum chemistry at a CBS-QB3 level in Gaussian 09 [67], estimations by analogies to 2-methylheptane chemistry, our spreadsheets, and the NIST Chemrate codes [68]. Thermochemistry was calculated for all 21 new TMEDA species in the proposed skeletal mechanism, accounting for hindered rotors. A total of 141 new reaction rates for TMEDA combustion were included in the mechanism. Adding these reactions and species, the TMEDA mechanism has 198 species and 1760 reactions. Additional details are provided in [67,68] and in Chapter 11 and Appendix J of Labbe[75].
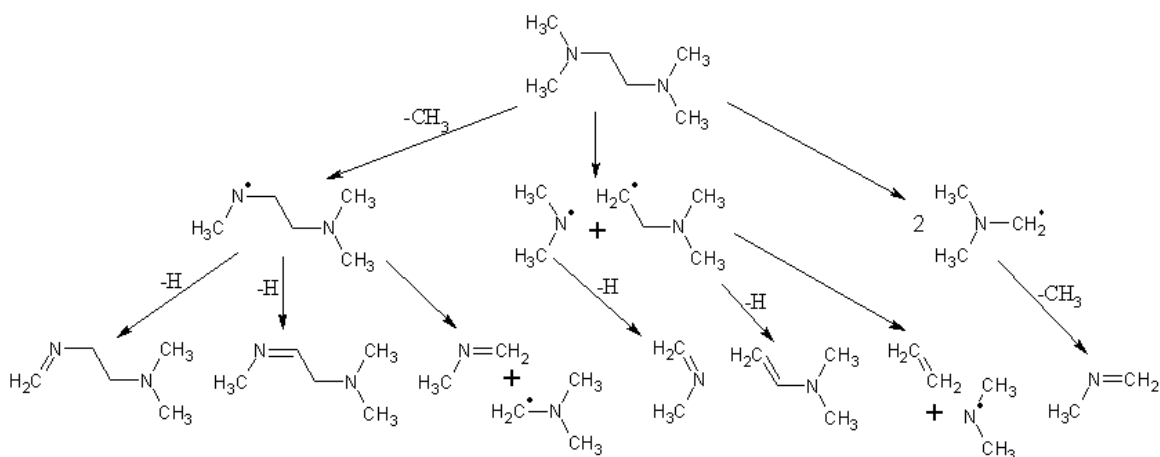
Figure 8-4: Proposed thermal decomposition pathways for TMEDA.

The resulting TMEDA set was tested for internal consistency and to identify dominant pathways for further examination using Chemkin Pro [69] in the same way as for MMH. The model predicted an ignition delay time at these conditions of 233 μs (Fig. 8-5) with temperature ultimately rising to 2756 K. From the model results, dominant reaction pathways could be determined. Primarily, TMEDA first loses a hydrogen atom via abstraction reaction, resulting in one of two different TMEDA radicals. Once a radical is formed, both different TMEDA radicals then preferentially β-scission the C-N bond adjacent to the ethane bridge, forming a three-heavy-atom species (either radical species CH_3-N-CH_3 or CH_3-N=CH_2) and a five-heavy-atom species. The CH_3-N-CH_3 radical then β-scissions a hydrogen to form CH_3-N=CH_2. The five-heavy-atom species, through subsequent reactions, also each form CH_3-N=CH_2 as an eventual product of reaction. Hence, each TMEDA molecule generally produces two CH_3-N=CH_2 molecules, resulting in a large spike in concentration of CH_3-N=CH_2 during reaction.
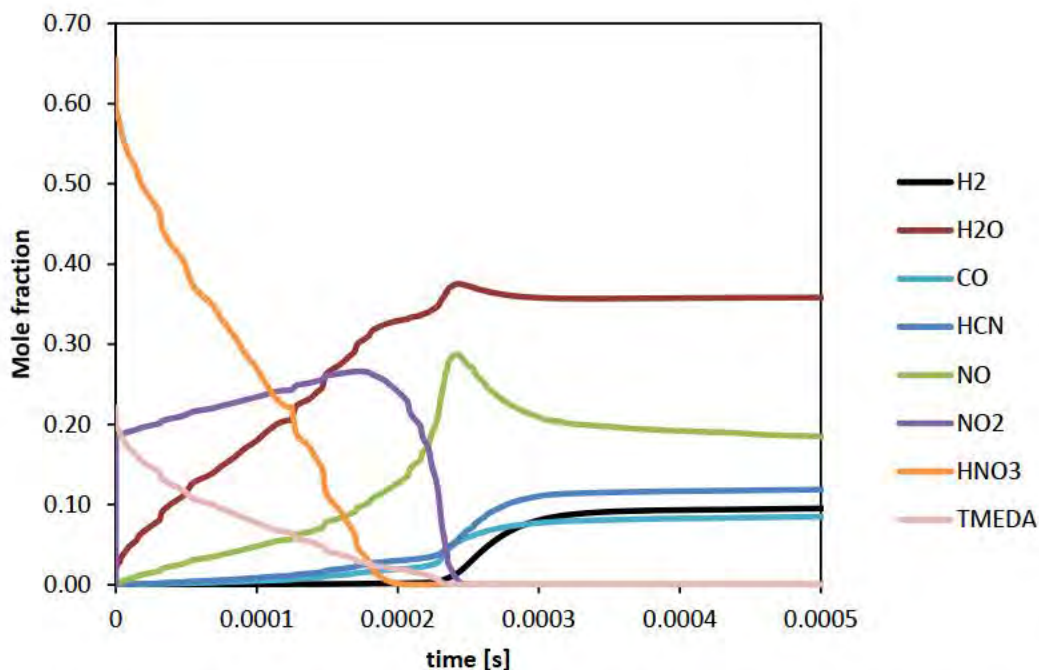
Figure 8-5: Mole fraction profiles for H₂, H₂O, CO, HCN, NO, NO₂, HNO₃ and TMEDA from a 0-D constant-pressure reactor model using a stoichiometric TMEDA/RFNA mixture at P = 1 atm and initial temperature of 1000 K.

8.3.4 Homogeneous vapor-phase chemistry – Reduced kinetics

Reduced-size reaction sets were developed to describe gas-phase combustion chemistry of hypergolic monomethyl hydrazine and tetramethylethyldiamine with red fuming nitric acid. Such reduced reaction sets are needed for affordable CFD calculations of real combustors.

To reduce the reaction set, a rate of production analysis through time was performed for each species included in the model and each reaction rate included in the model for the base-case system (stoichiometric, P = 1 atm). Peak rates of production were summed for every reaction included in the model to determine relative contributions to the overall model. The reactions with minimal contributions were iteratively eliminated until a first reduced reaction set was developed for MMH/RFNA with 87 species and 482 reactions. This reduced reaction set will be referred to as "reduced set 1."

While some CFD models may be able to incorporate such a large model, others need a further reduced model. To eliminate reactions and species further, overall contribution to the model for each species was considered and species were iteratively eliminated to make a further reduced set with 41 species and 200 reactions. This reduced reaction set will be referred to as "reduced set 2." This further reduced set had to eliminate some important chemistry, and performance of reduced set 2 is expected to be inferior to that of reduced set 1. However, given computational constraints of some CFD codes, the second set should give a good estimate. These two sets both contain only elementary-reaction rate constants. Further reduction could be achieved through the introduction of composite rate constants.

Adiabatic CSTR calculations were used to test the sets. Reduced set 1 predictions are indistinguishable from that of the full set, while reduced set 2 performs similarly, but more slowly than what is observed in the full set. Specifically, the ignition time delay for reduced set 1 is 110 μs (same as for the full set) compared to the ignition time delay for reduced set 2 of 1620 μs. The difference of a factor of about 15 is significant and should be considered when it is necessary to use such a reduced set. The shift is observed in the temperature profiles. While the reduced set 1 temperature profile is indistinguishable from the full set, reduced set 2's profile is shifted by the same shift in ignition time delay.

We then reduced the MMH/RFNA set further to 29 species and 120 reactions. Michael Nusca of ARL tested the sets in a CFD simulation of the AMRDEC Vortex Engine, comparing the predictions to those of a 49-species, 68-reaction set. Note that computation time depends more on the number of species than the number of reactions, as the number of mass balances to be solved corresponds to one for each species. In Fig. 8-6, the UMass set is shown to give qualitative dynamic accuracy of the pulse heat release and quantitative accuracy of the long-time chamber pressure.
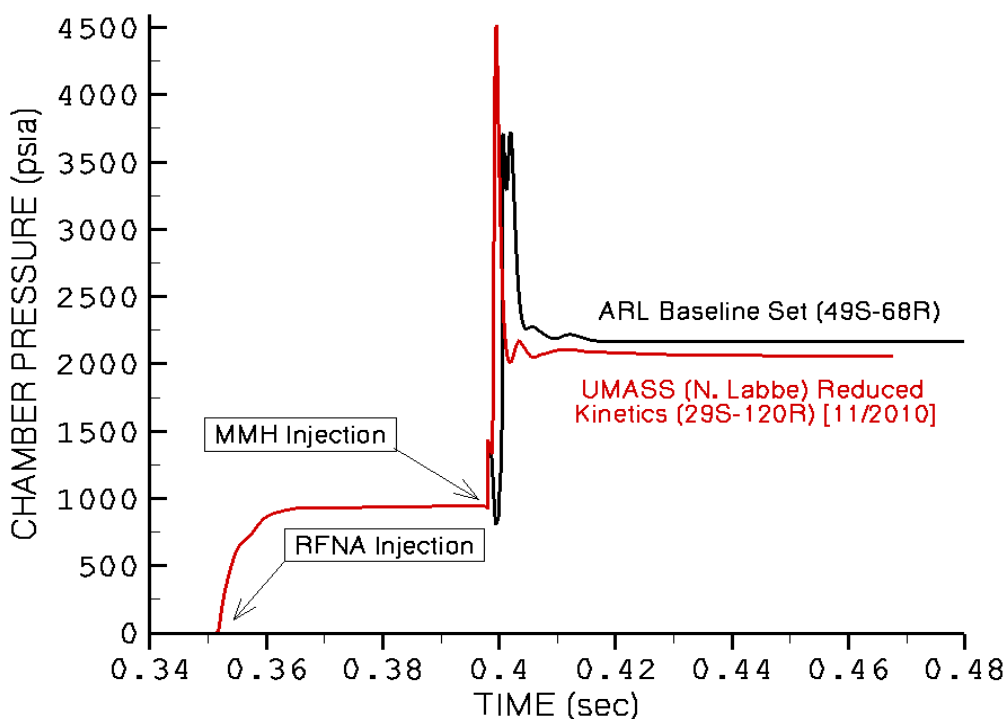
Figure 8-6: Comparison of the workhorse reduced ARL mechanism to the Labbe reduced mechanism for the Vortex Engine [performed by Michael Nusca of ARL, personal communication].

9.0 Spray Combustion

9.1. Experimental System Description

The main experiment related to spray combustion of hypergolic propellants relied on an unlike doublet impinging jet injection system with a 60° included impingement angle (see Figure 9-1).
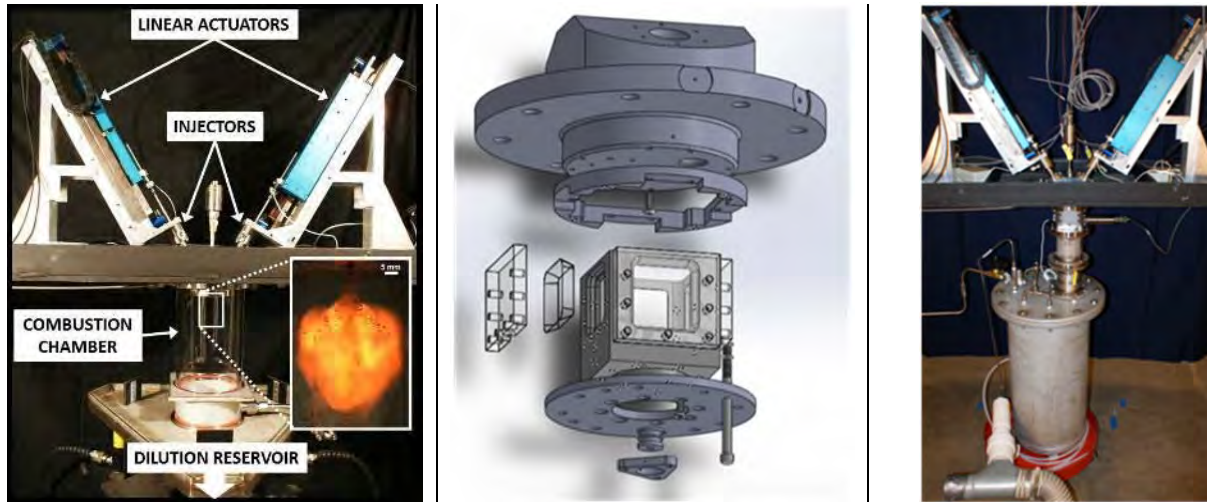
Figure 9-1. Unlike-doublet injection system with optically clear chamber (left), exploded chamber and injector plate (center) and fully assembled system on test stand (right).

In this system, propellants are loaded into the stainless steel syringe injectors (see Figure 9-2) by hand in dedicated fuel and oxidizer fume hoods and then mounted to the injector plate where the linear motors are incrementally lowered and fixed to the plungers. An array of interchangeable orifices with diameters from 0.0250 to 0.0600 inch are available to accommodate different propellant densities, target oxidizer to fuel ratios (O/F), and spray jet parameters. The injectors contain enough propellant to perform tests up to approximately 1000 ms dependent of mass flow rate and mixture ratio of both propellants.
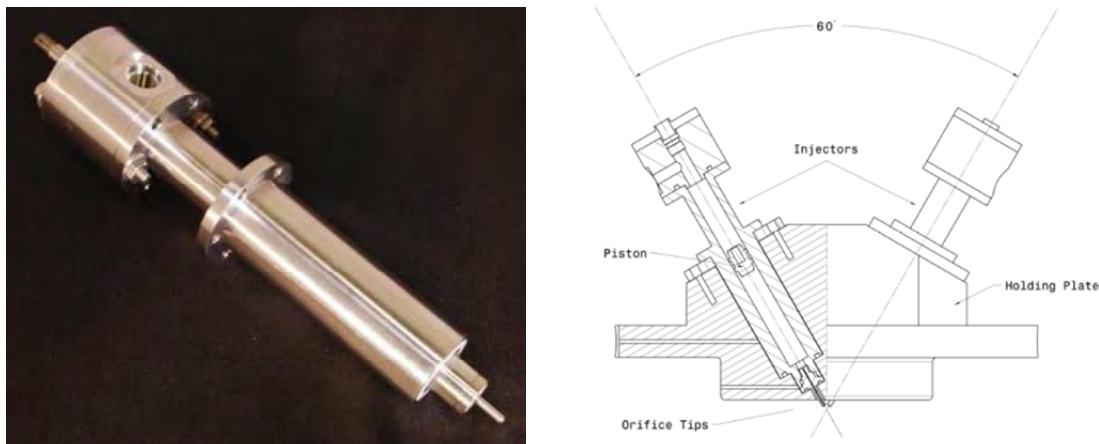
Figure 9-2. Assembled injector (left) and injector assembly drawing (right).

The injector plate houses the fuel and oxidizer injectors and has ports for measuring the chamber pressure and temperature at the injector plate face. A spray nozzle used for water and nitrogen purge is also installed in the injector plate face. The motion of the piston in the injector body used to inject the propellant is controlled by a linear motor driven positioning stage. The linear motors have a 4 inch travel length and can provide 150 lb$_f$ of peak pushing force.

The injection system can be coupled to two combustion chambers: a 360° optically accessible fused silica cylinder with a 6 inch inner diameter and 9.75 inch height for near atmospheric pressure experiments, and a 200 psi rated square cross-section combustor fitted with four windows (see Figure 9-1, center and right).

The exhaust management system is capable of diverting, cooling, and disposing of all toxic products. The flow exiting the combustion chamber must be cooled to protect the lab's ventilation system. Four pressure swirl atomizer nozzles mounted on the tank lid are fed 400 g/s of water before and during firing. The 13 gallon aluminum expansion tank operates as an open system with a vacuum ejector and the facility exhaust fan drawing the cooled and expanded gas out to avoid unchoking the nozzle. A section of pipe with a series of drilled holes acts as a diffuser at the tank inlet to lower the momentum of the flow and contain an ejected nozzle in the event of over-pressurization in the combustor.

9.2. Propellants Overview

The propellants used in this study were obtained from multiple manufacturers. Within each manufacturer, there has been some variability regarding the propellant quality with the most variations coming from the RFNA obtained from Sigma-Aldrich. The information regarding the source of each propellant used during the project period and pertinent information is summarized in Table 9-1.

Table 9-1. Propellant information.

Propellant	Supplier	Part No.	Notes
DMAZ	Mach I	-	Manufactured by 3M
H$_2$O$_2$	FMC	-	91.2%
MMH-1	Fluka Analytical	675540	purum $\geq$ 98%
MMH-2	Fluka Analytical	675540	purum $\geq$ 98%
Nitric Acid	Sigma-Aldrich	78005	puriss. p.a., $\geq$ 99.5%
RFNA-1	Sigma-Aldrich	309079	12 to 24% N$_2$O$_4$
RFNA-2	Sigma-Aldrich	309079	12 to 24% N$_2$O$_4$
TMEDA	Aldrich	411019	$\geq$ 99.5%

9.3 Liquid Hypergols Ignition Results

From the first calibration experiments with water and ethanol in 2009 to the latest results with green hypergolic propellants at chamber pressures up to 200 psia, the impinging jet system has performed over 200 test firings. The results of several studies are summarized in five conference papers and one journal paper submitted for publication in the Journal of Propulsion and Power.

Following the initial work dedicated to characterizing the response time and performance of the system, three major studies performed with the impinging jet system stand out and are

summarized here. The first study aimed at determining the experimental conditions required for a reliable and well defined ignition process within the optically clear fused silica combustion chamber. The second study focused on comparing the ignition and combustion of liquid and gel hypergols. In the third study, we characterized the effects on an inclined impact plate on the spray breakup and ignition processes with liquid MMH/RFNA.

9.3.1. Critical Ignition Criteria for MMH/RFNA

In the first study summarized herein, we focused on the observed spray behavior during impingement, mixing, and ignition in an impinging jet apparatus with a goal of better understanding the ignition threshold for the hypergolic propellant combination of MMH and RFNA.

We varied the contact area between the oxidizer and fuel jets, A_{jet}, through variation in the orifice diameters. At each contact area the total propellant mass flow rate, $\dot{m}^*$, was also varied by changing the injection velocity. All other parameters were held constant throughout the study at the values shown in Table 9-2. The propellants were kept at room temperature for all experiments and the chamber is designed to minimize pressurization above atmospheric pressure during experiments.

Table 9-2. Common injection conditions for MMH/RFNA experiments

Parameter	Value
Jet Momentum Ratio, R_m	1.68
Oxidizer to Fuel Diameter Ratio	1.15
Oxidizer to Fuel Ratio, *O/F*	2.0
Injection Duration	50 ms

The jet momentum ratio listed in Table 9-2 is defined by,

$$R_m = \frac{\rho_{ox} A_{ox} v_{ox}^2}{\rho_f A_f v_f^2}, \tag{9.1}$$

where ρ is the jet density, A is the area of the jet and v is the jet velocity for either the oxidizer (ox) of fuel (f). The optimal oxidizer to fuel ratio (O/F) for stoichiometric combustion of MMH and RFNA at near atmospheric pressure occurs at 2.76.

The variation of initial contact area is shown in Table 9-3 along with the non-dimensional contact area, A^* (A/A_{max}), and associated oxidizer and fuel orifice diameters. Each of these contact areas were tested with three different total propellant mass flow rates (fuel+oxidizer). The mass flow rates and non-dimensional mass flow rates, $\dot{m}^*$ ($\dot{m}/\dot{m}_{max}$), are shown in Table 9-4.

Table 9-3. Injector orifice diameters and area ratios used for the experimental study

Ox Orifice Diameter [mm]	Fuel Orifice Diameter [mm]	Contact Area [mm²]	Non-dimensional Area, A^*
0.73	0.64	0.91	0.23
0.86	0.73	1.25	0.32
0.99	0.86	1.67	0.42
1.14	0.99	2.22	0.56
1.23	1.06	2.57	0.65
1.32	1.14	2.96	0.75
1.52	1.32	3.95	1.00

Table 9-4. Injector orifice diameters and area ratios

Mass flow rate, $\dot{m}$ [g/s]	Non-dimensional mass flow rate, $\dot{m}^*$
10	0.25
25	0.63
40	1

The residence time, or the time during which the propellants are in intimate contact and can mix, is calculated from,

$$\tau_{res} = \frac{D_{jet}}{v_{jet} \sin^\theta/_2 \cos^\theta/_2},$$
(9.2)

where D_{jet} is the jet diameter, v_{jet} is the jet velocity and θ is the included angle in the impinging jet apparatus, 60° in this case. If the residence time is too short, there is insufficient time for the propellants to mix and react. In turn, residence times that are too long can lead to poor atomization and, potentially, reactive stream separation.[70]

Data Analysis

Following common practice, ignition delays were determined in this study as the time difference between first contact of the jet streams and first sign of visible light on the recorded high speed videos. Each of the test conditions was classified based on the probability that ignition occurred in less than 10 ms. Ignition events occurring after 10 ms were typically due to propellant buildup on the injector face and not from reaction occurring in the spray.

Ignition Results

The linear actuators used to control the injections in the present study provide repeatable events with short rise times. The steady state velocity, overshoot and recovery are all repeatable from day to day allowing comparison of tests performed throughout experimental campaigns. Figure 9-3 shows the actual piston velocity recorded by the actuator linear encoders for three individual injections performed on three separate days. Approximately 3 ms after motion is commanded, the actuators achieve and maintain a velocity within 10% of the commanded value. These qualities provide confidence that all of the commanded injections are comparable.
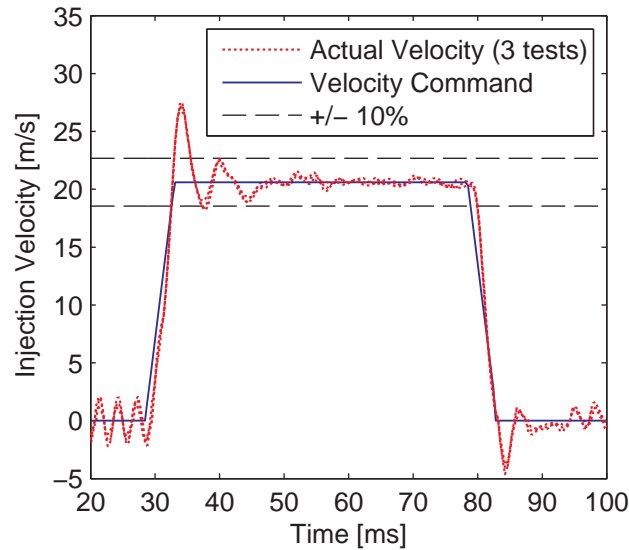
Figure 9-3. Commanded velocity and actual injection velocity for three experiments.

As described in the previous section, all experiments were inspected and classified as ignition or non-ignition cases. A minimum of five experiments were performed at each condition and the percentage of cases that ignited (ignition probability) was calculated for each condition. The ignition probability (IP) is divided into three regions; greater than 80% is classified as a "good ignition" condition, between 40% and 80% is a transition region and below 40% is a "failed ignition" condition. Conditions with high ignition probability but observed RSS are indicated with a filled green square. Figure 9-4 shows the ignition probability results and the transition from no ignition to intermediate ignition and repeatable ignition.
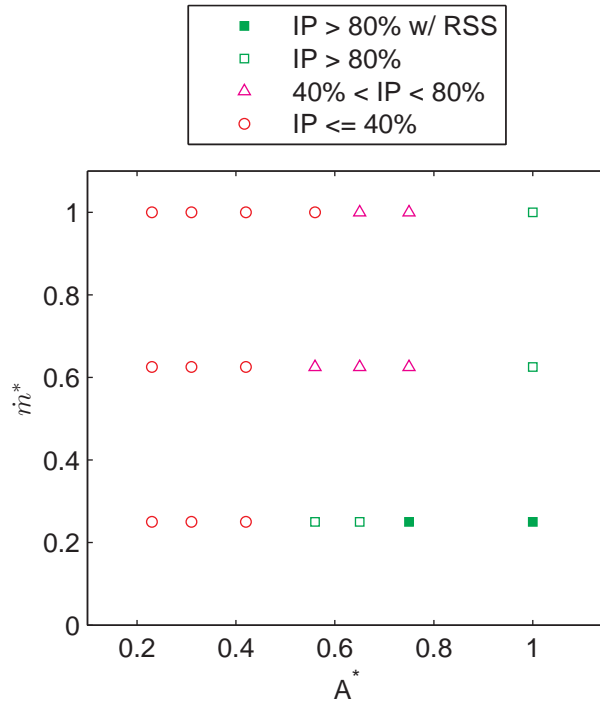
Figure 9-4. Ignition probability as of function of A^* and $\dot{m}^*$

The calculated residence times for each condition show that as residence time increases the ignition probability also increases as shown in Figure 9-5. Again, the residence time threshold appears to show some non-dimensional mass flow rate dependence but quantifying that dependence would require more experimentation. Based on the current results the minimum residence time to achieve ignition is 0.2-0.4 ms.
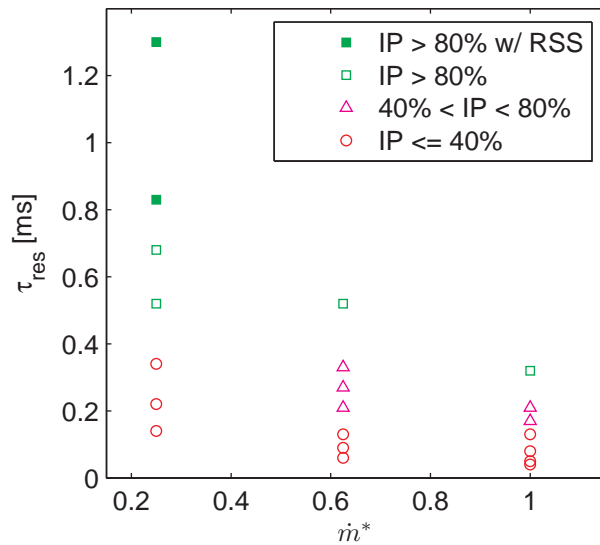
Figure 9-5. Residence time vs. non-dimensional mass flow rate showing ignition probability.

Reactive Stream Separation

As described by Lawver et al. for hydrazine/NTO there are injection conditions that cause separation of the oxidizer and fuel during hypergolic propellant impingement.[70] Stream separation was also achieved in the present study with MMH/RFNA. Images from the 10 and 25 g/s injection conditions for the $A^* = 1.0$ case are shown in Figure 9-6.

| a) | b) |
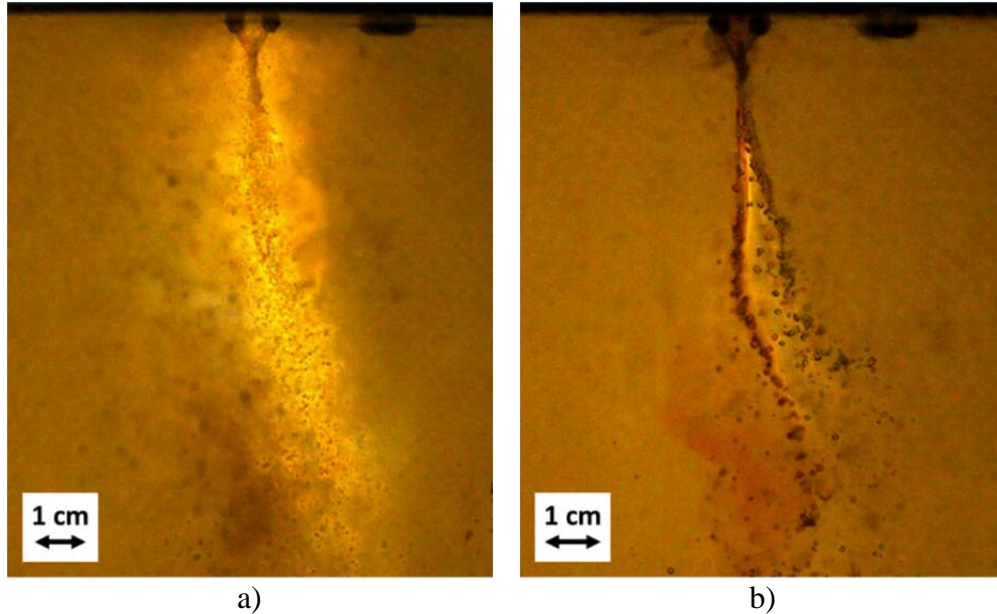
Figure 9-6. Images of test conditions showing mixing and RSS cases, a) $A^* = 1.0, \dot{m} = 25\ g/s$, b) $A^* = 1.0, \dot{m} = 10\ g/s$.

The low carbon content of MMH causes the flame to be very faint in these images but it is recognizable by a glow engulfing the spray sheet in Figure 9-6a and between the two streams in Figure 9-6b. In these images the oxidizer is being injected from left to right and the fuel from right to left.

At the 10 g/s condition for $A^* = 0.75$ and $A^* = 1.0$ RSS was observed but did not occur for every test at those conditions. The corresponding residence times were 0.72 ms and 1.12 ms respectively for the RSS conditions. The average ignition delays for these conditions were approximately 7.4 ms and 6.1 ms respectively. In contrast to the results reported by Lawver et al. for hydrazine/NTO, the critical ratio τ_{ign}/τ_{res} for RSS is not unity but closer to 6-10 for MMH/RFNA. This implies slower physical or chemical processes are dominating the ignition of MMH/RFNA compared to hydrazine/NTO. The lower vapor pressure of RFNA likely is a major contributor to the higher ratio, since a portion of heat production is lost to raising the RFNA to its boiling point.

9.4 Neat vs. Gel Ignition Results

Gel Characterization

The gelling agents considered in this study are Klucel® HF Pharm grade HPC and Aerosil® R974 hydrophobic fumed silica.[71,72] The hydrophobic coating on Aerosil® R974 allows for gel mixing without pre-drying the fumed silica. Previously, RFNA was gelled with Cabosil© M5 fumed silica but the hydrophilic surface allowed significant water absorption. Aerosil® R974 also reduced the required inert gelling agent concentration by 1 wt.% allowing the gelled propellant to contain more reactive material. Typical fumed silica gelled propellants are shown in Figure 9-7.
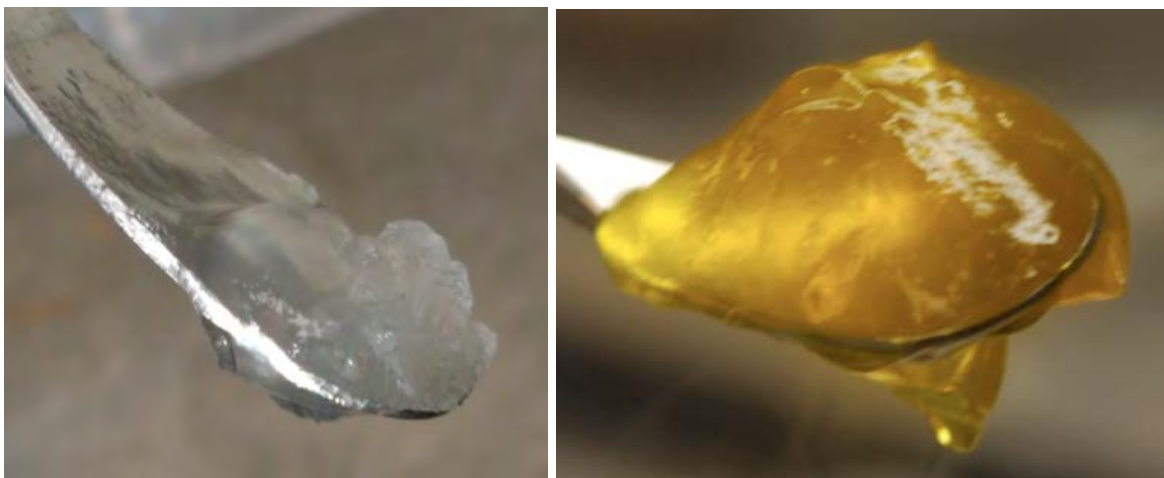
Figure 9-7. MMH/6 wt.% Aerosil gel (left) and RFNA/3 wt.% fumed silica gel (right).

MMH gels were prepared with 3 wt.% HPC as well as 5 and 6 wt.% Aerosil. The 5 wt.% Aerosil gels flow slightly under their own weight while the 6 wt.% Aerosil gels are stiff and do not flow. As anticipated, the 5 wt.% Aerosil gels have lower viscosities than 6 wt.% Aerosil gels over the entire shear rate range investigated. Yield stress measurements for these gels are also lower than the 6 wt.% Aerosil gels. RFNA gels required 3 wt.% Aerosil to obtain the desired gel properties.

RFNA/Aerosil gels had an average PL consistency index of 90.5 ± 21.86 Pa-s^n compared to 80.6 ± 45.7 Pa-s^n for MMH/ 6 wt.% Aerosil gels. The lower standard deviation indicates that the RFNA/Aerosil gel has less batch and measurement variation. Significant PL exponent standard deviations were found for both MMH and RFNA gels, but all gels considered, including MMH/HPC gels tested by Kubal et al., exhibit the shear thinning behavior required for rocket propulsion applications as indicated by PL exponents less than one.[45] The large standard deviations for the MMH/Aerosil gels may indicate that the manual gel mixing technique is insufficient to create a uniform gel. In addition, measurements taken on different days with different batches of gel likely increase the measurement variation. RFNA/Aerosil gels show more consistent curve fit parameters but, similar to MMH/Aerosil gels, still have significant variation in measured yield stress and PL exponent. The well-defined high shear mixing procedure followed for RFNA gels creates a more uniform gel and less batch variation but still requires more research to improve gel consistency.

Ignition Tests

a. MMH/HPC on RFNA/Fumed Silica

Ignition was not observed during testing with MMH/3wt.% HPC and RFNA/4wt.% fumed silica.[45] The MMH/HPC jet formed a sheet after impingement with the RFNA/fumed silica jet. The gelled MMH sheet did not break up even at the highest attainable injection velocities as reported by Kubal et al.[73] and shown in Figure 9-8. The Reynolds numbers presented in Figure 9-8 were calculated using a PL based calculation discussed by Kubal et al.[73] This Reynolds number takes into account the consistency index and exponent from the PL curve fit.

$Re_{RFNA} = 5000$, $V_{RFNA} = 11.9$ m/s $Re_{RFNA} = 10000$, $V_{RFNA} = 17.7$ m/s

$Re_{RFNA} = 15000$, $V_{RFNA} = 22.3$ m/s $Re_{RFNA} = 20000$, $V_{RFNA} = 25.9$ m/s
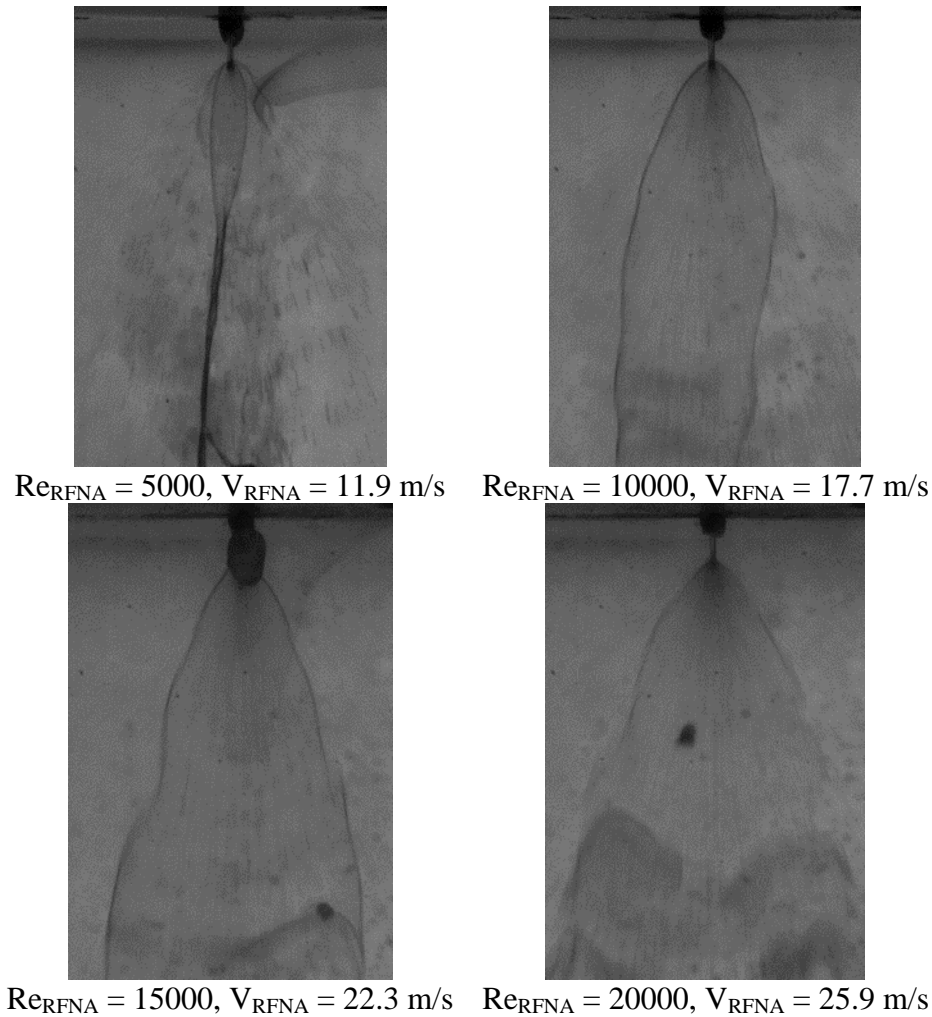
Figure 9-8. MMH/HPC on RFNA/fumed silica impinging jet test results.[4]

The elastic nature of the MMH/HPC sheet inhibits mixing of the fuel and oxidizer streams resulting in no ignition. At the highest injection velocities bag-like structures formed and broke away from the MMH/HPC sheet far from the impingement point.[73] The lack of jet breakup prompted the investigation of alternative gelling agents for MMH. The particulate gelling agent, fumed silica, was selected to better match the rheology of the RFNA/fumed silica gels.

1) MMH/Fumed Silica on RFNA/Fumed Silica

MMH gels were prepared with both 5 wt.% and 6 wt.% Aerosil fumed silica. Ignition was repeatable with the MMH/5 wt.% Aerosil gels but the ignition delay was unacceptably long (>10 ms). Testing with a slightly increased Aerosil concentration of 6 wt.% and RFNA/3 wt.% Aerosil showed repeatable short ignition delays. Ignition was observed near the injector plate, uniformly distributed around the impingement point. Sustained combustion throughout the impingement sheet followed ignition in every test.

A typical ignition event for MMH/ 6 wt.% Aerosil on RFNA/ 3 wt.% Aerosil is shown in Figure 9-9. The cameras are positioned parallel and perpendicular to the spray sheet formed after impingement (top and bottom images as indicated by the left-most frames). Video is captured with standard optical cameras and a false color map is applied based on pixel intensity to aid in flame zone visualization. The red-orange parts of the image are flame and black areas are the propellant spray or empty parts of the chamber.
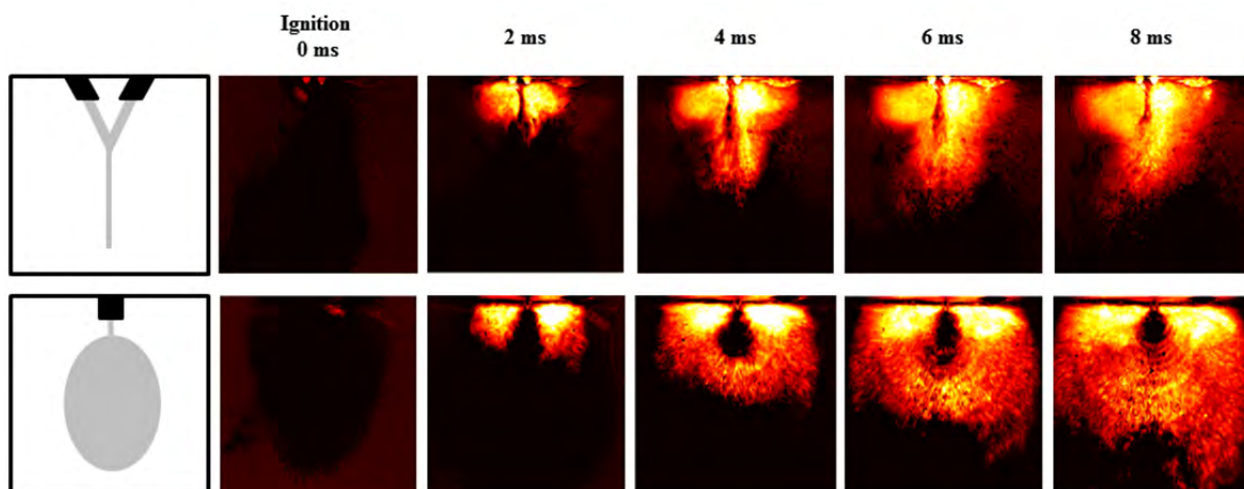
Figure 9-9. False color images of MMH/6 wt.% Aerosil on RFNA/3 wt.% Aerosil combustion.

The results of two gelled propellant test series are shown in Table 9-5 where the average jet velocity, which is simply the average of the oxidizer and fuel jet velocities, is presented to simplify data presentation.

Table 9-5. Ignition delay data for MMH/6 wt.% Aerosil on RFNA/3 wt.% Aerosil .

Test #	Average Jet Velocity [m/s]	Ignition Delay [ms]
1	17.1	4.4
2	8.4	4.6
3	14.2	4.1
4	11.5	4.9
5	17.1	3.1
6	14.2	2.4
7	11.5	3.6
8	17.1	4.8
9	8.4	6.0
10	14.2	3.0
11	11.5	3.8
12	17.1	3.6
13	8.4	5.4
14	14.2	4.2
15	11.5	4.0

Repeatable ignition occurred at all injection conditions with the MMH/6 wt.% Aerosil and RFNA/3 wt.% Aerosil gels. Ignition events always originated around the impingement point and spread downward throughout the spray sheet. As testing proceeded, significant buildup was observed on the combustion chamber in line with the spray sheet. The inert nature of the Aerosil prevents it from being combusted with the propellants. With RFNA, this is an issue that is unlikely to be resolved however, for fuels such as MMH combustible gellants are possible and are being investigated.

2) Comparison of Neat and Gelled Ignition

Neat MMH and RFNA were also tested in the IJ apparatus and repeatable ignition events were observed for all injection conditions. Ignition occurred initially approximately one inch below the impingement point and then near the injector face. After ignition, combustion is sustained throughout the entire injection duration. Neat and gelled propellants are compared in Figure 9-10. Neat propellant ignition delay results are shown in Table 9-6.
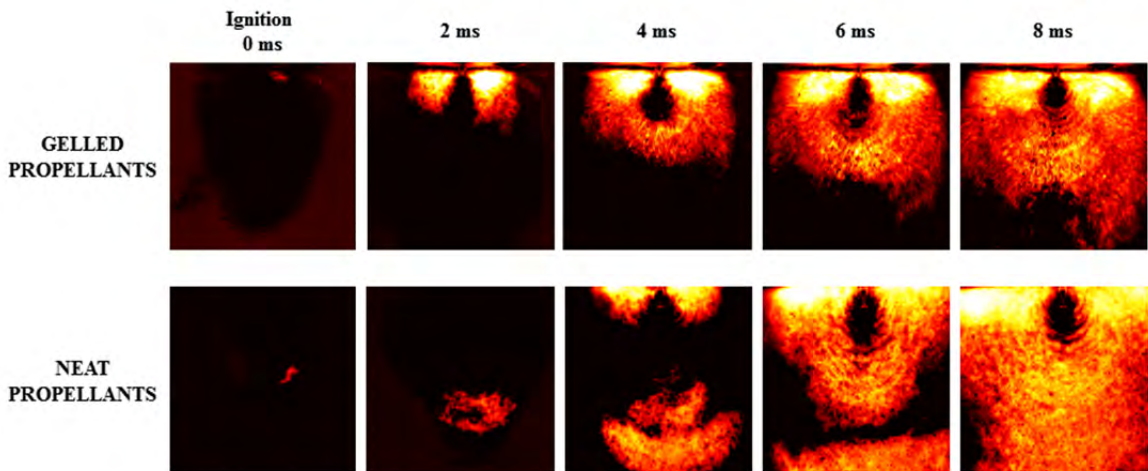
Figure 9-10. False color images of neat and gelled MMH/RFNA shortly after ignition and combustion (View of the impingement plane only).

Table 9-6. Ignition delay data for neat MMH on neat RFNA.

Test #	Average Jet Velocity [m/s]	Ignition Delay [ms]
1	11.5	2.8
2	11.5	3.2
3	14.2	2.8
4	11.5	4.4
5	14.2	3.6
6	14.2	3.3
7	17.1	3.3
8	17.1	2.7
9	17.1	4.4
10	8.4	4.9
11	8.4	4.7
12	8.4	3.0
13	8.4	3.4

The first ignition of neat propellants occurs just below the impingement point and after a short delay a second ignition occurs around the impingement point whereas for gels ignition occurs around the impingement point as shown in Figure 9-10. Sustained combustion of both neat and gelled propellants engulfs the entire spray sheet, but with gelled propellants a larger number of dark spots are present indicating unburned silica particles. The time delay from ignition to full combustion of the spray sheet is nearly the same for the neat and gelled propellants despite the differences in ignition process.

The ignition process is suspected to be heavily influenced by the rheological properties of the propellants after injection. The mechanisms that allow for shear thinning behavior with the silica gels have been discussed previously by Arnold et al.[74] The silica-silica bonds form a network

inside of the liquid propellant. This network is made up of hydrogen bonding between the silica particles. When shear is applied this network begins to break down allowing the gel viscosity to decrease. After some time at rest the hydrogen bonds begin to reform and the gel viscosity increases again. This is schematically shown in Figure 9-11.
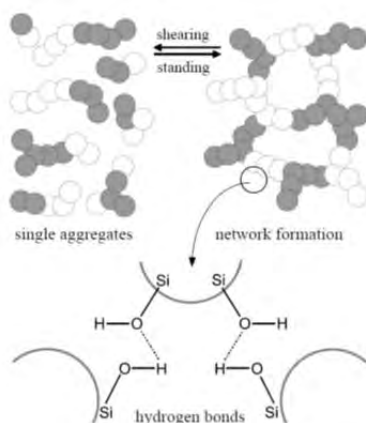
Figure 9-11. Schematic of fumed silica gel formation mechanism.[13]

The thixotropic property of silica gels prevents the gel from instantly reforming a full gel network after shear is removed. Therefore, it is suspected that the propellants that are impinging are still at reduced viscosities similar to neat propellants. The particulate gel mechanism is in contrast to the entanglement mechanism that allows HPC to form a gel. HPC forms a network of entangled polymers which impart elastic properties to the final gel. HPC gels do not possess thixotropic properties and are suspected to return to the pre-shear viscosity very quickly. The mechanism of gel formation has a major impact the usefulness of a gelled propellant for testing in the IJ apparatus.

Ignition delays for neat and gelled propellants were very similar as shown in Figure 9-12. Almost no dependence on injection velocity was observed for neat propellants. The narrow range of injection velocities tested does not allow for a conclusion about injection velocity dependence to be made for gelled MMH and RFNA.
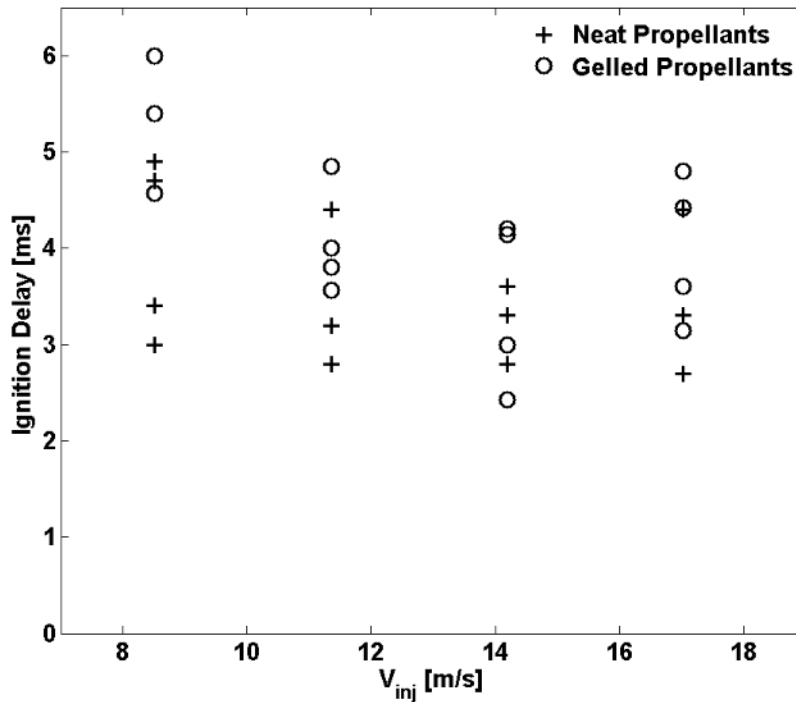
Figure 9-12. Comparison of neat and gelled ignition delays for MMH/RFNA (d_{ox} = 1.32 mm, d_f = 1.32 mm, R_m = 1.68, O/F = 2.0).

In summary, ignition delays are very similar for neat and Aerosil^{TM} gelled MMH/RFNA propellants. Qualitatively however, the ignition processes for neat and gelled propellants are different. For gels, ignition consistently begins around the impingement point while for liquids ignition first occurs below the impingement point and is followed by a secondary ignition event around the impingement point. With both neat and gelled propellants full sustained combustion is achieved after the same post-ignition delay.

9.5 Effects of an impact plate on spray impingement and ignition processes

Following several coordination teleconferences with Drs. Nusca and Anthenien, the impinging jet system developed by Purdue was adapted to simulate the conditions near the chamber wall of the Impinging Stream Vortex Engine (ISVE) of the U.S. Army. The confinement of the spray through the circular combustion chamber wall of the ISVE was simulated with an inclined straight plate mounted below the impingement point with an angle of 30º to the vertical.

Experimental System Description

The impinging jet system was modified by inserting an instrumented plate into the flow field of the spray downstream the impingement point with an inclination of 30º to the vertical, perpendicular to the spray plane created by the impingement. The impact plate was designed to fulfill the following list of requirements:

107

1. Enable measureable temperature change of the plate
2. Provide an angle of 30° to the vertical
3. Be positioned three times the distance d between the impinging point and the orifice tips downstream the impinging point (see Figure 9-13)
4. Be as wide and long as possible to keep edge effects to a minimum
5. Ensure easy mounting in the chamber with an accuracy of ±0.5% for the horizontal distance from the injectors and the inclination angle to the vertical
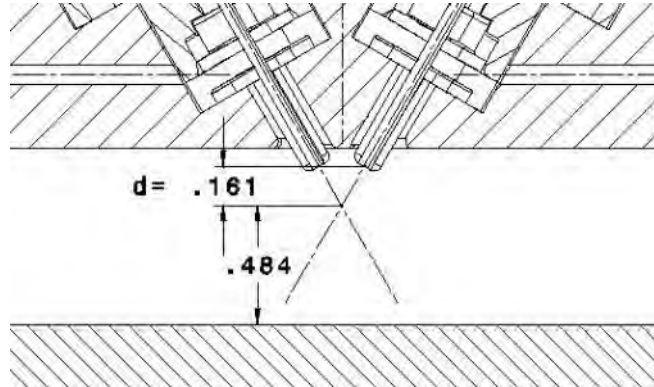
Figure 9-13. Illustration of dimension *d*, distance separating the jet impingement point to the impact plate.

The impact plate was fitted with a 30 holes thermocouple pattern shown in Figure 9-14. The thermocouple holes were drilled such that a wall thickness of 1.6 mm remained between the thermocouple tip and the plate surface in contact with the propellants.
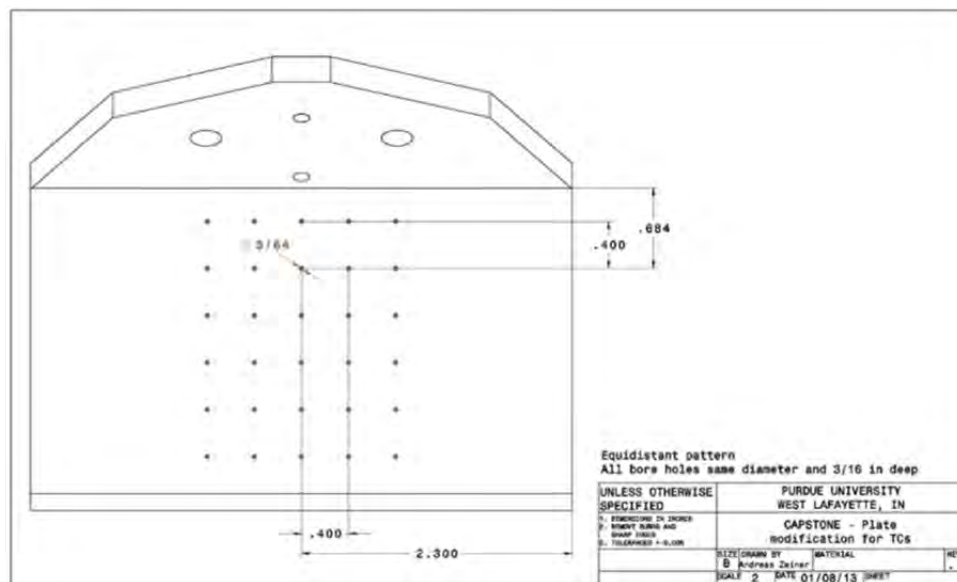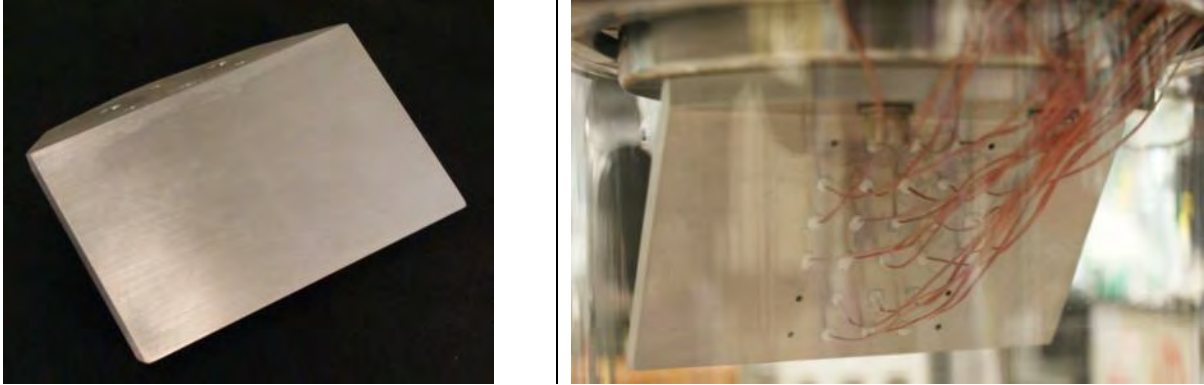
Figure 9-14. Machine drawing (top), front (bottom left), and back of the instrumented impact plate (bottom right).

The numbering of the positions equipped with thermocouples is provided in Table 9-7. The view for that pattern is from the back side of the plate meaning the pattern should be mirrored at the horizontal axis when looking at the front of the plate. These numbers correspond to the channels used in the data acquisition software during the tests.

Table 9-7. Numbering of installed thermocouples (back side view)

	1	2	3	
4	5	6	7	8
9	10	11	12	13
14	15	16	17	18
	19	20	21	
	22	23	24	

This pattern is located on the plate so that the position of thermocouple number 6 is vertically under the impinging point. Most of the thermocouples are located downstream of this location to cover all the area wetted by the spray of the impinging jets.

Ignition and Spray Patterns

An overview of the test parameters used in the impact plate study is given in Table 9-8.

Table 9-8. Overview of test conditions

Parameter	Value	Unit
v_{ox}	2.5 - 8.5	m/s
v_{fu}	3.1 - 13.1	m/s
R_m	1.7	-
O/F	2.7	-
d_{fu}	1.0	mm
d_{ox}	1.3	mm

A typical ignition behavior observed with the inclined plate below the impingement point is pictured in Figure 9-15. The indicated times are from the time of first contact of both jets since ignition delay is defined as the time between first contact and first visible light.

a) t = 1.8 ms, Plate impact   b) t = 2.8 ms, First gas production   c) t = 3.4 ms, Ignition
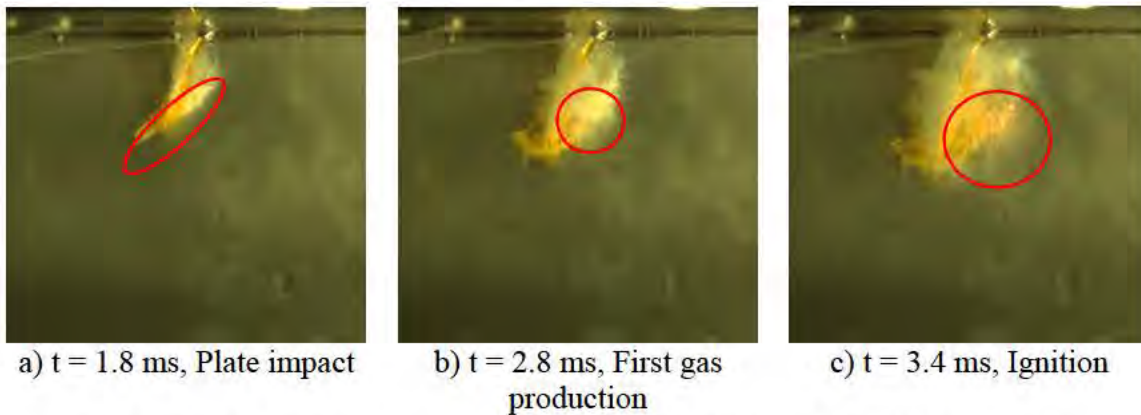
Figure 9-15. Selected frames of MMH/RFNA ignition with impact plate

The analysis of ignition delay of tests with similar injection conditions is summarized in Table 9-9. The consistency of all the ignition times is remarkable since experiments without a secondary impingement surface showed a greater fluctuation in ignition time delay.

Table 9-9. Ignition delays from impact plate experiments

Mixing Time (ms)	# of Tests	Avg. Ignition Delay (ms)	Mean Dev. from Avg. (%)
0.25	7	4.6	12
0.3	12	3.6	11

The secondary impingement on the surface of the inclined plate adds a mixing region to the spray dynamics which affects the ignition behavior as well as the combustion behavior. This additional mixing of the sprayed propellants helps to start up the ignition process but is also a trigger source for further effects like the pre ignition gas production (as shown in Figure 9-16) or explosion like behavior as discussed in the next section. Overall, the secondary impingement helped the mixing in the spray locally and therewith lead to consistent and predictable ignition delays.

| t = 3.0 ms | t = 3.8 ms | t = 4.4 ms |
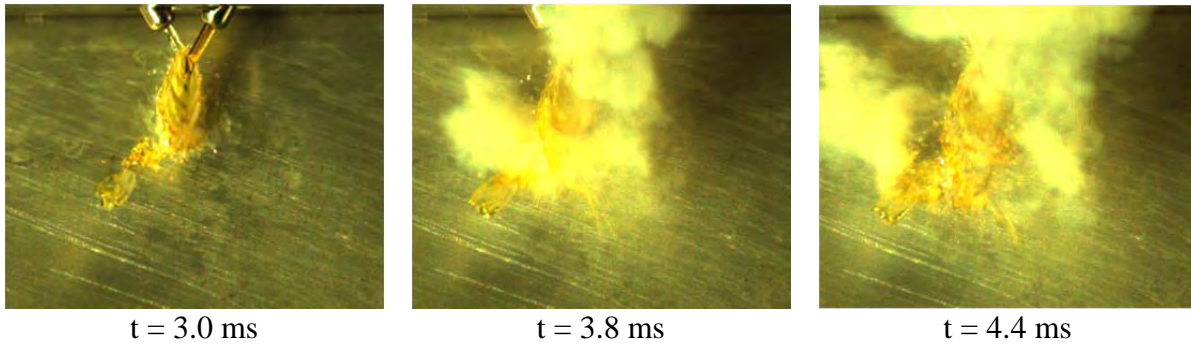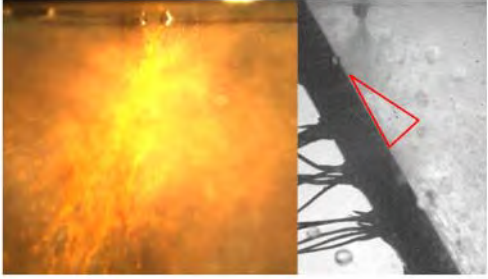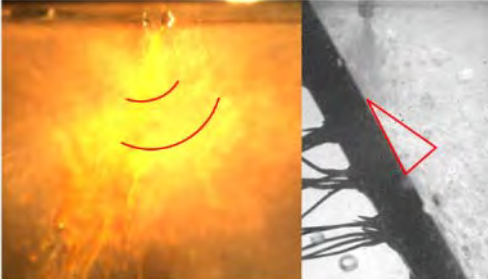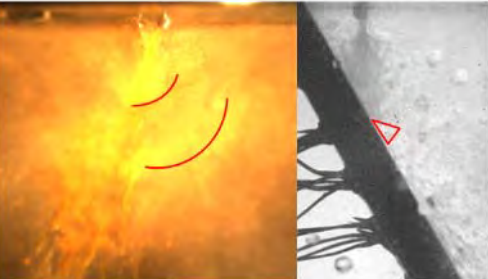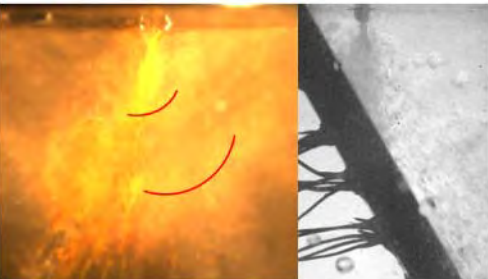
Figure 9-16. Gas production observed prior to MMH/RFNA ignition with impact plate.

Spray Patterns

As mentioned, the confinement of the spray from the location of the impact plate leads to a secondary mixing region. This change or disturbance of the fluid dynamic spray behavior resulted in several experiments to popping during steady state combustion. Similar conditions without the impact plate in previous ignition studies showed popping as well although not reported, but it occurred less frequently and was less severe.

The popping always originated on the same side of the spray and near to initial ignition location. It is postulated that the additional mixing creates a well-mixed enclosed pocket where gas is formed and heated prior to being released rapidly around the propellant spray. Such release is outlined in Figure 9-17 using selected frames the two high-speed video cameras located 90° from one another.

| | a)
t = 19.0 ms
First sign of disturbance (red ellipse) |
| | b)
t=19.2 ms
Accelerating gas visible |
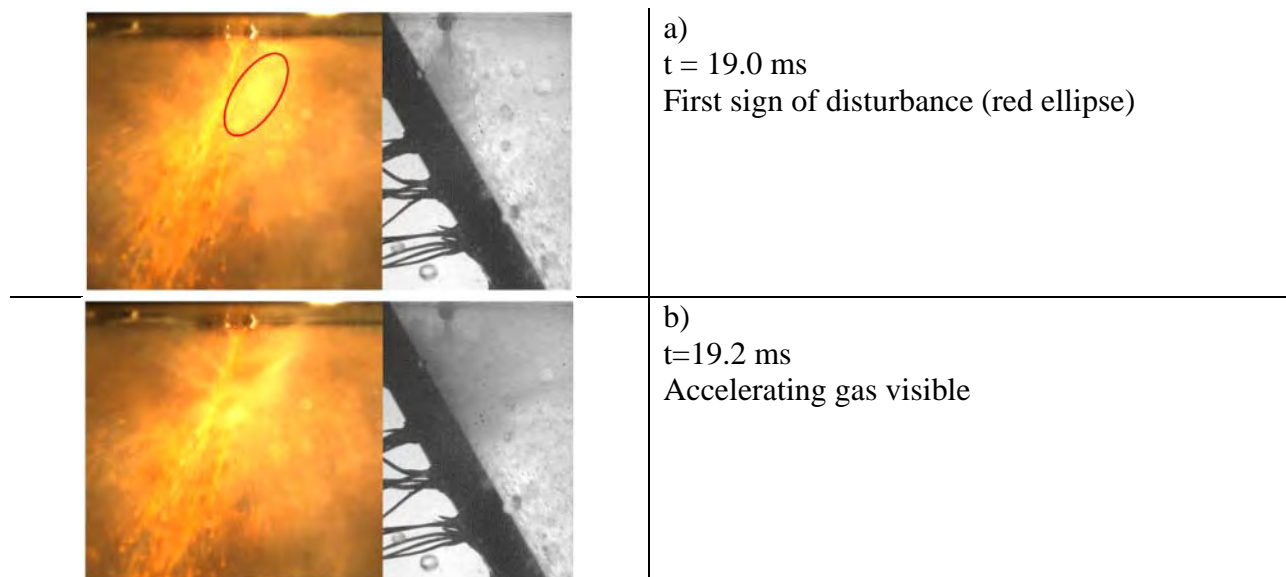
	c) t = 19.6 ms 'gap' visible, where less liquid is due to combustion in pop (red triangle)
	d) t = 20.0 ms Developing shockwave gets visible
	e) t = 20.4 ms Most intense view of wave, disturbance (triangle) near plate nearly deflagrated
	f) t = 21.0 ms Wave still visible, but second maximum of combustion fades out

Figure 9-17. Time sequence of typical popping event observed with impact plate.

The popping event leads to a significant disturbance in the spray, nearly all liquid gets either combusted or blown away within 0.4 ms at the location of the pop. It takes the spray about 4 times longer to recover than the propellants get blown away. Since the popping was only observed in a distinct range of injection velocities (7-9 m/s), the effect is not expected to occur frequently at injection velocities highly above that value. However, the pressure wave travelling through the chamber and up the injector will definitely reduce the injection velocity which may lead to conditions at which popping is likely.

Table 9-10 shows the number of observed pops over the range of investigated jet residence times. Since some velocities were tested more often and some less, the number of pops was divided by the total test duration during which they occurred. This value is presented in Table 9-10 as popping probability.

Table 9-10. Theoretical frequency of popping with impact plate

Mixing Time (ms)	# of Pops (-)	Firing Time (ms)	Probability (#/s)
0.25	1	420	2.4
0.3	17	950	17.9
0.34	17	720	23.6
0.5	12	450	26.7
0.7	4	450	8.9
0.9	0	150	0

No regular pattern for popping could be detected; however, it appeared to be a self-amplifying mechanism. A small number of tests showed the occurrence of multiple pops in a row where the time between the pops decreased while their intensity increased.

Pressure and Temperature Data

Although the experimental setup used in the impact plate study does not include a closed chamber with a nozzle, the exhaust pipe leading the combustion gases through a water bath gave enough resistance to build up chamber pressure of less than 1 bar over ambient. This chamber pressure did not reach steady state within the test duration but showed a significant dependency of mass flow rate (see Figure 9-18).
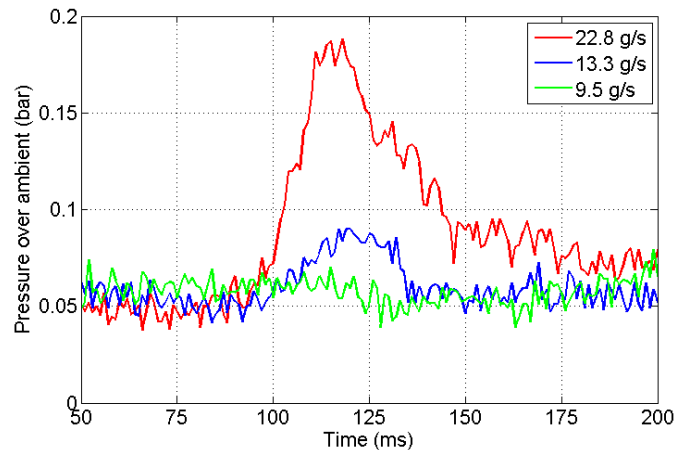
Figure 9-18. Chamber pressure dependence on mass flow.

If a thrust chamber is operated in pulse mode with short durations between pulses, the combustion chamber may be filled with combustion residue and in the case of an oxidizer containing NTO, the chamber can be filled with NTO vapors. Figure 9-19 shows the pressure spikes observed during the pulse tests in the impinging jet apparatus.

The timeline of the pressure on the right of Figure 9-19 is synchronized with the timeline of the motor control on the left. The injection velocity shown on the left is controlled by linear actuators and represents the two injection profiles used for pulse mode tests. While the first pulse

113

is barely visible on that scale, the second and third pulse show significantly higher pressure spikes. The zoom into the tip of one of the pressure peaks shows that multiple points of that spike could be captured at selected recording frequency of 1000 Hz.
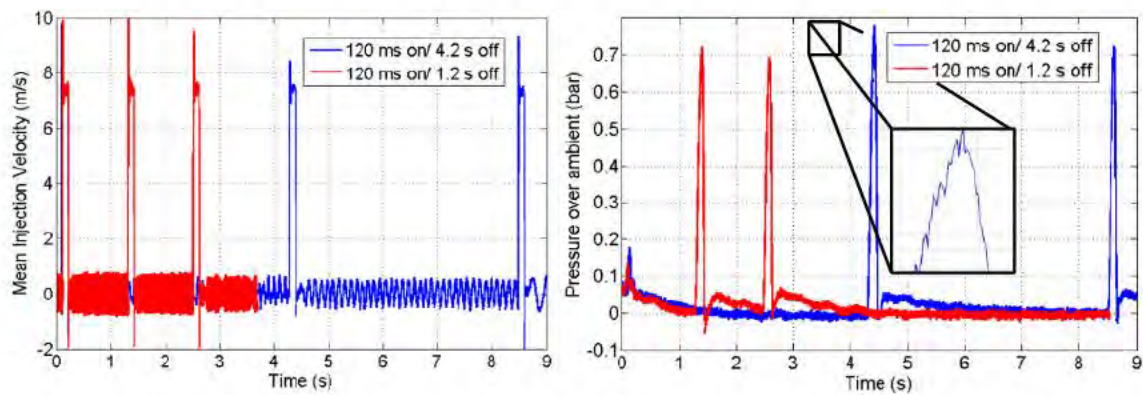
Figure 9-19. Injection velocity and chamber pressure during pulse mode operation.

Figure 9-20 shows the mean temperature of the impact plate for tests with different mass fluxes in single pulse and multiple pulse mode operation. As can be observed, in multiple pulse mode operation, the temperature increase during the first pulse is the same as during the second or third pulse.
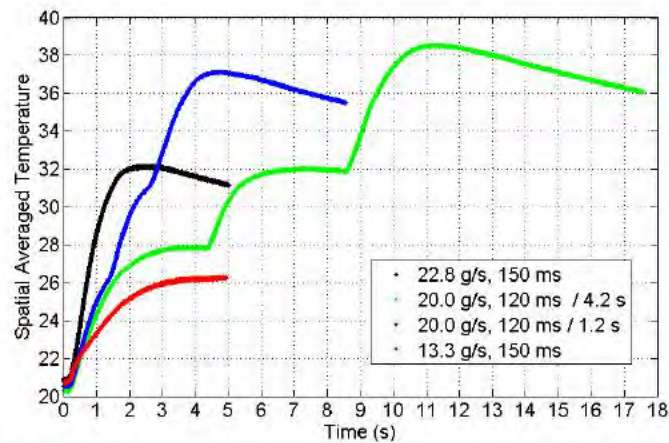
Figure 9-20. Mean impact plate temperature in pulse mode operation.

114

10.0 References

10.1 Publications Generated Under MURI Effort

- Yoon, C., Heister, S., Xia, G., and Merkle, C., "Numerical modeling of Injection of Shear-Thinning Gel Propellants Through Plain-Orifice Atomizer", *AIAA J. Propulsion & Power*, V27, No.5, pp. 944-954, 2011.

- Dambach, E., Rankin, B., Pourpoint, T., and Heister, S., "Temperature estimations in the near-flame field resulting from hypergolic ignition using thin filament pyrometry", to appear, *Combustion Science and Technology*, 2012.

- Dambach, E., Solomon, Y., Pourpoint, T., and Heister, S., "Experimental Study of Hypergolic Ignition with MonoMethyl Hydrazine", *AIAA J. of Propulsion and Power,* V29, No. 2, 331-338, 2013.

- Yoon, C., Heister, S., Merkle, C. L., Xia, G., "Simulations of Plain-Orifice Injection of Gelled Propellants Under Manifold Crossflow Conditions", *AIAA J. of Propulsion and Power,* V29, No.1, 136-146, 2013.

- Yoon, C., Heister, S. D., and Campanella, O. H., "Modeling gelled fluid flow with thixotropy and rheological hysteresis", Fuel, V128, 467-475, http://dx.doi.org/10.1016/j.fuel.2014.02.051 ,2014.

- Yoon, C., Heister, S., Xia, G., and Merkle, C.,"Numerical Simulations of Gel Propellant Flow Through Orifices", AIAA 2009-5045, 45th AIAA Joint Propulsion Conference, Denver, CO, 2009.

- Dambach, E., and Heister, S., "Ignition of Advanced Hypergolic Propellants", AIAA 2010-6984, 46th AIAA Joint Propulsion Conference, Nashville, TN, 2010.

- Yoon, C., Watson, C., Heister, S., Xia, G., Merkle, C., and Sojka, P., "Simulation of Injection of Shear-Thinning Gel Propellants Through Plain-Orifice Atomizer", AIAA 2010-7138, 46th AIAA Joint Propulsion Conference, Nashville, TN, 2010.

- Yoon, C., Heister, S., Xia, G., and Merkle C.L., "Simulation of Injection of Shear-Thinning Gel Propellants through Plain-Orifice Atomizer", AIAA-2010-7138, 46th AIAA Joint Propulsion Conference and Exhibit, Nashville, TN, 2010.

- Yoon, C., Xia, G., Merkle, C. L., Heister, S., "Numerical Modeling of Cross-Fed Orifice Flows for Shear-Thinning Fluids", European Conference for AeroSpace Sciences (EUCASS), Saint Peterburg, Russia, July 4-8, 2011.

- Dennis, J., Fineman, C., Yoon, C., Santos, P., Pourpoint, T., Son, S., Heister, S. and Campanella, O., "Characterization of Gelling Systems for Development of Hypergolic Gels", European Conference for AeroSpace Sciences (EUCASS), Saint Peterburg, Russia, July 4-8, 2011.

- Yoon, C., Watson, C., Heister, S., Xia, G., Merkle, C., Sojka, P., "Injector Flow Characteristics for Gel Propellants", AIAA-2011-5707, 47th AIAA Joint Propulsion Conference, San Diego, California, July 31 - Aug. 3, 2011.

- T. L. Pourpoint, J. Dennis, W. E. Anderson, S. F. Son, R. P. Lucht, S. D. Heister, and S. E. Meyer, "Design, Development and Operation of a Combustion Test Facility for Monomethylhydrazine and Red Fuming Nitric Acid Gels", JANNAF Combustion Meeting, 2011.

- T. R. Sippel, S. C. Shark, M. C. Hinkelman, T. L. Pourpoint, S. F. Son, and S. D. Heister, " Hypergolic Ignition of Metal Hydride-based Fuels with Hydrogen Peroxide", 2011 7th US National Combustion Meeting Organized by the Eastern States Section of the Combustion Institute, Atlanta, GA, 2011

- Sardeshmukh, S., Heister, S., Xia, G., and Merkle, C., "Kinetic Modeling of Hypergolic Propellants Using Impinging Element Injectors", AIAA 2012-3760, 48th AIAA Joint Propulsion Conference, Atlanta, Ga., 2012.

- Heister, S.D., and Pourpoint, T.L., "Progress in Understanding the Combustion Physics for Hypergolic Propellants", 5th European Conference for Aeronautics and Space Sciences, Munich, Germany, 2013.

- Forness, J., Pourpoint, T.L. & Heister, S. D., "Experimental Study of Impingement and Reaction of Hypergolic Droplets", AIAA 2013-3772, 49th AIAA/ASME/SAE/ASEE Joint Propulsion Conference, 2013.

- Sardeshmukh, S., Heister, S.D., Sankaran, V., & Wang, H., "Kinetics Modeling of Hypergolic Propellants", AIAA 2013-4157, 49th AIAA/ASME/SAE/ASEE Joint Propulsion Conference, 2013.

- J.M. García-Oliver, J.M. Pastor, A. Pandal, N. Trask, E. Baldwin, and D.P. Schmidt, "Diesel Spray CFD Simulations Based on the Sigma-Y Eulerian Atomization Model," *Atomization and Sprays*, 23(1), pp. 71-95, 2013.

- Nathaniel Trask, David P. Schmidt, Malissa D.A. Lightfoot, Stephen A. Danczyk, "Compressible Modeling of the Internal Two-Phase Flow in a Gas-Centered Swirl Coaxial Fuel Injector," *J. Propulsion and Power*, 28(4), 685-693, 2012.

- Andrew R. Teixeira, Kyle G. Mooney, Jacob S. Kruger, C. Luke Williams, Wieslaw J. Suszynski, Lanny D. Schmidt, David P. Schmidt, Paul J. Dauenhauer, "Aerosol Generation by Reactive Boiling Ejection of Molten Cellulose," *Energy & Environmental Science*, 4 (10), 4306 – 4321, 2011.

- Sandeep Menon and David P. Schmidt, "Supermesh construction for conservative interpolation on unstructured meshes: An extension to cell-centered finite-volume variables," *Comput. Methods Appl. Mech. Engrg*. 200(41-44), 2797–2804, 2011.

- Karl Georg Stapf, Sandeep Menon, David Schmidt, Michael Rieß, Marc Sens, "Charge Motion and Mixture Formation Analysis of a DISI Engine Based on an Adaptive Parallel Mesh Approach," SAE Congress, April, 2014.

116

- David P. Schmidt, Eli Baldwin, Sukanta Rakshit, "Modeling the Internal Flow through Spray A and Spray H Nozzles from the Engine Combustion Network," 25th Annual Conference on Liquid Atomization and Spray Systems, Pittsburgh, PA, May 2013.

- Kyle G. Mooney and David P. Schmidt, "Finite Volume Simulations of the Collision of Viscoelastic Droplets using Adaptive Re-meshing and Explicit Interface Tracking," ICLASS, Heidelberg, September, 2012.

- Kyle G. Mooney, Sharon Snyder, P. E. Sojka, and David P. Schmidt, "Simulation and Experimental Studies of Shear-Thinning Droplet Breakup," ILASS-Americas 23rd Annual Conference on Liquid Atomization and Spray Systems, Ventura, CA, May 2011.

- Nathaniel Trask, J. Blair Perot, David P. Schmidt, Terry Meyer, Malissa Lightfoot, Steven Danczyk, "Modeling of the Internal Two-Phase Flow in a Gas-Centered Swirl Coaxial Fuel Injector," 48th AIAA Aerospace Sciences Meeting, Orlando, FL, 2010.

- Sandeep Menon, Jonathan Rothstein and David P. Schmidt, "A Numerical Study of Axi-symmetric Droplet Formation Using A Moving Mesh Approach," 11th Triennial International Conference on Liquid Atomization and Spray Systems, Vail, Colorado USA, July 2009.

- Muddu, R., Lu, J., Sojka, P. E., Corvalan, C. M. 2012. Threshold wavelength on filaments of complex fluids. Chemical Engineering Science, 69 (1), 602-606.

- Muddu, R., Lu, J., Corvalan C.M. and Sojka, P.E., Effect of Perturbation Wavelength On Jets of Complex Fluids, AIChE Annual Meeting, November 7-12, 2010, Salt Lake City, UT.

- Muddu, Rajeswari. 2010. Effect of perturbation wavelength on jets of complex fluids. Master's Thesis, Purdue University.

- Dechelette, A., Muddu, R., Corvalan C.M., and Sojka, P.E. 2009. Breakup of Shear-Thinning Liquid Sprays Subject to Controlled Disturbances, International Congress on Liquid Atomization and Spray Systems ICLASS, Vail CO.

- Lu, J., Corvalan, C. M. 2012. Coalescence of viscous drops with surfactant. Chemical Engineering Science, 78(20), 9-13.

- Lu, J. and Corvalan, C.M., Surfactant Effects on the Dynamics of Drop Coalescence, AIChE Annual Meeting, October 16-21, 2011. Minneapolis, MN.

- Lu, J., Corvalan, C. M. 2014. Influence of rheology on the impingement of laminar liquid jets. Chemical Engineering Science, submitted.

- Lu, Jiakai. 2014. Influence of shear-thinning rheology on jet impingement and primary atomization events. Ph.D. Thesis, Purdue University.

117

- Muddu, R., Lu, J., Vaidya, N., Sojka, P.E., and Corvalan, C.M. Replacement of interfacial proteins by waves of surfactant. Institute of Food Technologists Annual Meeting, July 17-20, 2010, Chicago, IL.

- Corvalan, C. M., Free surfaces on fluid foods. SHPE 2012 National Conference, November 14-18, 2012. Fort Worth, TX.

- Dechelette, A., Corvalan C.M., and Sojka, P.E. 2010. An experimental investigation on the breakup of surfactant-laden shear-thinning jets, International Congress on Liquid Atomization and Spray Systems, ILASS – Europe 2010, 23rd Annual Conference on Liquid Atomization and Spray Systems, Brno, Czech Republic.

- Corvalan, C. M., Multiphase flow through porous food matrices. 4th International Conference on Porous Media and Annual Meeting of the International Society for Porous Media, May 14-16, 2012. West Lafayette, IN.

- Dechelette, A., Corvalan, C.M. and Sojka, P.E. 2011. Effect of Surfactant Solubility and Adsorption Kinetics on Satellite Droplet Formation. International Conference on Liquid Atomization and Spray Systems, Estoril, Portugal.

- Vaidya, N., and Corvalan, C. M. Interfacial Mass Transfer and Emulsion Stability. Conference of Food Engineering, April 2009, Columbus, OH.

- Vaidya, N., Lu, J., and Corvalan, C.M. Caking of amorphous food powders: a direct numerical simulation. Institute of Food Technologists Annual Meeting, July 17-20, 2010, Chicago, IL.

- Solomon, Y., DeFini, S., Pourpoint, T., and Anderson, W., "Gelled Monomethyl Hypergolic Droplet Investigation," *Journal of Propulsion and Power*, Vol. 29, No 1 (2013), pp. 79-86.

- Arnold, N., Santos, P. H. S., deRidder M., Campanella, O. H., and Anderson, W. E. Comparison of Monomethylhydrazine/Hydroxypropylcellulose and Hydrocarbon/Silica Gels. 48th AIAA Aerospace Sciences Meeting Including the New Horizons Forum and Aerospace Exposition, 4 - 7 January 2010, Orlando, Florida.

- Santos, P.H.S., Carignano M.A. and Campanella, O.H. 2011. Qualitative Study of Thixotropy in Gelled Hydrocarbon Fuels. Engineering Letters, 19(1), 13-19. http://www.engineeringletters.com/issues_v19/issue_1/index.html.

- Santos, P.H.S., Campanella, O.H. and Carignano, M.A. 2010. Brownian Dynamics Study of Gel-Forming Colloidal Particles. The Journal of Physical Chemistry B, 114(41), 13052-13058.

- Santos, P.H.S., Campanella, O.H. and Carignano, M.A. 2013 Effective attractive range and viscoelasticity of colloidal gels. Soft Matter, 9, 709-714. DOI: 10.1039/C2SM26585K.

- Santos, P.H.S., Abiad, M.G, Carignano, M.A and Campanella, O.H.. 2012. Viscoelastic properties of dibenzylidene sorbitol (DBS) physical gels at high frequencies. Rheologica Acta, 51(1), 3-11.

- N. J. Labbe, "Determining Detailed Reaction Kinetics for Nitrogen-and Oxygen-Containing Fuels," Ph. D. Dissertation, University of Massachusetts Amherst (2013). http://scholarworks.umass.edu/open_access_dissertations/719/

- A. Lucassen, N. J. Labbe, P.R. Westmoreland, K. Kohse-Höinghaus, "Combustion chemistry and fuel-nitrogen conversion in a laminar premixed flame of morpholine as a model biofuel," Combustion and Flame 158 (2011) 1647-1666; DOI: 10.1016/j.combustflame.2011.02.010

- N. J. Labbe, V. Seshadri, T. Kasper, N. Hansen, P. Oßwald, P. R. Westmoreland, "Flame chemistry of tetrahydropyran as a model heteroatomic biofuel," Proc. Comb. Inst. 34 (2013) 259-267; DOI: 10.1016/j.proci.2012.07.027

- S. Li, D. F. Davidson, R. K. Hanson, N. J. Labbe, P. R. Westmoreland, P. Oßwald, K. Kohse-Höinghaus, "Shock Tube Measurements and Model Development for Morpholine Pyrolysis and Oxidation at High Pressures," Comb. Flame 160(9) (2013) 1559-1571; DOI: 10.1016/j.combustflame.2013.03.027.

- P. R. Westmoreland, N. J. Labbe, C. D. Needham, T. G. Voskuilen, T. L. Pourpoint, "Predictive Modeling of Hypergolic-Propellant Performance. Part I: Reaction-Kinetics Model for Monomethylhydrazine and Nitric Acid Liquids and Vapors," Combustion and Flame (to be submitted 11/2014).

- T. G. Voskuilen, C. D. Needham, P. R. Westmoreland, T. L. Pourpoint, "Predictive Modeling of Hypergolic-Propellant Performance. Part II: Ignition of Hypergolic Liquids and Shear-Thinning Gels of Monomethylhydrazine and Fuming Nitric Acids," Combustion and Flame (to be submitted 11/2014).

- N. Labbe, P.R. Westmoreland. "Modeling ammonia combustion to develop a comprehensive reaction set for N/H/O kinetics." AIChE Annual Meeting, Pittsburgh PA, October 28-November 2, 2012.

- N. J. Labbe, V. Seshadri, T. Kasper, N. Hansen, P. Oßwald, P. R. Westmoreland, "Flame chemistry of tetrahydropyran as a model heteroatomic biofuel," 34th International Combustion Symposium, Warsaw University of Technology, Warsaw, Poland, July 29-August 3, 2012. [Podium presentation]

- T. Bierkandt, T. Kasper, N. Labbe, P.R. Westmoreland, D.A. Knyazkov, S.A. Yakimov, O.P. Korobeinichev, "Effect of nitrogen addition to low-pressure, premixed flat ethanol flames," 34th International Combustion Symposium, Warsaw University of Technology, Warsaw, Poland, July 29-August 3, 2012. [Poster]

- N. Labbe and P.R. Westmoreland. "Flame chemistry of tetrahydropyran as a model heteroatomic biofuel," 30th Regional Meeting on Chemical Kinetics and Dynamics, SUNY-Albany, Albany NY, January 28, 2012.

- N. Labbe, Y. S. Kim, P.R. Westmoreland. "Computational Mechanism Development for Hypergolic Propellant Systems: MMH and DMAZ." AIChE Annual Meeting, Minneapolis MN, October 7-12, 2011. Podium presentation and poster.

- N. Labbe, P.R. Westmoreland. "Reaction kinetics for TMEDA combustion with red fuming nitric acid." Fall Technical Meeting, Eastern Section of the Combustion Institute,

Univ. of Connecticut, Storrs CT, October 9-12, 2011. Paper A-20. [Charles Fenimore Best Paper Award]

- N. Labbe, A. Lucassen, P.R. Westmoreland, K. Kohse-Höinghaus, "Mechanistic insights into nitrogen fate in a morpholine flat flame." 7th U.S. National Combustion Meeting, Atlanta GA, March 20-23, 2011.

- A. Lucassen, P. Oßwald, N. Labbe, P. R. Westmoreland, K. Kohse-Höinghaus, "Combustion Behavior of Nitrogen-Containing Model Biofuels," Annual Convention of the Deutschen Gesellschaft für Massenspektrometrie, February 27-March 2, 2011.

- N. Labbe and P.R. Westmoreland. "New developments in morpholine flame modeling and mechanism development," 29th Regional Meeting on Chemical Kinetics and Dynamics, University of Massachusetts Amherst, January 29, 2011.

- N. Labbe, Y. S. Kim, P.R. Westmoreland. "Computational Mechanism Development for Hypergolic Propellant Systems: MMH and DMAZ." AIChE Annual Meeting, Salt Lake City UT, November 7-12, 2010. Podium presentation and poster.

10.2 References of Related Material

1. Arnold, R., Santos, P.H.S., Campanella, O.H. and Anderson, W.E. 2011. Rheological and Thermal Behavior of Gelled Hydrocarbon Fuels. Journal of Propulsion and Power 27, 151-162. doi: 10.2514/1.48936.

2. Sutton, G. P., and Biblarz, O., Rocket Propulsion Elements, 7th ed., Wiley, New York, 2001.

3. Teipel, U. and Forter-Barth, U. 2005. Rheological Behavior of Nitromethane Gelled with Nanoparticles," Journal of Propulsion and Power, 21, 40–43. doi:10.2514/1.3471

4. Arnold, R., Santos, P.H.S. Kubal, T., Campanella O. and Anderson, W.E. 2009. Proceedings of the World Congress on Engineering and Cmputer Science, Vol. I WCECS 2009, October 20-22 2009, San Francisco, USA.

5. Yoon, C., Heister, S. D., and Campanella, O. H. "Modeling gelled fluid flow with thixotropy and rheological hysteresis", Fuel, V128, 467-475, http://dx.doi.org/10.1016/j.fuel.2014.02.051 ,2014.

6. Madlener, K. and Ciezki, H. K. Analytical Description of the Flow Behavior of Extended Herschel-Bulkley Fluids with regard to Gel Propellants," 36th International Annual Conference of ICT & 32nd International Pyrotechnics Seminar, Karlsruhe, Federal Republic of Germany, June 28 - July 1 2005.

7. Kubal, T.D., Arnold, R, Pourpoint, T.L., Campanella, O.H and Anderson, W.E. 2010. Rheological Characterization of Hydroxypropylcellulose/Monomethylhydrazine and Silica/Red Fuming Nitric Acid Gels. 46th AIAA/ASME/SAE/ASEE Joint Propulsion Conference & Exhibit July 25-28, 2010, Nashville, TN.

8. Rahimi, S., Peretz, A., and Natan, B. 2007. On Shear Rheology of Gel Propellants," Propellants, Explosives, Pyrotechnics, 32, 165-174.

9.   Rahimi, S., Hasan, D., Peretz, A., and Wellner, S. 2001. Preparation and Characterization of Gel Propellants and Simulants,"7th AIAA/ASME/SAE/ASEE Joint Propulsion Conference & Exhibit, Salt Lake City, Utah, 2001.

10.   Allan, B. D. 1983. Thixotropic IRFNA gel, 26 May 1983, US Patent 6,165,293.

11.   Arnold, R., Santos, P., Kubal, T., Campanella, O., and Anderson, W. Investigation of Gelled JP-8 and RP-1 Fuels," World Congress on Engineering and Computer Science 2009, Vol. 1, San Francisco, USA, 2009.

12.   Santos, P., Arnold, R., Anderson, W., Carignano, M., and Campanella, O. Characterization of JP-8/SiO2 and RP-1/SiO2 Gels," Engineering Letters, Vol. 18, No. 1, 2010.

13.   Morrison, F.A. Understanding Rheology. 2001. Oxford University Press.

14.   Santos, P.H.S., Campanella, O.H. and Carignano, M.A. 2010. Brownian Dynamics Study of Gel-Forming Colloidal Particles. The journal of Physical Chemistry B, 114(41), 13052-13058.

15.   Santos, P.H.S., Campanella, O.H. and Carignano, M.A. 2013 Effective attractive range and viscoelasticity of colloidal gels. Soft Matter, 9, 709-714. DOI: 10.1039/C2SM26585K.

16.   S. Rahimi and B. Natan, "The injection process of gel fuels," in *33rd AIAA/ASME/SAE/ASEE Joint Propulsion Conference and Exhibit* Seattle, WA, 1997.

17.   B. N. Shai Rahimi, "Numerical Solution of the Flow of Power-Law Gel Propellants in Converging Injectors," *Propellants, Explosives, Pyrotechnics,* vol. 25, pp. 203-212, 2000.

18.   H. Ciezki, A. Robers, and G. Schneider, "Investigation of the Spray Behavior of Gelled Jet-A1 Fuels using an Air Blast and an Impinging Jet Atomizer," in *38th AIAA/ASME/SAE/ASEE Joint Propulsion Conference and Exhibit* Indianapolis, Indiana, 2002.

19.   K. Madlener, H. Ciezki, J. Kampen, B. Heislbetz, and F. Albert, "Characterization of Various Properties of Gel Fuels with Regard to Propulsion Application," in *44th AIAA/ASME/SAE/ASEE Joint Propulsion Conference and Exhibit* Hartford, CT, 2008.

20.   Yoon, C., Heister, S., Xia, G., and Merkle, C., "Numerical modeling of Injection of Shear-Thinning Gel Propellants Through Plain-Orifice Atomizer", AIAA J. Propulsion & Power, V27, No.5, pp. 944-954, 2011.

21.   Yoon, C., Heister, S., Merkle, C. L., Xia, G., "Simulations of Plain-Orifice Injection of Gelled Propellants Under Manifold Crossflow Conditions", AIAA J. of Propulsion and Power, V29, No.1, 136-146, 2013.

22.   Yoon, C., Heister, S., Xia, G., and Merkle, C.,"Numerical Simulations of Gel Propellant Flow Through Orifices", AIAA 2009-5045, 45th AIAA Joint Propulsion Conference, Denver, CO, 2009.

23.   Yoon, C., Watson, C., Heister, S., Xia, G., Merkle, C., and Sojka, P., "Simulation of Injection of Shear-Thinning Gel Propellants Through Plain-Orifice Atomizer", AIAA 2010-7138, 46th AIAA Joint Propulsion Conference, Nashville, TN, 2010.

24.   Yoon, C., Heister, S., Xia, G., and Merkle C.L., "Simulation of Injection of Shear-Thinning Gel Propellants through Plain-Orifice Atomizer", AIAA-2010-7138, 46th AIAA Joint Propulsion Conference and Exhibit, Nashville, TN, 2010.

25.   Yoon, C., Xia, G., Merkle, C. L., Heister, S., "Numerical Modeling of Cross-Fed Orifice Flows for Shear-Thinning Fluids", European Conference for AeroSpace Sciences (EUCASS), Saint Peterburg, Russia, July 4-8, 2011.

26.   Yoon, C., Heister, S. D., and Campanella, O. H., "Modeling gelled fluid flow with thixotropy and rheological hysteresis", Fuel, V128, 467-475, http://dx.doi.org/10.1016/j.fuel.2014.02.051 ,2014.

27.   Yao W., Maris H. J., Pennington P. and Seidel G. M. 2005. Coalescence of viscous liquid drops. Phys. Rev. E 71, 016309.

28.   Jovani Luiz F_avero. Simula_c~ao de escoamentos viscoel~asticos : desenvolvimento de uma metodologia de an~alise utilizando o software openfoam e equacoes constitutivas diferenciais. Master's thesis, Federal University of Rio Grande do Sul, 2009. In Protuguese.

29.   S. C. Xue R. I. Tanner and N. Phan-Thien. Numerical modeling of transient viscoelastic flows. Journal of Non-Newtonain Fluid Mechanics, 2004.

30.   Meizhong Dai and David P. Schmidt. Adaptive tetrahedtral meshing in free-surface flow. Journal of Computational Physics, 208(1):228-252, 2005.

31.   H.G. Weller, G. Tabor, H. Jasak, and C. Fureby. A tensorial approach to computational continuum mechanics using object-oriented techniques. Computers in Physics, 12:620-631, 1998.

32.   J. Qian and C. K. Law. Regimes of coalescence and separation in droplet collision. Journal of Fluid Mechanics, 1997.

33.   Paulo J. Olivera and Fernando T. Pinho. Analytical solution for fully developed channel and pipe flow of Phan-Thien-Tanner fluids. Journal of Fluid Mechanics, 387:271-280,1999

34.   M.F. Tome G.S. de Paulo and S. McKee. A marker-and-cell approach to viscoelastic free surface flows using the PTT model. Journal of Non-Newtonian Fluid Mechanics, 147:149-174, 2007.

35.   Catoire, L., Chaumeix, N., and Paillard, C., "Chemical Kinetic Model for Monomethylhydrazine/Nitrogen Tetroxide Gas-Phase Combustion and Hypergolic Ignition," *J. Propulsion and Power*, Vol. 20, No. 1, 87-92, 2004.

36.   Seamans, T. F. and Dawson, B. E., "Hypergolic Ignition at Reduced Pressures," AFRPL-TR-67-129, 1967.

37.   Dambach, E. M., "Ignition of Hypergolic Propellants," Ph.D. Dissertation, Aeronautics and Astronautics Dept., Purdue Univ., West Lafayette, IN, 2010.

38.   Forness, J. M., "Phenomena Resulting from Hypergolic Contact," Masters Thesis, Aeronautics and Astronautics Dept., Purdue Univ., West Lafayette, IN, 2013.

39. Rein, M., "Phenomena of Liquid Drop Impact on Solid and Liquid Surfaces," *Fluid Dynamics Research*, Vol. 12, 61-93, 1993.

40. Rodriguez, F. and Mesler, R., "Some Drops don't Splash," *J. Colloid Interface Sci.*, Vol. 106, No. 2, 347-352, 1985.

41. O. Ubbink, Numerical prediction of two fluid systems with sharp interfaces, Ph.D. Thesis, Imperial College of Science, Technology, & Medicine, 1997.

42. S. Popinet, J. Comput. Phys. 190 (2003) 572-600.

43. J. Dennis, T. Kubal, O. Campanella, S. Son, T. Pourpoint, J. Propul. Power 29 (2013) 313-320.

44. C. Fineman, High shear capillary rheometry of gelled hypergolic propellants, Masters Thesis, Purdue University, 2012.

45. T. D. Kubal, R. Arnold, T. L. Pourpoint, O. H. Campanella, W. E. Anderson, 46th AIAA Joint Propulsion Conference & Exhibit, July 25-28, 2010, Nashville, TN, AIAA 2010-7140.

46. E. Dambach, B. Rankin, T. Pourpoint, S. Heister, Combust. Sci. Technol. 184 (2012) 205-223.

47. N. Nikolopoulos, G. Strotos, K. S. Nikas, G. Bergeles, Int. J. Heat Mass Trans. 55 (2012) 2137-2150.

48. C. Focke, D. Bothe, M. Kuschel, M. Sommerfeld, Experiments and Direct Numerical Simulations of binary collisions of miscible liquid droplets with different viscosities, ICLASS 2012, 12th Triennial International Conference on Liquid Atomization and Spray Systems, Heidelberg, Germany, September 2-6, 2012

49. C. Focke, D. Bothe, Phys. Fluids 24 (2012) 073105.

50. J. Forness, T. Pourpoint, S. Heister, 49th AIAA JPC, July 14-17, 2013, San Jose, CA, Paper AIAA 2013-3772

51. L. Catoire, N. Chaumeix, C. Paillard, *J. Propul. Power* 20 (2004) 87-92.

52. W. Anderson, M. McQuaid, M. Nusca, A. Koltar, "A Detailed, Finite-Rate, Chemical Kinetics Mechanism for Monomethylhydrazine-Red Fuming Nitric Acid Systems," Army Research Laboratory, ARL-TR-5088, February 2010.

53. E. Dambach, Y. Solomon, S. Heister, T. Pourpoint, *J. Propul. Power* 29 (2013) 331-338.

54. S. Wang, S. Thynell, *Combust. Flame* 159 (2012) 438-447.

55. W.-G. Liu, S. Wang, S. Dasgupta, S. Thynell, W. Goddard, S. Zybin, R. Yetter, *Combust. Flame* 160 (2013) 970-981.

56. J. Smith, "Time resolved measurements and reactive pathways of hypergolic bipropellant combustion," U.S. Army Research Office Document 41691.10-EG, March 2006.

57. T. Seamans, M. Vanpee, V. Agosta, *AIAA Journal* 5 (1967) 1616-1624.

58. J. Forness, T. Pourpoint, S. Heister, 49th AIAA JPC, July 14-17, 2013, San Jose, CA, Paper AIAA 2013-3772.

59.   F. M. Tao, *J. Chem. Phys.* 108 (1998) 193-202.

60.   R. E. Treybal, *Mass Transfer Operations, 3rd Ed.*, New York: McGraw-Hill, 1980.

61.   C. Duynslaegher, H. Jeanmart, J. Vandooren. *Proc. Combust. Inst.* **32** (2009) 1277-1284.

62.   J. Bian, J. Vandooren, P.J. Van Tiggelen. *Proc. Combust. Inst.* **21** (1986) 953-963.

63.   J. Vandooren, J. Bian, P.J. Van Tiggelen *Combust. Flame* **98** (1994) 402-410.

64.   R.C. Sausa, G. Singh, G.W. Lemire, W.R. Anderson. *Int. Symp. on Combust.* **26** (1996) 1043-1052.

65.   D.F. Davidson, K. Kohse-Höinghaus, A.Y. Chang, R.K. Hanson. Int. *J. Chem. Kinetics* **22** (1990) 513-535.

66.   H. Sun, L. Catoire, C.K. Law. *Int. J. Chem. Kinetics* **41** (2009) 176-186.

67.   *Gaussian 09, Revision A.1*, M. J. Frisch, G. W. Trucks, H. B. Schlegel, G. E. Scuseria, M. A. Robb, J. R. Cheeseman, G. Scalmani, V. Barone, B. Mennucci, G. A. Petersson, H. Nakatsuji, M. Caricato, X. Li, H. P. Hratchian, A. F. Izmaylov, J. Bloino, G. Zheng, J. L. Sonnenberg, M. Hada, M. Ehara, K. Toyota, R. Fukuda, J. Hasegawa, M. Ishida, T. Nakajima, Y. Honda, O. Kitao, H. Nakai, T. Vreven, J. A. Montgomery, Jr., J. E. Peralta, F. Ogliaro, M. Bearpark, J. J. Heyd, E. Brothers, K. N. Kudin, V. N. Staroverov, R. Kobayashi, J. Normand, K. Raghavachari, A. Rendell, J. C. Burant, S. S. Iyengar, J. Tomasi, M. Cossi, N. Rega, J. M. Millam, M. Klene, J. E. Knox, J. B. Cross, V. Bakken, C. Adamo, J. Jaramillo, R. Gomperts, R. E. Stratmann, O. Yazyev, A. J. Austin, R. Cammi, C. Pomelli, J. W. Ochterski, R. L. Martin, K. Morokuma, V. G. Zakrzewski, G. A. Voth, P. Salvador, J. J. Dannenberg, S. Dapprich, A. D. Daniels, Ö. Farkas, J. B. Foresman, J. V. Ortiz, J. Cioslowski, and D. J. Fox, Gaussian, Inc., Wallingford CT, 2009.

68.   V. Mokrushin, V. Bedanov, W. Tsang, M. Zachariah, V. Knyazev. *ChemRate: A Calculational Database for Unimolecular Reacation*. Ver. 1.5.8 (2009). Available from http://mokrushin.com/ChemRate/chemrate.html

69.   *CHEMKIN-PRO 15112*, Reaction Design: San Diego, 2011.

70.   Lawver, B. R., and Breen, B. P. "Hypergolic Stream Impingement Phenomena-Nitrogen Tetroxide/Hydrazine," NASA CR-72444, 1968.

71.   Ashland, "Klucel™ hydroxypropylcellulose," URL: http://www.ashland.com/products/aerowhip-hydroxypropylcellulose [cited August 2014].

72.   Evonik Industries, "Hydrophobic fumed silica," URL: http://www.aerosil.com/product/aerosil/en/Pages/default.aspx [cited August 2014].

73.   Kubal, T. D., Dambach, E. M., Son, S. F., Anderson, W. E. and Pourpoint, T. L., "Aspects of Monomethylhydrazine and Red Fuming Nitric Acid Ignition," 46th AIAA/ASME Joint Propulsion Conference, Nashville, TN, 2010.

74.   Arnold, R., Anderson, W. E., "Droplet Burning of JP-8/Silica Gels," 48th AIAA Aerospace Science Meeting, Orlando, FL 2010.

75.   Nicole J. Labbe, "Determining Detailed Reaction Kinetics for Nitrogen- and Oxygen-Containing Fuels." Ph.D. dissertation, University of Massachusetts Amherst (2013).

76. Muddu, R., Lu, J., Sojka, P. E., Corvalan, C. M. 2012. Threshold wavelength on filaments of complex fluids. Chemical Engineering Science, 69 (1), 602-606.

77. Muddu, R., Lu, J., Corvalan C.M. and Sojka, P.E., Effect of Perturbation Wavelength On Jets of Complex Fluids, AIChE Annual Meeting, November 7-12, 2010, Salt Lake City, UT.

78. Muddu, Rajeswari. 2010. Effect of perturbation wavelength on jets of complex fluids. Master's Thesis, Purdue University.

79. Dechelette, A., Muddu, R., Corvalan C.M., and Sojka, P.E. 2009. Breakup of Shear-Thinning Liquid Sprays Subject to Controlled Disturbances, International Congress on Liquid Atomization and Spray Systems ICLASS, Vail CO.

80. Lu, J., Corvalan, C. M. 2012. Coalescence of viscous drops with surfactant. Chemical Engineering Science, 78(20), 9-13.

81. Lu, J. and Corvalan, C.M., Surfactant Effects on the Dynamics of Drop Coalescence, AIChE Annual Meeting, October 16-21, 2011. Minneapolis, MN.

82. Lu, J., Corvalan, C. M. 2014. Influence of rheology on the impingement of laminar liquid jets. Chemical Engineering Science, submitted.

83. Lu, Jiakai. 2014. Influence of shear-thinning rheology on jet impingement and primary atomization events. Ph.D. Thesis, Purdue University.

84. Muddu, R., Lu, J., Vaidya, N., Sojka, P.E., and Corvalan, C.M. Replacement of interfacial proteins by waves of surfactant. Institute of Food Technologists Annual Meeting, July 17-20, 2010, Chicago, IL.

85. Corvalan, C. M., Free surfaces on fluid foods. SHPE 2012 National Conference, November 14-18, 2012. Fort Worth, TX.

86. Dechelette, A., Corvalan C.M., and Sojka, P.E. 2010. An experimental investigation on the breakup of surfactant-laden shear-thinning jets, International Congress on Liquid Atomization and Spray Systems, ILASS – Europe 2010, 23rd Annual Conference on Liquid Atomization and Spray Systems, Brno, Czech Republic.

87. Corvalan, C. M., Multiphase flow through porous food matrices. 4th International Conference on Porous Media and Annual Meeting of the International Society for Porous Media, May 14-16, 2012. West Lafayette, IN.

88. Dechelette, A., Corvalan, C.M. and Sojka, P.E. 2011. Effect of Surfactant Solubility and Adsorption Kinetics on Satellite Droplet Formation. International Conference on Liquid Atomization and Spray Systems, Estoril, Portugal.

89. Vaidya, N., and Corvalan, C. M. Interfacial Mass Transfer and Emulsion Stability. Conference of Food Engineering, April 2009, Columbus, OH.

90.   Vaidya, N., Lu, J., and Corvalan, C.M. Caking of amorphous food powders: a direct numerical simulation. Institute of Food Technologists Annual Meeting, July 17-20, 2010, Chicago, IL.